



UNIVERSIDAD DE CHILE
FACULTAD DE CIENCIAS FISICAS Y MATEMATICAS
DEPARTAMENTO DE INGENIERIA ELECTRICA

DESIGN AND CONSTRUCTION OF AN OPTICAL SYSTEM FOR A 31-45 GHZ
RADIOASTRONOMICAL RECEIVER

TESIS PARA OPTAR AL GRADO DE DOCTOR EN INGENIERÍA
ELÉCTRICA

PABLO IGNACIO ZORZI AVENDANO

PROFESOR GUÍA:
FAUSTO PATRICIO MENA

MIEMBROS DE LA COMISIÓN:
URS ULRICH GRAF
SCHIN'CHIRO ASAYAMA
LEONARDO BRONFMAN AGUILÓ

Este trabajo ha sido parcialmente financiado por:
CONICYT, a través de sus programas Fondo Basal, proyecto PBF06. Fondos ALMA para el
Desarrollo de la Astronomía, proyectos 31060002, 31080003 y 31080004. Becas Chile
FONDEQUIP, proyecto AIC-27.
MECESUP a través de proyecto FSM 0601.

SANTIAGO DE CHILE
MAYO 2013

Abstract

The Atacama Large Millimeter/Submillimeter Array (ALMA) is the largest astronomical observatory ever built. It is located on the Chajnantor plateau, at an altitude of 5000 meters above the sea level in northern Chile. It consists of an array of 66 antennas capable to detect weak-signal sources coming from the deepest space. The detection instrument on each antenna is divided in 10 high-sensitive dual-polarization heterodyne receivers that cover the frequency range between 30 to 950 GHz. In particular, the Band-1 receiver is been designed to cover the 31–45-GHz spectral window. This Band will give help the astronomers to bring new light in studies of anisotropies in the Cosmic Microwave Background Radiation, high-resolution of the Sunyaev-Zel'dovich effect, imaging of cluster gas at all redshifts, gravitational lenses survey and monitoring and mapping of the cold Inter Stellar Media matter at intermediate and high redshift.

The aim of this thesis is to design and construct a complete optical system for a 30-to-45-GHz radio-astronomical prototype receiver that fulfils the ALMA Band-1 specifications. The optical system includes a lens, a horn, and an orthomodal transducer. Each one of these microwave components were designed according to well-known existing theoretical models, and further optimized using commercial numerical software. Once the desired model was found, the device was constructed and characterized. Every one of the three devices presented excellent performances and good agreement between experimental measurements and simulations. Moreover, a very import part of this thesis involved the development and construction of a near-field setup used to measure the radiation pattern of the horn and the horn-lens arrangement system. The most important achievements of this thesis were two. (i) The development of a very compact spline-line horn design that has exigent beam characteristics. (ii) A first and unique dual-ridge orthomodal transducer design, since it supports a large bandwidth in a very compact form.

Keywords: Radio-astronomical instrumentation, heterodyne receiver, Quasioptics, microwaves, ALMA Band 1.

Resumen

El Atacama Large Millimeter/Submillimeter Array (ALMA) es el observatorio astronómico más grande jamás construido. Se encuentra en el llano de Chajnantor, a una altura de 5.000 metros sobre el nivel del mar en el norte de Chile. Consiste en un conjunto de 66 antenas capaces de detectar fuentes de señal muy débil que nos llegan desde el espacio más profundo. El instrumento de detección en cada antena consiste en 10 receptores heterodinos de doble polarización y de muy alta sensibilidad que cubren la gama de frecuencia entre 30 a 950 GHz. En particular, el receptor de la Banda-1 está diseñado para cubrir la ventana espectral 31–45 GHz. Esta banda dará ayuda a los astrónomos a traer nueva luz en estudios de Anisotropías en el fondo de radiación cósmica, alta resolución del efecto Sunyaev-Zel' dovich, detectar imágenes de gas de clúster a diferentes redshifts, estudios de lentes gravitacionales y monitoreo y mapeo del medio interestelar frío a intermedio y alto corrimiento al rojo.

El objetivo de esta tesis consiste en diseñar y construir un completo sistema óptico para un receptor prototipo de radio astronomía que trabaje entre los 30 a 45 GHz y que cumpla con las especificaciones de la Banda 1 de ALMA. El sistema óptico incluye una lente, una bocina y un transductor Orthomodal de polarizaciones. Cada uno de estos componentes de microondas fueron diseñadas utilizando modelos teóricos existentes y que son bien conocidos, y luego fueron optimizados utilizando un software comercial numérico muy avanzado. Una vez que se encontró el modelo deseado, el dispositivo fue construido y caracterizado. Cada uno de los tres dispositivos que fueron desarrollados y luego construidos en nuestro laboratorio, presenta excelentes prestaciones y de buen acuerdo entre las mediciones experimentales y simulaciones. Además, una parte importante de esta tesis estuvo muy involucrada en el desarrollo y la construcción de una cámara anecoica de campo cercana que fue utilizada para medir los patrones de radiación de la bocina y también del sistema integrado por la bocina y la lente. Los logros más importantes de esta tesis fueron dos. (i) el desarrollo de un diseño de bocina de tipo spline-line muy compacta y que genera patrones de radiación de muy alta calidad. (ii) un separador de polarización ortogonal de señales que es muy compacto y compatible con un gran ancho de banda.

This thesis is dedicated to my father Juan Carlos and my mother Raquel. Thank you both for all your unconditional support and understanding. Without your kindly help, this thesis could not be possible. You are the Best.

Acknowledgements

First, I would like to thank my adviser, Patricio Mena from the Department of Electrical Engineering, for his outstanding guidance, kindness and patience when working in this thesis project. I would also like to thank both, Dr. Leonardo Bronfman and Jorge May (R.I.P.) from the Astronomy Department, for their kindly support through all these years and for encouraging me to pursue and enjoy the Astronomical Instrumentation Ph. D. program at Universidad of Chile. Many thanks to Jose Pizarro for his outstanding support and help when constructing the horn and OMT at the mechanical workshop of Cerro Calán. It was a great and perfect job. I am very grateful also to Franco Colleoni for developing the automation control system and the image processing software for the near-field system setup, and also, for helping me with the radiation pattern measurements.

Special thanks go also to Michael Krause and Damian Moratschke from the machine workshop of University of Cologne for constructing the HDPE lens. I am also very grateful to Christopher Granet, at the BEA System in Australia, for helping us with the horn work. Many thanks goes also to Dough Henke and Dr. Stéphane Claude at the Herzberg Institute of Astrophysics (NRC-HIA) in Canada, for all the working hours that we spend together with the quasioptical design of the Band 1 optical system, and also for their kindly invitation and support during my 1-month stay at the HIA during September 2009. I would also like to express all my gratitude to Nicolas Reyes for all the hours that we spent together discussing and interchanging great ideas regarding the experimental measurement setups on how to perform such experiments. Finally special thanks to all the members of the Millimeter Wave-Laboratory at Calán and the Photonic Lab at Beauchef for their invaluable friendship and support through all these years that we spend together as working colleagues.

Table of Content

1	Introduction	1
1.1	Fundamentals	2
1.1.1	Science with the ALMA Band-1 Receiver	2
1.1.2	A Typical Millimeter Heterodyne Radio Receiver	5
1.1.3	Noise Basics	6
1.1.4	The ALMA Site Location	7
1.1.5	The ALMA Cassegrain Antenna Specifications	8
1.1.6	The Cryostat and the ALMA Cartridges	9
1.1.7	The ALMA Amplitude Calibration Device	10
1.1.8	The ALMA Band-1 Receiver Specifications	10
1.1.9	Low Noise Receiver Technology	11
1.1.10	Mixing Scheme	12
1.2	Addressed Problem	12
1.2.1	Our proposed 31–45-GHz Receiver System	13
1.2.2	Keeping the Total Receiver Noise as Low as Possible	14
1.3	Scope of this Thesis	16
2	Bibliographic Revision of Related Work	17
2.1	Existing Radio-telescope Receivers at 31–45 GHz	17
2.2	Preliminary ALMA Optical Design	18
2.3	Dielectric Lens and Quasioptical Ray Analysis	19
2.4	Infra Red Filters	20
2.5	Horn Design	22
2.6	Circular to Square Waveguide Transition	24
2.7	Ortho-Modal Transducer (OMT)	25
2.8	Manufacturing Techniques	27
2.8.1	Choice of Material	27
2.8.2	CNC Machine	28
3	Quasioptic Lens Design and Construction	29
3.1	Introduction	29
3.2	Quasioptical Theory	30
3.2.1	Focusing of Gaussian Beams (Thin Lens)	35
3.2.2	Gaussian Beam Telescope	37
3.2.3	Thick Lens Corrections	38
3.2.4	Gaussian Beam Launchers	39
3.2.5	Complex Beam parameter and Ray Matrices	40
3.2.6	Dielectric Materials Properties	45
3.2.7	Quasioptical treatment of Cassegrain Antennas	46
3.2.8	Off-axis Feed Aberrations in Cassegrain Antennas	49
3.3	Optical System Design Examples and Their Noise Estimation	51
3.3.1	Optical Dimensions between Receiver and Subreflector	52
3.3.2	Feed Horn with or without optical arrangement	52
3.3.3	Four Different Optical System Design Examples	54
3.3.4	Discussion of Simulation Results	61
3.4	Final Lens Design and Construction	63

3.5	Lens Antireflection Layer	65
3.6	Conclusions.....	69
4	Horn Design and Construction	70
4.1	Introduction.....	70
4.2	Classical Corrugated Conical Horn	71
4.2.1	Theory and Design of a Preliminary Horn	71
4.2.2	Preliminary Corrugated Horn Simulation.....	76
4.2.3	Optimizing the Preliminary Corrugated Horn Design.....	77
4.3	Corrugated Spline-line Horn Design Using Mode Matching Techniques.....	79
4.4	Comparison of Horn Designs.....	82
4.5	Horn Construction and Experimental Measurements	83
4.5.1	Construction of the Corrugated Spline-line Horn.....	83
4.5.2	Beam-pattern Measuring Setup	83
4.5.3	Horn Measurements.....	84
4.5.4	Horn and Lens Measurements	89
4.6	Quasioptical Beam Analysis Corrections	93
4.7	Conclusions.....	95
5	OMT Design and Construction.....	96
5.1	Introduction.....	96
5.2	Waveguide Basics.....	97
5.3	Orthomodal Transducer Design.....	101
5.3.1	Dual-ridge Section Design.....	102
5.3.2	E-bend Section Design	103
5.3.3	Y-combiner section Design	103
5.3.4	The Final Optimized OMT Design.....	104
5.4	Circular to Square Transition.....	106
5.5	Construction of the Devices.....	108
5.6	Experimental Results	109
5.6.1	Description of the OMT Measuring Setup	109
5.6.2	OMT Measurements.....	109
5.7	Horn-Transition-OMT Simulations with HFSS.....	112
5.8	Conclusions.....	114
6	Discussion and Further Work.....	115
7	References	117
8	Appendix A: Technical Drawing.....	126
8.1	Lens.....	126
8.2	Horn	127
8.3	OMT.....	128
9	Appendix B: Author List of Publications.....	129
	Articles.....	129
	Conferences	129

Chapter 1

Introduction

The Atacama Large Millimetre Array (ALMA) will be the largest millimetre and sub-millimetre radio telescope in the world. It is under construction in the Altiplano region of northern Chile, specifically in the Chajnantor Plateau. This is an extremely dry site at 5000 m of altitude. Consequently, it is one of the best sites on earth for the measurement of millimetre/sub-millimetre radiation from astronomical sources. ALMA combines an array of 66 antennas (54×12m and 12×7m diameter antennas) specially designed for doing interferometry and spectroscopic measurements of the early Universe with an angular resolution less than 1". It will also reveal new information about the birth of stars and planets and the formation of galaxies. Since the received signals coming from distant radio sources are extremely weak, ALMA will use the most advanced low-noise receiver technologies developed so far. These technologies will directly help to increase the signal-to-noise ratio quality of the measurements and, therefore, decrease the time integration when doing interferometry. In general, ALMA will provide high sensitive and precision imaging between 30 and 950 GHz in 10 bands at the Southern Hemisphere. This telescope will be fully functional in about 2015.

In 2008 the Departments of Electrical Engineering (DIE) and Astronomy (DAS) of Universidad of Chile, created of a new interdisciplinary research area in the field of Radio Astronomical Instrumentation. One of the first projects of this new group was the design, construction and testing of a 31-to-45-GHz full-operating ALMA Band-1 prototype receiver. For that purpose two Ph. D. students were selected to initiate this work. One of these students would be in charge of the construction of the complete optical system part of this receiver while the second would work with the amplification, mixing and down-conversion part of the signals. The aim of this Ph.D.-thesis is related to the first part of the aforementioned project, namely with the different aspects that involve the design, optimization and construction of a suitable optical system for a 31-to-45-GHz receiver that will be part of the prototype receiver for Band 1 of ALMA.

A receiver covering ALMA Band 1 offers many unique scientific research capabilities related to the field of radio astronomical observation for low centimetre wavelength ranges. There are several important radio astronomical studies that can be made at this frequency band. Among them, the most interesting ones are the Cosmic Microwave Background Radiation (CMBR) anisotropies studies, high-resolution Sunyaev-Zel'dovich (SZ) effect imaging of cluster gas at all redshifts, gravitational lenses survey and monitoring, and mapping the cold Inter Stellar Media (ISM) matter at intermediate and high redshift.

1.1 Fundamentals

1.1.1 Science with the ALMA Band-1 Receiver

In astronomy there are several quantities, such as magnitudes, spectra, angular sizes and distances that can be measured with radio-telescopes to study the evolution and structure of different stellar objects, galaxies, Interstellar Medium (ISM) and the “*cosmic microwave background radiation*” (CMBR). The CMBR is the cooled remnant of the hot Big Bang explosion that fills the entire universe with a microwave radiation that has an average temperature of about 2.725 Kelvin at 160.2 GHz [1]. In simple terms it means that the space between the stars and galaxies is not empty when observing the sky with a radio telescope. At very small angular size scales (i.e. large dipole moment l) the Band-1 receivers will be able to detect these small CMBR temperature fluctuations of a few micro Kelvins. These small temperature fluctuations are called “anisotropies” and are used to probe the galaxies scale sizes at very far astronomical distances.

The study of the cosmic microwave background radiation and the astronomical red shift observations are together regarded as the best available evidence for the Big Bang theory and therefore are very important tools for modern cosmology. Figure 1 shows the CMB anisotropy (red line) and other detectable source of emissions from our Galaxy (e.g. synchrotron radiation, free-free radiation, and thermal radiation) as a function of the antenna temperature.

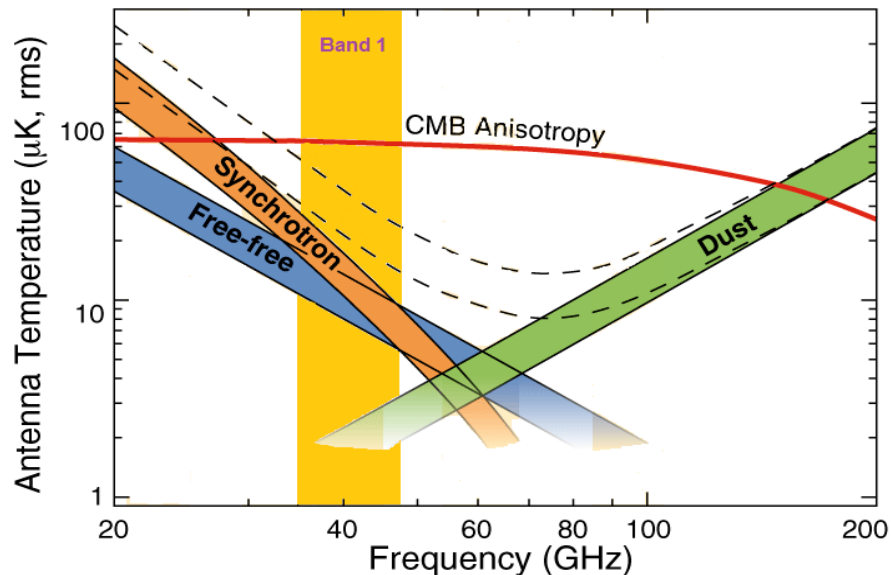


Figure 1. Expected CMB anisotropy (red line) as a function of the antenna temperature. The three main interstellar dust foreground emission from our Galaxy are also shown, synchrotron radiation, free-free radiation, and thermal radiation. The ALMA Band-1 coverage is indicated in with a yellow bar on the plot. The dotted lines show the total foreground emission contribution. Here one can note how the Band 1, thanks to its sensitive and high resolution, will be able to detect in detail the CMBR anisotropy fluctuations [1].

One of the most interesting application of the ALMA Band-1 will be the high resolution imaging of the “*Sunyaev-Zel'dovich effect*” (SZE), a second order anisotropy spectral distortion of the CMBR. The SZE effect is a physical process that occurs when high energy electrons transfer energy to the low energy CMBR photons (through inverse Compton scattering) in a hot gas environment, resulting in irregular small fluctuations of the CMBR [2]. Using these surveys, astronomers will be able to detect density perturbations in the Universe at high redshifts ($z > 1$) which will reveal several hundred of new dense galaxy clusters located at the South Hemisphere part of the sky.

With Band 1 it will be also possible observe *gravitational lenses*, which are formed when photons are deflected by strong gravitational potentials around a massive object between the source object and the observer [3]. This effect was already predicted by Albert Einstein's general theory of relativity in the beginning of the 19 century, but it was not until 1979 that was confirmed by observations of a double quasar known as Q0957+561 [4]. When studying these objects at low frequencies, scientist will be able to measure more accurate values on the Hubble cosmological constant and on the total matter density of the universe.

Another important application of this receiver will be when mapping the cold “*Inter-Stellar Media*” (ISM) matter at intermediate and high redshifts. The ISM mapping is related to trace the density of very cold gas (where star formation activity may occur) using indirect detection techniques of low rotational photon emission transition of CO J=1-0, CO J=2-1, CO J=3-2, [5], HCN J=1-0 and HCN J=2-1 [6], which are redshifted in the range of $z = 1-10$ approximately. CO and HCN are use for tracing H_2 in cold molecular clouds (i.e. dark nebula) where star formations occurs. Figure 2 show us the different CO detectable transitions at different redshifts.

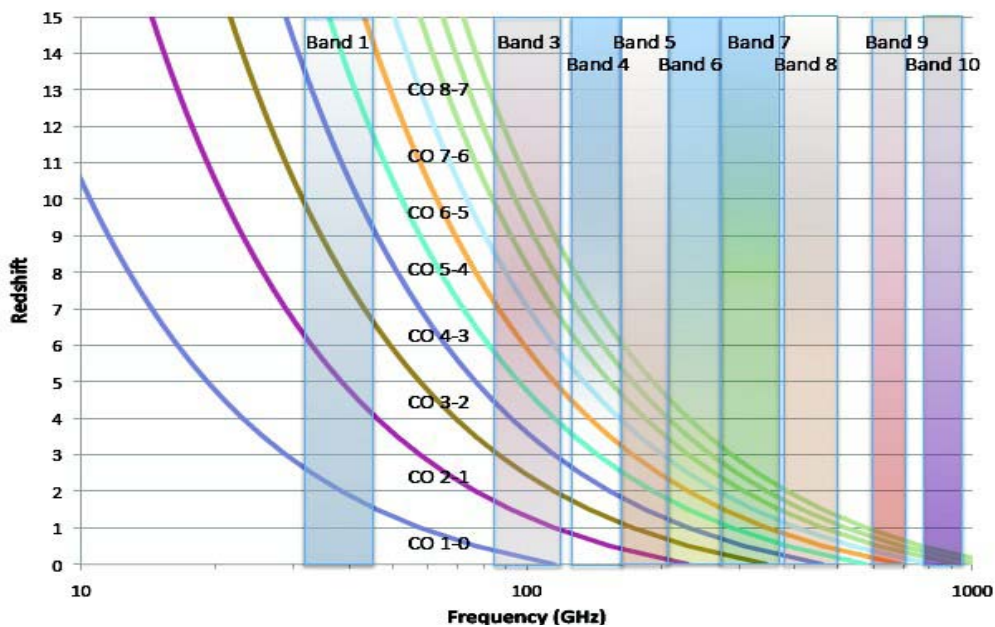


Figure 2. The CO emission transitions at frequencies between 10-1000 GHz as a function of redshift. The detection frequency range of the different ALMA bands is also shown. Of especially interest, is the left side of the figure, where the ALMA Band-1 detectable CO transitions at different redshift are illustrated.

“*Masers*” (“microwave amplification by the stimulated emission”) are similar to lasers but they emit radiation at shorter wavelengths in the range of radio frequencies or microwaves instead of visible light. In general there are two different kinds of radioastronomical maser sources: circumstellar masers and interstellar masers. The former is generated from the mass outflow from red giants stars while the latter is found in clouds of molecules in regions where stars are forming. To the circumstellar class of masers belong, for example, the OH, H₂O and the SiO masers. The CH₃OH (Methanol) maser is a type of interstellar maser. Between 31 to 45 GHz, ALMA will detect the SiO and CH₃OH masers. Their detectable transitions at those frequencies are summarized in Table 1 and 2.

Table 1. Observed SiO maser lines in the Band 1 of ALMA (Wooten 2007). The v and J correspond to vibration and rotational quantum level numbers, respectively.

Emission transitions	Frequency (GHz)
$v=0 (J= 1 \rightarrow 0)$	43.423585
$v=1 (J= 1 \rightarrow 0)$	43.122079
$v=2 (J= 1 \rightarrow 0)$	42.820582
$v=3 (J= 1 \rightarrow 0)$	42.519373
$v=0 (J= 1 \rightarrow 0)$	42.879916
$v=0 (J= 1 \rightarrow 0)$	42.373359

Table 2. Observed (Menten 2007) and predicted (designated with a star, Cragg et al. 2005) methanol maser lines in Band 1.

Transitions	Frequency (GHz)
$14(-3) \rightarrow 15(-2)E^*$	34.2368
$4(-1) \rightarrow 3(0)E$	36.1693
$7(-2) \rightarrow 8(-1)E$	37.7037
$6(2) \rightarrow 5(3)A^+$	38.2933
$6(2) \rightarrow 5(3)A^-$	38.4527
$7(0) \rightarrow 6(1)A^+$	44.0694
$2(0) \rightarrow 3(1)E^*$	44.9558

The birth of a planet could take several of millions of years. Its formation takes place inside “*protoplanetary disks*” rich in dust and gas that are surrounding young stars. In a first evolutionary stage, the dust starts to interact with the interstellar gas that freeze and covers its surface to form “*grains*”. Lately, the grains tend to chunk with each other due to gravitational forces, and thereafter becomes larger pebbles, that later becomes rocks and finally a planet. To study the evolution of such grains deep inside protoplanetary disks, astronomers need to observe at longer wavelengths since then these disks become optically thin. ALMA Band 1 is intended to study the grains evolution inside protoplanetary disk at wavelengths that varies between 0.7 to 1.0 cm.

1.1.2 A Typical Millimeter Heterodyne Radio Receiver

The typical front-end configuration of a *heterodyne* radio receiver working up to 100 GHz is presented in Figure 3. This kind of receiver is called *coherent detector* receiver since it maintains the phase information of the original signal while it is down converted into a lower frequency signal making easier its digital post-processing. In brief, what a heterodyne receiver does is to combine two signals with different frequencies, one coming from the antenna, of frequency ω_1 , and the other of proportional strength but lower/higher in frequency, ω_2 , provided by the local Oscillator (LO), which then results in an output signal that contains a complete spectrum of frequencies that are linear combinations of ω_1 and ω_2 , but with the amplitude proportional to the amplitude of ω_1 . The element where this conversion process takes place is called mixer which, in general, is any nonlinear microwave device, such as a Schotky diode [7].

The useful output terms in a mixing process are the frequencies $(\omega_1 - \omega_2) > 0$ (Upper Side Band “USB”) and its image $(\omega_2 - \omega_1) > 0$ (Lower Side Band “LSB”). Depending on how these two output signal bands are processed, a receiver is classified in three main categories: SSB, DSB, and SBS receivers. In a Double Side Band (DSB) receiver both sidebands are detected in the same output while in a Single Side Band (SSB) receiver the unwanted sideband signal is suppressed using a pass filter in front of the mixer [8]. Finally there is the so-called sideband separating (SBS) receiver where the unwanted image channel is not filtered out but is separated from the signal channel and its outputs will be processed independently [9].

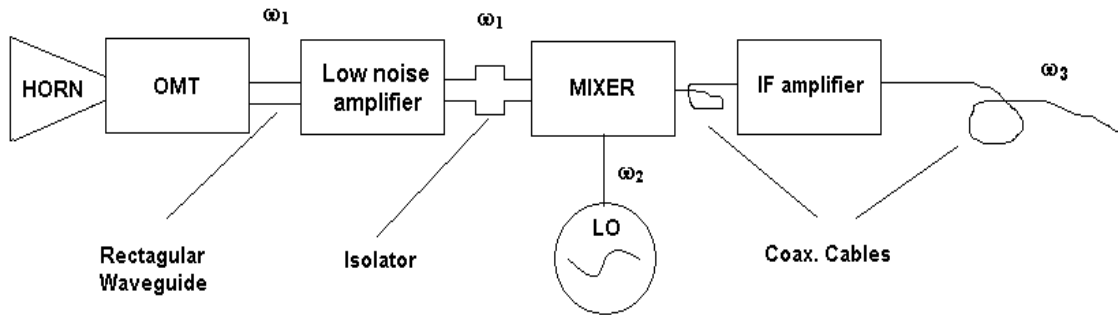


Figure 3. Block diagram of a typical heterodyne radio receiver configuration for frequencies up to 100 GHz. The figure shows also the input signal ω_1 , the local oscillator signal ω_2 , and the resulting down converted output signal ω_3 .

The receiver configuration block shown in Figure 3 depicts a horn that guides the EM-radiation (previously collected by the antenna dish) into the Ortho-Modal Transducer, OMT, which splits the signal polarization in two linear/circular orthogonal polarized components. The OMT is a device that can be integrated in a heterodyne receiver system if polarization measurements are needed to be done. Then, the output of a single polarized signal is guided into a low noise amplifier which amplifies the signal adding noise as low as possible. This device is the main responsible to determine the overall noise performance of the whole receiver system. The microwave isolator lying between the low noise amplifier and the mixer allows that the transmitted signal follows the direction of propagation without being reflected into the input port of the amplifier, avoiding in this way saturation or instability of the amplifier. Finally, the

resulting amplified signal is down converted inside the mixer block before being amplified later on by the Intermediate Frequency (IF) amplifier, the last component of the heterodyne receiver. It is important to mention that in general the entire receiver will show better performance when working at cryo-cooled temperatures of 77K or/and 4K (see section 1.1.5).

1.1.3 Noise Basics

Noise is formed by unwanted power contributions that, when combined with the power of the wanted received signal, affects the ability of the receiver to reproduce correctly the original signal. In general if the attenuation of a medium (e.g. atmosphere or electrical component) increases, so it does its emitted noise temperature. For frequencies above 1 GHz the source of noise can be separated in three main groups [10]:

- a) The noise emitted by natural sources located within the antenna reception area such as the sky (Cosmic Background Microwave radiation) and the earth noise (non-ionized part of the atmosphere).
- b) The thermal noise generated by the different components in the receiving system.
- c) The noise contribution produced by the ground transmitting antennas and electronics which produce interference.

The equivalent total noise power captured by a receiver in dBW is given by $kT_{sys}B$ where k is the Boltzmann's constant, T_{sys} is the total temperature contribution of the different noise sources (K) and B is the noise bandwidth (Hz). Now, the total noise contribution is given by the following equation:

$$T_{sys} = T_{ant} + T_{rec} = T_{atm} + T_{sky} + T_{ground} + T_{rec} \quad [\text{K}] \quad (1)$$

where:

T_{ant} = the total antenna noise temperature = $T_{atm} + T_{sky} + T_{ground}$ [K]

T_{atm} = the non-ionized atmospheric noise temperature [K]

T_{sky} = the cosmic background noise temperature = 2.7 K

T_{ground} = the earth surface ground noise temperature [K]

T_{rec} = the total noise temperature of the receiver [K]

The receiver noise T_{rec} is generally represented as if there were multiple noisy components connected in cascade, where the noise temperature of the cascade will be limited by the noise temperature of the first component (from left to right) in the cascade. The gains of the components at the beginning of this system will have a large contribution effect to minimize the total noise temperature at the output of the system. Its total noise contribution can be estimated according to [11]:

$$T_{rec} = T_1 + \frac{T_2}{G_1} + \frac{T_3}{G_1 G_2} + \dots + \frac{T_n}{G_1 G_2 \dots G_{n-1}} \quad [\text{K}] \quad (2)$$

where:

T_n = noise temperature of the n^{th} component in the cascade [K]

G_n = gain of the n^{th} component in the cascade. ($n = 1, 2, 3, \dots$)

1.1.4 The ALMA Site Location

The amount of Precipitable Water Vapour (PWV) on Llano de Chajnantor site, where ALMA is being constructed, can vary between 1.0 to 0.3 mm along the year which allows a full spectral coverage transparency for all the 10 receiver bands designed for this array. A typical PWV median of 0.5 mm can be expected for 50% of the observing time during the months of May-November. In Figure 4, it is shown the atmospheric transmission between 1 GHz to 1 THz for PWV value of 0.5mm. Note the excellent transmission values at lower frequencies, especially around the Band-1 frequency range.

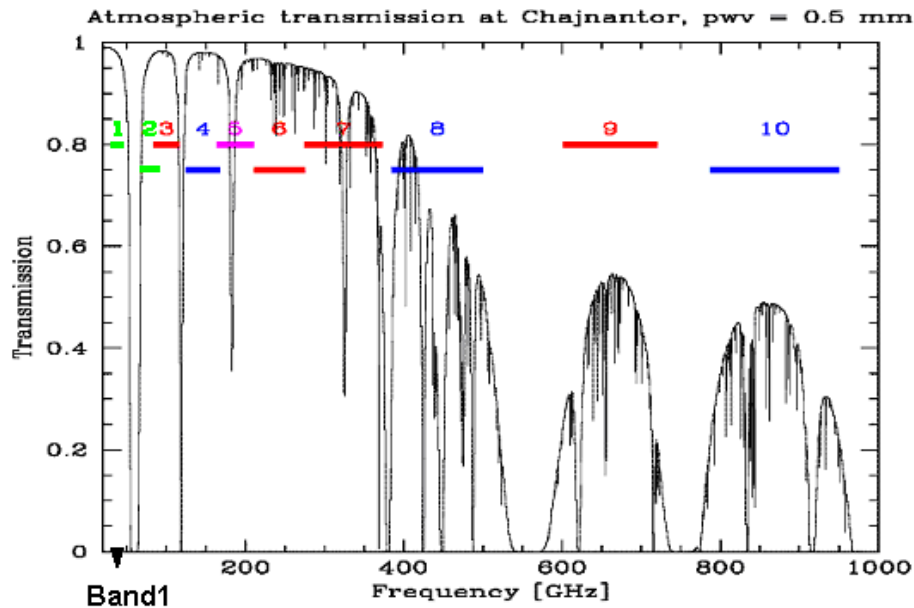


Figure 4. Zenith atmospheric transmission estimation in Chajnantor as a function of the frequency with an average perceptible water vapour $PWV = 0.5$ mm [12]. Note that the frequency bands corresponding to the 10 different ALMA receiver systems are also plotted in the diagram.

An annual variation of the PWV content study at Chajnantor, based on 10 years of site testing [12], shows that this site has the most dryness and stable sky environment around the world, very important characteristics that finally determined ALMA to be constructed there. Members of our group were involved in the site identification already in 1994.

1.1.5 The ALMA Cassegrain Antenna Specifications

The final ALMA array configuration will consist in a total of fifty 12-meter diameter antennas that will be used for interferometry, four 12-meter diameter antennas for total power measurements and twelve 7-meters diameter antennas for doing short spacing interferometry [13]. The first 50 antennas are being manufactured by Alcatel Alenia Space (for ESO, Europe) and Vertex RSI (for NRAO, USA), while the remaining ones are being constructed by Mitsubishi Electrical Company (for NAOJ, Japan). Each antenna has a parabolic primary reflector with a diameter of 12 or 7 m and a hyperbolic secondary reflector. In Figure 5, the optics layout of a 12-meter Cassegrain antenna is shown and the symbols are described in Table 1. For further details about the mechanical layout of the Cassegrain antennas, concepts and definitions please see reference [14]. See also reference [15] for a dual reflector Cassegrain antenna design introduction.

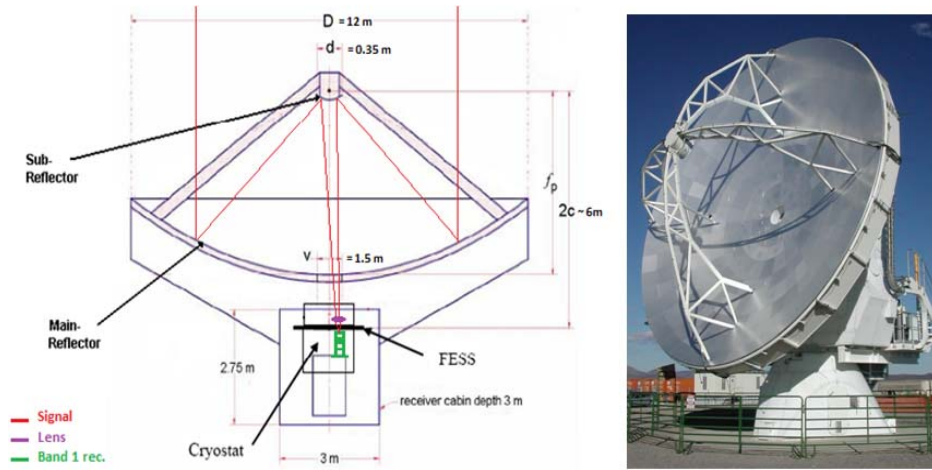


Figure 5. (Left) Optical layout of the ALMA 12-meter diameter Cassegrain antenna. The diagram also shows the ALMA Cryostat, where the Alma Band-1 receiver band, will be located. The FESS is the Front End Support Structure which helps to attach the Cryostat to top of the antenna cabin, and also align its centre with respect to the antenna optical axis. Refer to Table 1 for symbol descriptions [13]. (Right) An ALMA Cassegrain antenna manufactured by VERTEX.

Table 3. 12-meters Cassegrain antenna optical Parameter description [13].

Symbol	Description	Value
D	Primary Aperture	12 m
f_p	Focal length of Primary	4.8 m
f_p/D	f/D ration of Primary	0.40
d	Secondary Aperture	0.75 m
F/D	Final f/D ratio	8.00
F	Focal length of equivalent Paraboloid	96 m
M	Magnification	20
e	Secondary Eccentricity	1.10526
θ_p	Primary angle of illumination	128.02°
θ_s	Secondary angle of Illumination	7.16°
$2c$	Distance between primary and Secondary foci	6.177 m
v	Primary Vertex Hole Clear Aperture	0.75 m

1.1.6 The Cryostat and the ALMA Cartridges

The ALMA cryostat [16] was specially designed to house all ten receivers inside a common dewar. The dimensions of the dewar are 0.97 m in diameter and a 0.62 m in height. Each receiver is built in a cylindrical structure called *cartridge* which is divided in three section-levels cooled down to 4, 15 and 110 K, respectively, by a 3-stage GM RDK 3ST Sumitomo cryocooler [17]. The cartridges are designed to be inserted into ports at the bottom of cryostat. In Figure 6, the ALMA cryostat concept is illustrated. The dimensions of the Band-1 cartridge are 0.17 m in diameter, approximately 0.47 m high and it is located on a radius of 0.295 m from the centre of the cryostat top plate [18]. Due to fact that the Band-1 receiver components such as the horn, OMT and other active components are relatively large, the 4 K stage-plate can be removed from the cartridge, leaving only the 15 and 110 K stages to cryocool the components. The cartridge height measured from its bottom to the 15 K shield plate will be then 0.2 m which means that there will be $2\pi \times 0.17 \times 0.27 \text{ m}^3$ of free space available to accommodate the optics and the low noise amplifier on top of this plate.

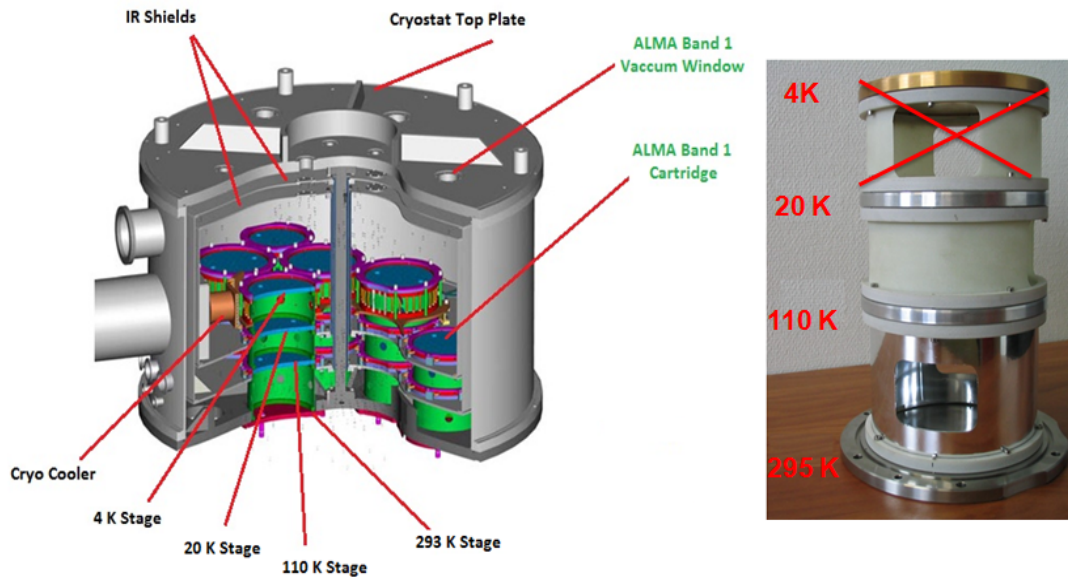


Figure 6. (Left) Cross-section of an ALMA cryostat with a view of the cartridges location inside of it. The signal collected by the antenna subreflector is focused through the vacuum windows inside the corresponding receiver horn. Note that the receiver cartridges will be inserted into ports at the bottom of the cryostat and the sides of the chassis will hold part of the supporting electronic equipment. (Right) An ALMA cartridge showing the different cryocooled stages. The 4 K stage will be removed to attach the most critical microwave parts on top of the 20 K plate [16].

1.1.7 The ALMA Amplitude Calibration Device

The Amplitude Calibration Device or “ACD”, is a robotic arm that consist of two blackbody radiators loads with well known physical temperatures that are monitored as a power references [23]. The first load is an ambient temperature of about 293K. The second one is an actively hot load kept at a well-established temperature of between 343 and 353 K. There is also a third solar load that is will be used for Sun observations. By inserting the hot or the ambient loads in front of one selected receiver band input, and then shifting between them, the amplitude scale of each receiver measure system noise can be calibrated with respect to the detected measured sky signal. The importance of mentioning this device in this section is due to the fact that the distance between the Cryostat Top-plate and the bottom part of the ACD filters will limited the spacing of the optical setup arrangement design to be used on top of the Band1 receiver. In Figure 7 it is shown a schematic CAD figure of such system.

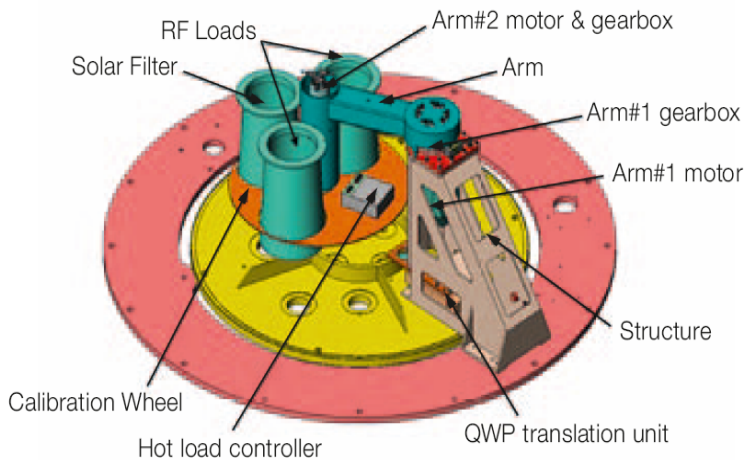


Figure 7. CAD overview drawing of the ALMA ACD showing its mayor sub-device features [23].

1.1.8 The ALMA Band-1 Receiver Specifications

All ten receiver bands are designed to measure total power and polarization state (dual linear polarization) of the received signal at a given frequency. The frequency band directly determines the component technology (optics design, mixing scheme, and amplifier types) that will be used in the receiver design. According to the ALMA Project Book [19][20], the ALMA Band-1 receiver requirements are summarized in Tables 4 to 6.

Table 4. Band-1 general receiver configuration and noise specifications.

Frequency Range RF input	Optical system design	Low Noise Receiver technology	Mixing scheme	Frequency Range IF output	Maximum Receiver noise temperature	
					T (SSB) over 80% of the RF band	T (SSB) at any RF frequency
31 – 45 GHz	Lens + IR filters + Horn + OMT	HEMT	USB	4 – 12 GHz	17 K	28 K

Table 5. Band-1 Local-oscillator (LO) specifications.

Bottom frequency	Top frequency	Remarks
27 GHz	33 GHz	USB mixing scheme

Table 6. Band-1 SSB Mixer requirements.

Down converted Output frequency	Bandwidth Single-Side Band (SSB) fully tuneable	Image band Rejection* (SSB)
4 - 12 GHz	8.0 GHz	> 10 dB

1.1.9 Low Noise Receiver Technology

HEMT stands for “High Electron Mobility Transistor” and is a field effect transistor that presents very low noise output characteristics when working at room temperature. Some of the designs present good performances also at cryogenic temperatures [22]. HEMT amplifiers are often used in radio astronomical receiver systems as the primer amplification device when the detection signals are below 100 GHz. The HEMT is a junction between two materials with different energy bandgaps. For example, one is made of a highly-doped n-type AlGaAs thin layer and a non-doped GaAs layer. The effect of this junction is to create a very thin layer (also called 2-DEG “two-dimensional electron gas”) where the Fermi energy is above the conduction band. When biasing this 2-DEG layer, the substrate behaves like a uniform material with high electron mobility (i.e. low resistivity) and adding the fact that with today’s manufacturing technology techniques, the gate length of the junction can be reduced in a few tenths of micrometers, then, the recombination time of the transistor will be very short. Therefore the HEMT has ability to work at higher frequencies than it is possible with other transistor of the same family such as the MESFET [23].

1.1.10 Mixing Scheme

In Figure 8, the Upper Side Band, *USB* mixing scheme is presented. The term ω_1 correspond to the input signal being detected (31–45-GHz), ω_2 is the signal delivered by the Local oscillator that it will be tune, in this particular case, between 27 and 33 GHz (depending on the frequencies that are need to be detected), while $\omega_1 - \omega_2$ is the resulting USB output signal. The Lower Side Band signal *LSB* is suppressed by a waveguide high-pass filter placed at the input of the mixer. Thus, this mixing scheme will delivery and instantaneous analogue Intermediate Frequency (IF) output signal of 8 GHz for each polarization, starting from 4 GHz up to 12GHz.

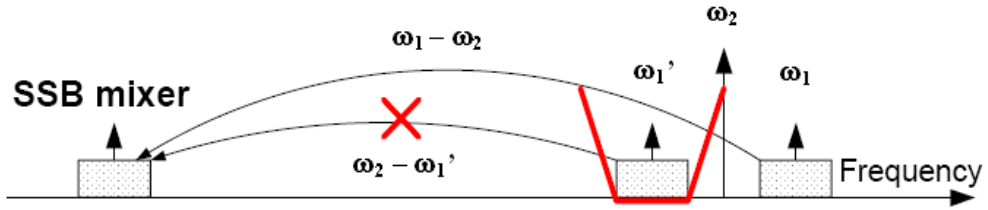


Figure 8. The diagram shows how the RF input signal ω_1 and its image ω_1' are down-converted in a Single Side Band mixer. In this figure it is shown as example the cancellation of the LSB image. ω_2 corresponds to the LO frequency.

1.2 Addressed Problem

When measuring very weak astronomical signals, it is important to keep the antenna and the receiver noise temperatures, T_{ant} and T_{rec} , as low as possible. If the noise temperature of the antenna is maintained as low as possible, which can be achieved by using a large antenna dish (maximizing its directivity) and a well designed corrugated horn (minimizing the side lobes), then, according to Equation (1), T_{rec} can be minimized by cooling as much as possible all or the major parts of the receiver components, such as the optical elements and the HEMT amplifier of the receiver system. There is, however, also another important concept in radio astronomy that is must be taken into account when designing radio astronomical receivers which is called the *sensitivity* of a receiver. This is a figure of merit that tells us the ability of such instrument to pick up and resolve weak signals among a noisy environment. The sensitivity ΔT of a single radio antenna system is given by [24]:

$$\Delta T \approx T_{sys} \sqrt{\frac{1}{\Delta \nu \Delta t} + \left(\frac{\Delta G}{G}\right)^2} \quad [\text{K}] \quad (3)$$

Where:

T_{sys} = total noise contribution of the whole receiver system (see Eq.1) [K]

$\Delta\nu$ = bandwidth of the system [Hz]

Δt = integration time of the measurement [sec]

G = total gain of the receiver system

ΔG = total gain fluctuations of the receiver system

Equation (3) is telling us that the receiver sensitivity depends on the gain stability of the system and its total noise temperature. It also tells us that the use of wide bandwidth and long integration time will also reduce noise fluctuations (i.e. increase its sensitivity). Therefore, the goals of radio astronomical receiver development can be identified as a three step optimization process. First, greater sensitivity of the system needs a large total gain which can be solved by using large antenna reflectors (the size of the antenna is already fixed, nothing more that can be done there), special designed horns with high directivity and low side lobes characteristics (a part of the optical receiver design), high gain with low noise “first stage” amplifier (e.g. HEMT amplifier [25]) and the use of low loss optical microwave components (see section 2.7.1 for further discussion). Secondly, the total noise of the system must be kept as low as possible which leads to the use of cryogenics on most of the optical components, and passive and active microwave components as well. Finally, a stable gain stability of the system is reached, by constructing the radio astronomical antenna in a site with excellent weather conditions (as it was discussed in section 1.1.3), and by using very stable gain low noise amplifier (LNA). Once these three processes are optimized, the determination of the integration time duration can be determined according to the type of observations that are needed to be made.

1.2.1 Our proposed 31–45-GHz Receiver System

Following the specifications for the Band-1 receiver presented in section 1.1.6, the configuration shown in Figure 9 has been proposed by our research group. The receiver system has been divided in three mayor subsystem blocks: the optical system, the amplification system, and the down-conversion system block. These subsystems are planned to be constructed using our own designed/manufactured microwave components (such as the lens, horn, OMT, HEMT's waveguide filter, while other components will be purchased (isolators, IF low noise amplifier, mixers) or acquired trough external cooperation with foreign Universities (e.g. transistor for the HEMT amplifiers and PPL controller of the LO system).

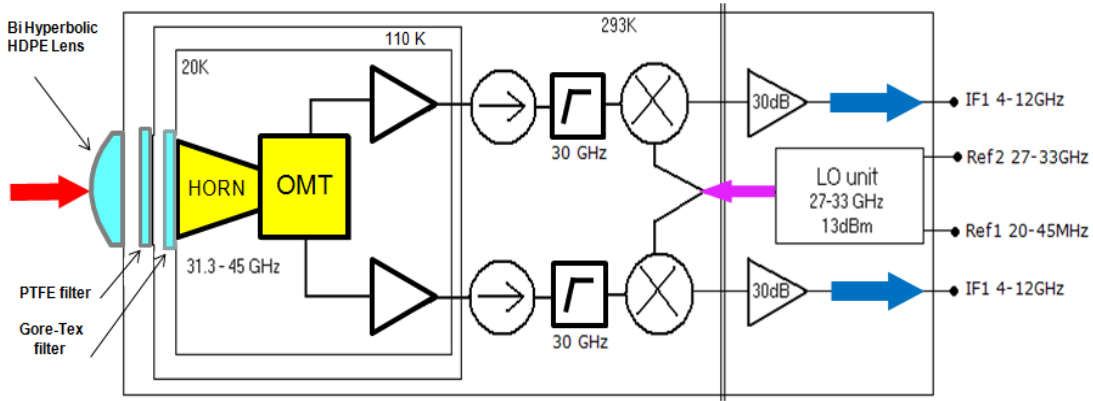


Figure 9. Our proposed Band-1 receiver configuration. In this diagram, the receiver is divided in 3 main subsystems where the optical and amplification systems are mounted in the cartridge and placed inside the cryostat. The down-conversion chain system will be located outside the cryostat, specifically behind it where this system is attached to the electronics chassis part of the system.

An observed RF signal that is coming from a Cassegrain subreflector antenna is coupled with the horn via an optical system made by a lens and a coupled of IR-filter. The signal is then divided by an Orthomodal Transducer (OMT) into two orthogonal polarization independent channels that are further amplified by an High-Electron Mobility Transistor amplifier (HEMT) each, cooled at 20K. Later, these amplified signals are down-converted into an Intermediate Frequency (IF) output signal with the help of a Schottky mixer, but prior reaching that state, the Lower Side Band (LSB) part of the amplified signal was suppressed by a low pass-filter.

The design, development, construction and testing of the whole first subsystem part of this receiver prototype will be the Ph. D. thesis topic of the author of this paper. The second and third subsystems will be developed and constructed by a second Ph. D. student. These two students are members of the Radio Astronomical Instrumentation Group of the Electrical Engineering Department of the Universidad de Chile, located in Santiago de Chile.

1.2.2 Keeping the Total Receiver Noise as Low as Possible

According to the receiver configuration proposed in the previous section, there are two main ways to tackle the low noise specification levels needed by the ALMA Band 1 receiver system. The first is by optimizing each one of the optical component materials, dimensions and design to keep the overall total noise contribution of the optical system as low as possible. The second one is fully determined by the total gain, and noise contribution of the HEMT amplifier that is going to be used in the receiver. Using Equation (2) and applying the strategy of dividing the proposed receiver configuration (Figure 9) in three main blocks, each one with a noise temperature, T_i , gain, G_i , and losses, $L_i = 1 - G_i$, a figure of merit illustrated in Figure 10, was obtained. Note that in these calculations the noise of the down-conversion system T_3 has been fixed to 500 K. This figure of merit illustrates the dependence between the total noise

temperature of the system and the total gain for different noise temperatures of the optical system setup and the amplification subsystem.

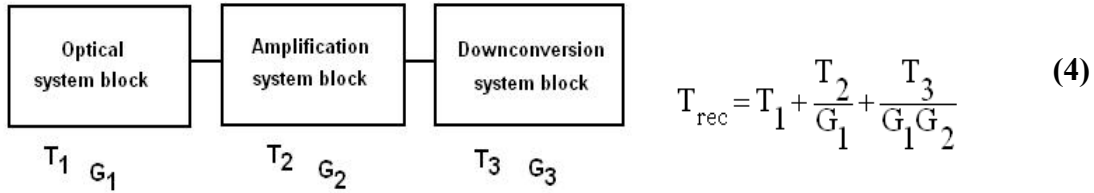


Figure 10. Simplified system noise block for the proposed receiver system presented in section 1.2.1. Here the T_1 is the optical system noise temperature; T_2 is the Low Noise Amplifier chain (i.e. amplification system part) overall noise temperature, and T_3 is the down-conversion system noise temperature.

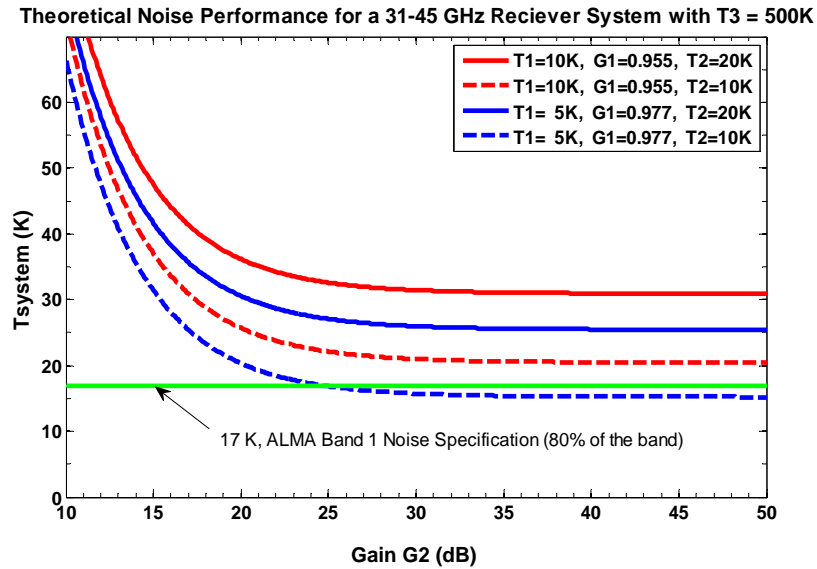


Figure 11. Theoretical receiver noise performance for the simplified system block diagram shown in Figure 10. Note that the horizontal solid line denotes the 17 K total receiver noise level specified for the ALMA Band-1 receiver system

As shown in Figure 9, the ALMA specification of 17 K for the Band-1 receiver will not be easy to reach. Even if the system incorporates the best and latest HEMT amplifier technology with high gain and low noise characteristics (see Table 5 in section 2 for HEMT technology examples used at similar/related frequency bands), the final total receiver system noise performance T_{system} will depend strongly also on the total noise contribution of the optical system. Hence, this thesis will be focused in how to design, optimize and construct an optical system that will contribute with the lowest noise level as possible to a 31–45-GHz receiver system.

1.3 Scope of this Thesis

The rest of this thesis is organized in 6 chapters. Chapter 2 describes existing radio-telescopes in other parts of the world that work in the same or similar frequencies range as the ALMA Band 1 receiver. This Chapter also describes some related research work that had important relevance for the design and construction of the horn and orthomodal transducer. Chapter 3 presents an overview of quasioptical techniques for designing optics in the microwave range, lens design and simulation, optical system noise budget verification, and its construction. Chapter 4 discusses the horn design and its optimization techniques (starting from the optical design developed in the previous chapter). The final constructed device, a very-compact corrugated horn with a spline-line profile, is presented. It is shown that gives excellent beam performances. The same chapter also presents the measuring results of the horn and the horn-lens system. Chapter 5 introduces us to the design, simulation, optimization, construction, and characterization of a dual-ridge Orthomodal Transducer (OMT). This OMT has a first and unique design of its kind, since it supports a large bandwidth in a very compact size. Moreover, this chapter also describes the design and construction of a very short circular-to-square waveguide transition (used to connect the horn and OMT), which can be easily built-in into the OMT block. Chapter 6 draws the final conclusions and describes the future work that can be continued from this rese

Chapter 2

Bibliographic Revision of Related Work

In this section some existing radio-telescope receiver technology, working in the range of the K and Q-bands are mentioned. Afterwards, it will follow that will be useful when designing and constructing our 31–45-GHz ALMA Band-1 optical system. It has already been decided that the most critical optical components such as lens, horn, circular to rectangular transition, and OMT are going to be designed, constructed and tested at our institution. On the other hand, the IR filters and isolators will be purchased from commercial suppliers. The standard waveguide dimensions that will be used to transport the RF signal from the OMT to the HEMT amplifier (and further on up to the mixer) is the standard WR-22 waveguide type. It supports optimal frequency transmission of the standard TE₁₀ Transverse Electrical mode in the range of 30 to 50 GHz [26].

2.1 Existing Radio-telescope Receivers at 31–45 GHz

There are several existing radio telescopes around the world working in frequency bands that are similar to the 31–45-GHz spectrum band. In Table 5 we summarize some of these telescopes that use HEMT amplifiers technology for detecting the received radio signals.

Table 7. Existing radio telescopes using HEMT technology and with similar receiver frequencies range as the ALMA Band-1 receiver.

Radio telescope name (Location)	Telescope type [Reference]	Frequency bands [GHz]	Bandwidth [%]	Best receiver noise temp. [K]
“Australia Telescope Compact Array” ATCA (Australia)	Interferometer [26]	30-50	50	30
“Cosmic Background Imager” CBI (Chile)	Interferometer [27]	26-36	32	15
Effelsberg (Germany)	Single dish [28]	27-36.7 41.6-44.4	30 6.5	20 73
“Extended Very large Array” EVLA (USA)	Interferometer [29]	26.5-40 40-50	40 22	40 48
“Q/U Imaging Experiment” QUIET (Chile)	Array [30]	26-40	42	20

Even though these telescopes work at cryogenic temperatures and use very similar amplification and down conversion systems than our proposed receiver, they defer in their optical configuration. In our case, the Band-1 receiver will need to use a lens placed in the front of the subreflector to refocus the beam waist into the horn, while for most of the other telescopes the subreflector connects the radiation directly into the feeder. In that sense, the main useful information that can be extracted from those references will be related to the design and construction of specific components in our receiver design.

2.2 Preliminary ALMA Optical Design

According to the ALMA specifications all the receiver bands must use optics that will not require any focusing system due to the fact that all the 10 receivers will be housed in a common cryocooled Dewar with fixed optical component. A preliminary optical design made by J. Lamb [31] for ALMA Band 1 is shown in Figure 11, where the OMT and some important dimensions are also included. It consists in a plano-convex spherical lens and a standard conical corrugated horn design with the IR filters located between these two components. The size and location of the components and the lens focal length are designed to fit the ALMA Cassegrain antenna focus (see section 1.1.4).

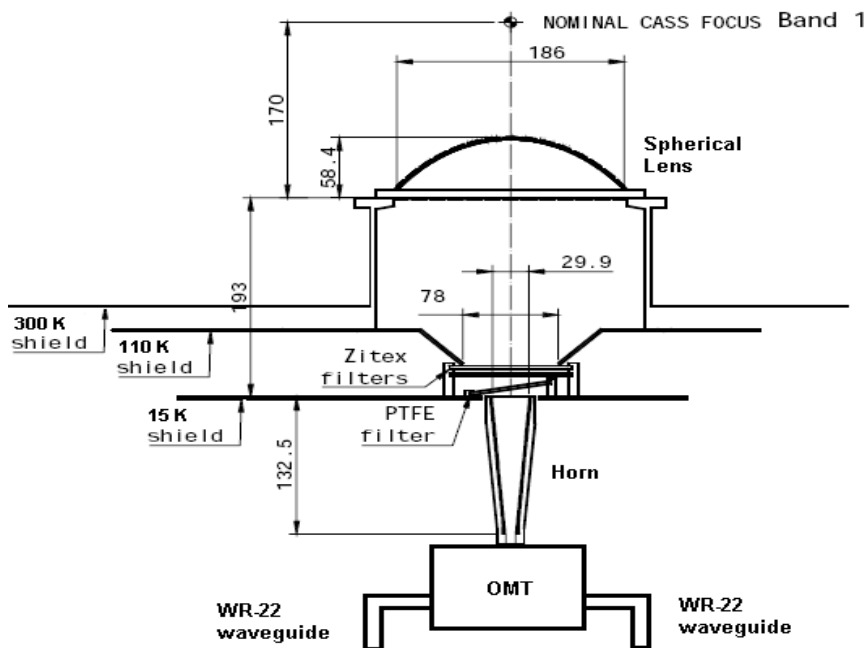


Figure 12. Preliminary ALMA Band-1 optical design showing the dimensions of the lens, filter, horn, and the OMT and how they are mounted in the top part of the cartridge. In this figure, one can also note the approximate location of the 15 K and 110 K stages of the cryocooler [31].

Since the type of lens used in this configuration is rather thick, it will result in high signal absorption and therefore it will generate a large amount of noise, a new thinner lens design is

being proposed in thesis project. This new lens design will also have a direct impact in the dimension and shape of the corrugated horn design showed in Figure 11.

2.3 Dielectric Lens and Quasioptical Ray Analysis

A dielectric “thick” lens (its thickness is proportional to the working wavelengths) will be the first element in our receiver system design since according to the ALMA Cassegrain-antenna specifications [32], the focus of the 31–45-GHz received signals will be located in between the subreflector mirror and the feed horn input and therefore the beam needs to be refocused into the horn. The optimal lens design can be carried out using the Fundamental Gaussian Beam Mode analysis [33]. The Fundamental Gaussian Beam Mode analysis, or “Quasioptics”, deals with the propagation of a beam of radiation that is reasonably well collimated but has relatively small dimensions when measured in a direction transversal to the axis of propagation in multiples of wavelengths. The Quasioptical mathematical formalism treatment can be found in [34].

There are three important considerations to take into account when designing a dielectric lens at mm frequencies and especially for this kind of optical system. First, the preferred lens profile is a convex bihyperbolic lens since, according to Goldsmith [34], it should preserve the phase of a large wave front (i.e. large beam waist) that is propagating through this lens design better than as it is in the case of a spherical lens choice [36]. Secondly, the lens material must have a large refractive index n and a low tangent loss δ [35], since they will determine the lens thickness. The lens thickness should be small as possible (but remembering that it should be not so small since this element will also act as a vacuum window) to minimize the noise contribution of the optics to the total receiver noise. Finally, at 38 GHz, which is the center frequency of the band, the lens focus at the right must coincide with the focussed *beam waist* position of the Cassegrain subreflector, and the other lens focus (left side), must be centred at the phase center position generated by the horn at the same (i.e. “focused optical system” [37]). Hence, the radiation coupling efficiency, c_{12} , between the subreflector and the horn will be maximized over the whole bandwidth and thereby it will be not necessary to realign the optics when changing frequency. Reflection at the lens surface can be minimized if circular grooves are cut in both sides of this component as they act as an antireflection layer [38].

A possible alternative to the bihyperbolic lens design is to use a so called *Zoned Lens* and *Zoned Plate Lens*, see Figure 12. Some advantages of such lens design are that this process reduces considerably the weight of the lens, and thereby it becomes thinner and have less power dissipation than the bihyperbolic lens design. On the other hand, these kinds of lenses have two major drawbacks. First, if they have a large diameter and if they work as a vacuum window, they may not hold large pressure since, due to its inhomogeneous surface, it could crack easily at their sharp concave edges (a hyperbolic lens is more robust in that sense). Its second major drawback is that they are bandwidth limited and could generate some phase distortion contribution at the focus that depends in the total number of zoned steps profile used in its construction [39].

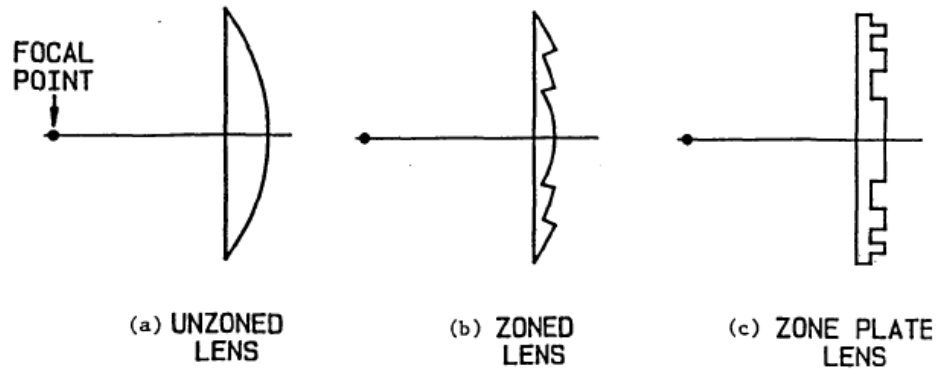


Figure 13. *Different lens design profiles. As it can be seen, the zoned lenses have a different transversal sections that make them thinner than a normal profile lens.*

Summarising then, our lens should support a large bandwidth (i.e. 30-45 GHz), it must be able to sustain a good vacuum and high pressure tolerance, must have low power losses (it will depend on the thickness of the lens and on the choice of dielectric material used in its construction), and finally, an antireflection surface treatment of both lens surfaces must be provided to minimize reflection losses.

2.4 Infra Red Filters

A radio astronomical cryogenic receiver requires the use of infrared (IR) filters to avoid that the external heat load contaminates the different internal cold stages of a Cryostat. The IR-filters main functions are to be fully transparent for the radio frequencies that are measured and to shield efficiently each one of the cryogenic stages from the IR radiation coming from the outside of the receiver. Inside the cryostat, the two radiation shields (15 K and 110 K) have circular apertures made in the cryostat wall where the IR filters are attached (see Figure 6). The 110 K stage filter will be made of PTFE [40]. On the other hand, the 15 K filter will be constructed using Gore-Tex, which is a kind of commercial expanded PTFE dielectric foam [41]. The dimensions and dielectrically properties of such IR-filters are summarized in Table 8.

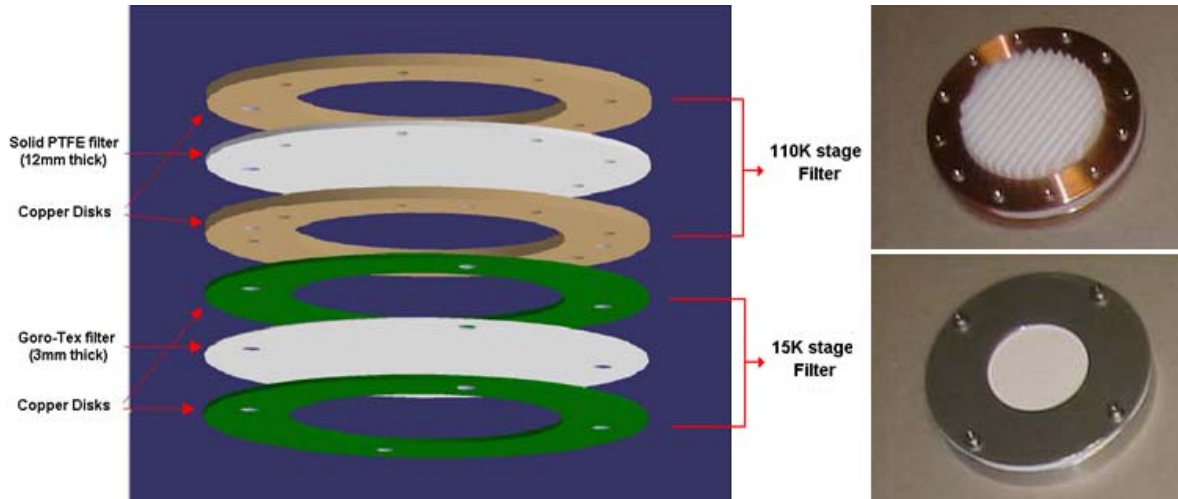


Figure 14. The left figure show a schematic filter representation showing the two main IR-filter stages with their corresponding materials and configurations. To the right, a real picture of the manufactured 110K (upper) and the 14K IR-filters (lower) [42].

As it can be seen in Figure 14, right figure, each one of the filters will be attached mechanically to their corresponding stages using two copper rings, one on the top and the other at its bottom, which help them to reach thermal equilibrium with their shields. The left part of Figure 13 correspond to a couple of pictures of such IR filters being constructed and delivered by the "Institut de Radio Astronomie Millimétrique", IRAM, in France for the ALMA Band1 [42].

Table 8. IRAM manufacturad Band1 Infra Red filter material properties and dimensions.

IR-filter type	Material	Dielectrical Properties ⁽¹⁾	Diameter and Thickness	Antireflection Layer
110K filter	PTFE	$n = 1.5$ $loss_tan = 3e^{-4}$	Diameter: 61 mm Thickness: 8.5 mm	Triangular machined grooved patterns on both sides (pitch = 4mm, slot depth = 3.5mm)
15K filter	Goro-Tex	$n = 1.2$ $loss_tan = 2e^{-4}$	Diameter: 40 mm Thickness: 3 mm	None

⁽¹⁾ data taken from reference [42].

2.5 Horn Design

A horn is a radiating/receiving electromagnetic element feed that is often used in microwave satellite communications systems or in radio astronomical receivers. The most typical feed used in this kind of applications is the so called “conical corrugated horn” whose main characteristic is that it supports a wide bandwidth over which both, the sidelobe levels and cross-polarisation are very low. Such horn structure comprises three main sections as it is shown in the bottom part of Figure 14. A circular waveguide input (that support the TE_{11} fundamental mode), a flare controlled conical corrugated section (supporting the HE_{11} mode) and an output throat section [43]. The corrugated section is divided in two subsections, the first from left to right (according to Fig. 14) is the mode launching section which has corrugation depths and teeth length of variable sizes, and secondly there is the thread section with a constant corrugation pattern. A good introduction to corrugated horn design can be found in references [95] and [44].

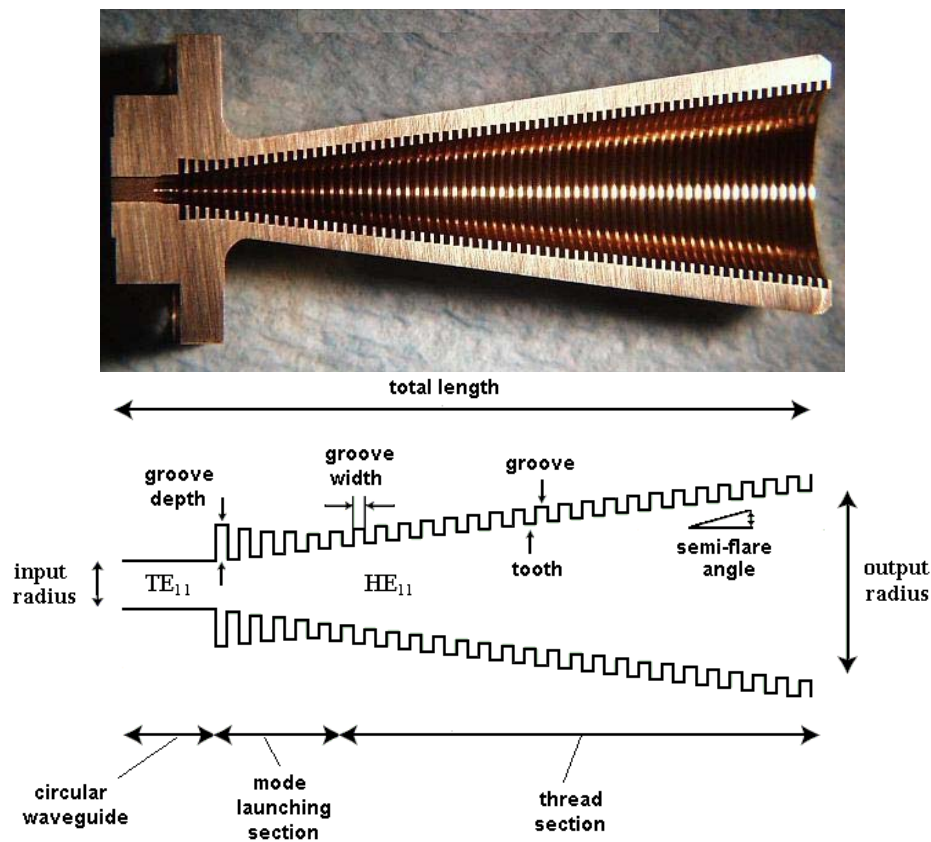


Figure 15. (Top) A typical conical corrugated horn cross section, showing its corrugation pattern. (Bottom) The main design parameters of such horn type.

The geometrical parameters shown in Figure 14 have a strong influence in the radiation pattern response and the overall performance of the designed horn [46]. For example, the semi flare angle size determines the phase center position of the beam and the generation of unwanted higher order modes [47]. The mode-launching section geometry is responsible of a smooth

transition mode conversion level [48]. The radiation pattern symmetry and cross-polar characteristics are defined by the shape of corrugation profile [49]. Finally, the total co-polar bandwidth of the received signal is determined by the size of the horn output aperture (e.g. the larger the more bandwidth it supports) [50].

By making an appropriate choice of flare angle, corrugated profile, mode-launching section type, and throat aperture size, an appropriate horn design can be developed for any receiver system.

There are two other horn alternatives types that are interesting to study and make good candidates for our system. The first one is the so called “Smooth-Walled Spline-Profile” horn developed by C. Granet [51]. In this design, the horn corrugations have been replaced by several cylindrical ring sections which increase in size as they reach the horn-output throat. As an example, see the horn profile geometry presented in Figure 15. Its main advantage is that it is easier to machine and presents good beam profile characteristics (e.g. low side lobes level) but cannot easily achieve a good cross-polar level as the corrugated horn design.

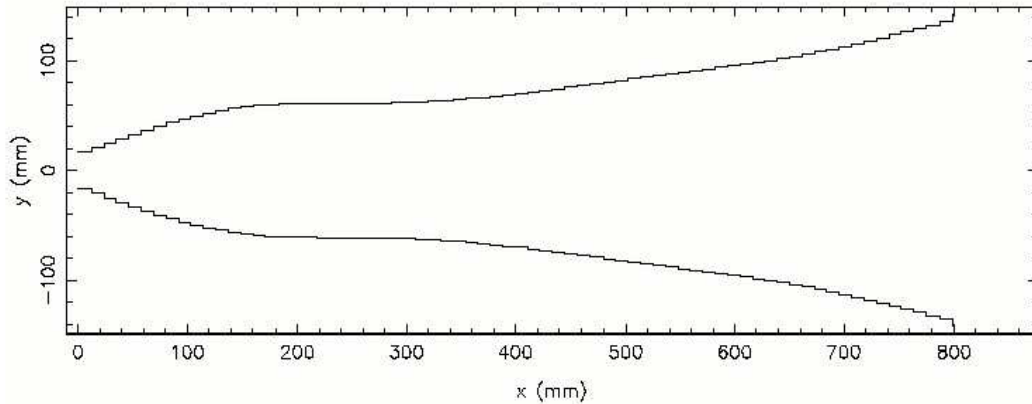


Figure 16. A schematic Smooth-walled Spline-line horn profile example taken from reference [52].

The second interesting alternative is a multi-sectional flare-angle-discontinuity “Potter horn” [53] with a complex flare angle discontinuity theory that is discussed in reference [54]. For example, see Figure 16. This type of horn presents great advantages from the manufacturing point of view since is easy to be machine from a single piece of metal block (no grooves are machined into the horn walls). Its exhibits excellent beam circularity and low cross polarisation over a relatively large bandwidth. However, in general, the more bandwidth the application requires, the more the number of sections that has to be added to the horn and therefore the more complex and time demanding will be the simulation.

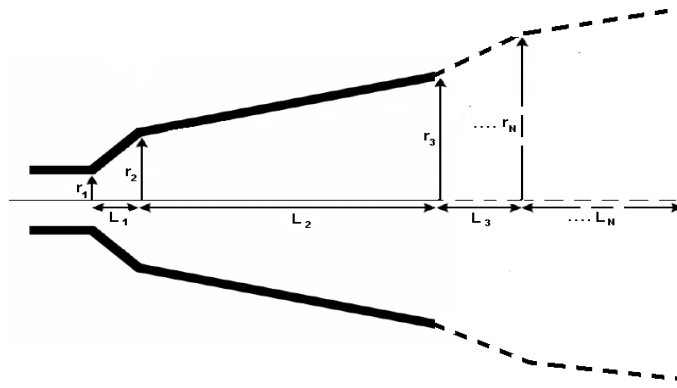


Figure 17. Geometry of the Potter horn (solid line) with r_N and L_N are the radius and the length of the N -th conical section.

2.6 Circular to Square Waveguide Transition

As it was discussed in the previous section the horn feed collects all the radiation that it is being received by the antenna dish and while the radiation is launched from the horn into the circular waveguide input port, the electromagnetic transmitted radiation suffers a mode transformation from HE_{11} into a TE_{11} mode. Now, the receiver system we are designing besides measuring the total receiver power of a signal at certain frequency, it is intended to analyze its polarization as well. To be able to accomplish that, the TE_{11} mode supported by the circular waveguide will be transformed into two orthogonal polarization channels TE_{10} and a TE_{01} using a special waveguide transform [55] that ends in a waveguide with square profile as the one shown in Figure 17. This transition is intended to be integrated in the final stage design of the OMT (see next section).

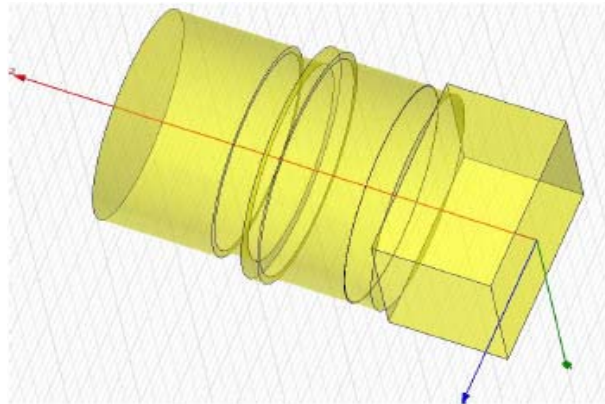


Figure 18. A typical schematic of a circular to square waveguide transition using a ring loaded transition design. The waveguide transform section serves to match the impedance transformer from the circular to the rectangular waveguide. The TE_{11} mode is transformed (i.e. decomposed) into a TE_{10} and TE_{01} orthogonal components [55].

2.7 Ortho-Modal Transducer (OMT)

In the mm and sub-mm spectral region, there are two main ways to separate the polarization of a signal. One is the quasi optical system mostly used at sub-mm wavelengths that uses a combination of mirrors and/or lenses, and a polarizer. The second way, applied for the mm wavelengths, is by using a special waveguide device called Ortho-Modal Transducer (OMT). The OMT is a waveguide passive component that separates the received astronomical signal into two orthogonal linearly-polarized components. It has three physical ports. One square input waveguide port which guides simultaneously the TE_{10} and TE_{01} modes (coming from the transition device discussed in the previous section) and two rectangular waveguide outputs that guide these modes independently through (a standard WR-22) rectangular wave guide. Using these two polarization channels that are amplified by independent amplification chains, one can estimate the 4 Stokes parameters of the incoming signal [56].

An interesting OMT design is the one based on the dual junction in rectangular waveguide introduced and described by Bøifot [57]. This design is shown in Figure 18, where the polarization modes TE_{10} and TE_{01} are filtered in the so called “Bøifot junction”. One polarization goes through the main arm and leaves the device at port 2, while the power of the second polarized signal is split in two and later on it is recombined at the power combiner part of the device. Basically what this junction does is that the thin septum and pins work as “linear polarizer” elements that filter out the unwanted signal component, “forcing” the signal to change direction, and letting the other pass without changing its direction of propagation (i.e. the port match its impedance). The main arm stepped transition and the side arms smooth taper designs, helps to adapt their impedance to a WR.22 standard waveguide section and therefore minimize the reflection losses.

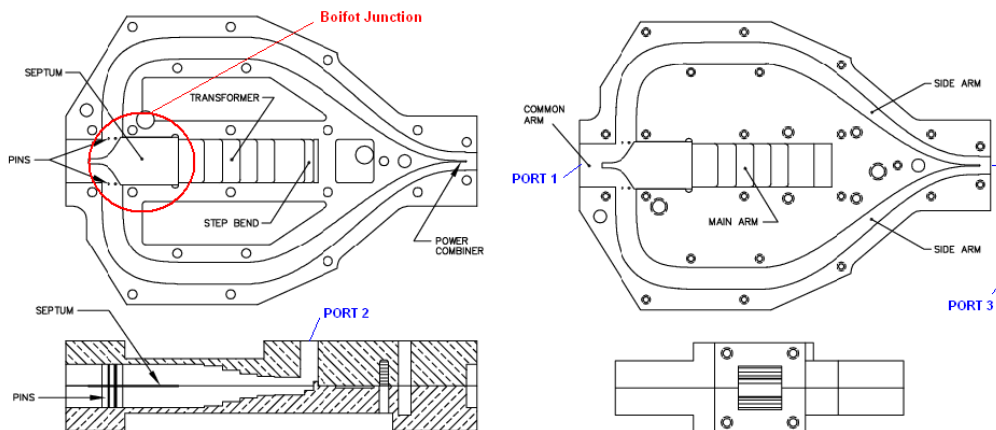


Figure 19. A WR42 Bøifot Junction OMT designed and constructed for an 18-26.5 GHz radio telescope of the National Radio Astronomy Observatory (NRAO) [58]. The diagram shows the principal components section and the input and output ports. The overall dimensions of the device are $102 \times 71 \times 23 \text{ mm}^3$.

A complete reference source related to the design of a Bøifot junction OMTs can be found in [59]. References related to the design of the OMT step transform section are found in [60], for

the Right-Angle-Miter Bends in [61][62] and power combiner in [63]. The OMT will be designed using Ansoft HFSS v11. It is important to mention that the main design objectives here, is to match the different waveguides transition to obtain low reflections and cross polarization values over the whole 31–45-GHz bandwidth.

Another interesting OMT design is the one developed by Asayama for the ALMA Band 4 and Band 8 receivers [64]. Figure 19 shows a schematic diagram of the device, which is based on a “Dual-Ridge” polarization divider transition [65] that has replaced the pins and the septum of the Boifot OMT and uses an E-plane split block power combiner waveguide circuit [66]. Figure 20 shows a real picture of such device, manufactured with a milling machine, using split-block technique, before and after being assembled.

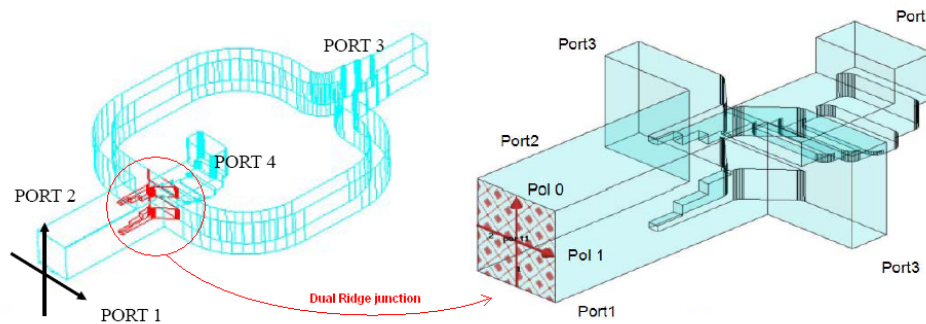


Figure 20. A schematic diagram of Asayama’s 125-163 GHz OMT showing its input and outputs ports (left figure). The “Double-Ridge” transform geometrical details are also shown in the right part of the figure [64].



Figure 21. Asayama’s Band-4 125--16-GHz OMT showing the two CNC machined split blocks (left picture) and the final assembled device (right picture) [64].

Finally, there is one more OMT design that could be useful for our purposes, this is the so called “Turstille Junction Orthomodal Transducer“ [64], which is shown in Figure 21. This OMT has the main advantage, similar to the Dual-Ridge OMT design, of having no pins or septum to be aligned. On the other hand, small misalignment errors on the 4-block sections could cause resonances inside the device.

Summarizing, there are 3 interesting OMT models that can be used for the design of our 31–45-GHz OMT and thereby be constructed using machined split block techniques. Probably Asayama’s OMT model has the great advantage since it only consists only of two machine block pieces that do not require any further integration and extra alignment effort as when using pins and a septum for the case of the Bøifot OMT design, or high alignment tolerance as in the turnstile OMT case.

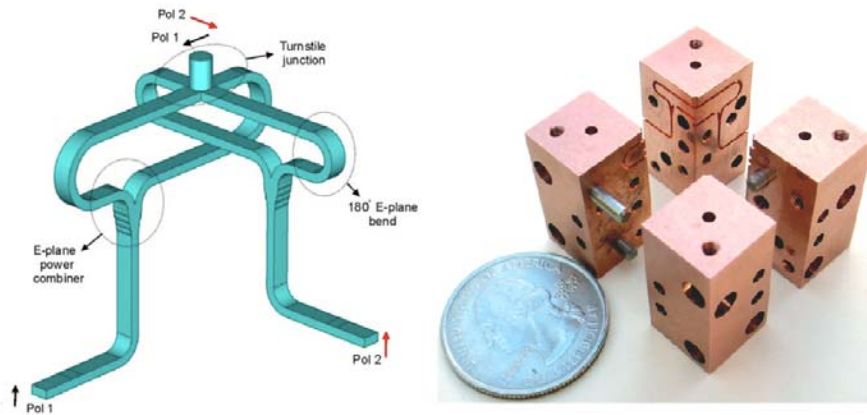


Figure 22. The “turnstile OMT” design (left) and a picture of a CNC-machined 4-section split blocks OMT, constructed for the CARMA 200-270 GHz radio receiver before being assembled (right) [64].

2.8 Manufacturing Techniques

This section discusses in brief the materials needed to construct the devices and the techniques needed to accomplish such processes.

2.8.1 Choice of Material

It is important to take into account the type of material that is going to be used when manufacturing the components. For the lens, the best likeable choice of dielectric would be Nylon, High Density Polyethylene HDPE, and Teflon, which are all very strong materials and suitable to be used as vacuum windows. HDPE is the best choice due to its high refractive index (i.e. the thickness of the lens will be low) and low attenuation losses (generate low intrinsic noise).

When thinking about the horn and the total length of the OMT’s internal waveguides, aluminum and copper are good candidates since, relatively, they are not expensive materials and are easy to machine. In addition, copper waveguides can be gold plated to decrease the losses and extend their lifetime since it will avoid rusting on the surface of the waveguide.

2.8.2 CNC Machine

To manufacture high demanding millimeter geometrical structures, such as the OMT split blocks, or to polish and create the antireflection coating grooves needed for the dielectric lens, our institution has purchased a high-precision CNC micro-milling machine from KERN Corporation [68]. Such machine, shown in Fig. 31, has the following features:

- Position accuracy: $< \pm 1\mu\text{m}$
- Position Scatter: $< \pm 1\mu\text{m}$
- Milling speed: 4000 rpm
- Number of axes: 5 independent axes



Figure 23. *The KERN high-precision Micro-Milli*

Chapter 3

Quasioptic Lens Design and Construction

The aim of this chapter is to provide information about the different aspects that involve the design, optimization and construction of a suitable optical system for the 31-to-45 GHz receiver that will be part of the prototype receiver for Band 1 of ALMA. Four optical layouts will be presented in this chapter section of the thesis. (1) A single HDPE lens that also acts as vacuum window – this is the original configuration [69]. (2) Two lenses forming a Gaussian beam telescope where the first lens is cooled. Finally and finally (3)(4) a single room temperature lens made of Quartz and other of Silicon lens, but using a common separate thinner vacuum quartz window, giving more freedom to the choice of material for the lens. In each scenario, the feed is represented as an optimum gain horn and first-order Gaussian beam analysis, i.e. Quasioptical, has been used to model the system. Each system is optimized for frequency independent illumination of the secondary and aperture efficiency, and then put into context through a comparison of the predicted receiver noise. Focus efficiency has been placed at a lower priority since it is assumed that the secondary can be refocused. All the theory presented here, unless mentioned otherwise, refers to [70].

3.1 Introduction

Quasioptic deals with the propagation of a beam of radiation that is reasonably well collimated but has relatively small dimensions when measured in wavelengths, transverse to the axis of propagation. The wavelength is proportional to the size of the object, meaning that there will be a focus with a waist instead of a point. It works over a sufficiently wide bandwidth where the so called “beam-waist radius” varies appreciably as a function of the distance. This theory is widely useful when designing mm and sub-mm wave components and systems and it takes care of the loss of power due to diffraction.

Ray optics use geometrical optics (i.e. straight lines) formulation when describing the propagation of the radiation beam. The wavelength is very small comparing to the size of the lens or other components and its focus is a point. Only one single frequency at the time is used when working with this theory and cannot explain diffraction phenomena. In contrast, *Wave optics* theory uses Maxwell Equations to solve the wave propagation of the radiation in very complex optical systems. Quasioptics come in between these two limiting cases. This allows the theory of the Gaussian beam modes and Gaussian beam propagation to be used.

When using Quasioptics to design the optical system for Band 1, one has to take into account the main specifications for this band [71]. They are summarized in Table 9.

Table 9. ALMA Band-1 optical system specifications (yields for all frequencies).

Parameter:	Specification:
Reflections:	< - 20 dB
Total Noise contribution	≤ 9 K
Total optical efficiency loss	≤ 9.9 %
Bandwidth	= 31-45 GHz
Illumination efficiency at Subreflector	= 12.3 dB

3.2 Quasioptical Theory

The theory behind Quasioptical Gaussian beams can be imagined as a beam essentially moving in the direction parallel to the propagation axis z (called paraxial beam) with a width that is not very large compared to the size of the propagating wavelength of radiation. This EM-field propagating in free space is described by Helmholtz-equation

$$\Delta\psi + k^2\psi = 0 \quad (5)$$

Where:

$$k = 2\pi/\lambda$$

If this beam is collimated (i.e. not too divergent), most of its EM-field phase will only have a z dependence. Thus the wave-function solution of Equation (5) can be written as:

$$\psi(x, y, z) = A(x, y, z)e^{i(\omega t - kz)} \quad (6)$$

Combining Equation (5) and (6), then:

$$\frac{\partial^2 A}{\partial x^2} + \frac{\partial^2 A}{\partial y^2} + \frac{\partial^2 A}{\partial z^2} - 2ik \frac{\partial A}{\partial z} = 0 \quad (7)$$

For a “ray”, the function $A(x,y,z)$ is not changing with z . This means:

$$\frac{\partial A}{\partial z} = \frac{\partial^2 A}{\partial z^2} \equiv 0 \quad (8)$$

But, In the Gaussian beam approximation, it can be assumed that:

$$\frac{\partial A}{\partial z} \neq 0 \quad \text{and} \quad \frac{\partial^2 A}{\partial z^2} \equiv 0 \quad (9)$$

This approximation is valid if:

$$\left| \frac{\partial^2 A}{\partial x^2} \right| \ll \left| 2ik \frac{\partial A}{\partial z} \right| \quad (10)$$

Thus, when combining these approximations with Equation (7), the result will be:

$$\frac{\partial^2 A}{\partial x^2} + \frac{\partial^2 A}{\partial y^2} - 2ik \frac{\partial A}{\partial z} = 0 \quad (11)$$

The solution to the above equation can be either expressed as a Gauss-Hermite function in Cartesian coordinates, or as a Gauss-Laguerre function in cylindrical coordinates. In Figure 27, the two lowest axially symmetric Gauss-Laguerre beam modes are shown. In cylindrical coordinates, taking into account only the lowest order mode solution [72], the solution is of the type:

$$\psi(x, y, z) = \psi_0 \frac{w_0}{w(z)} e^{-ir^2/w^2(z)} e^{-ikz - i\pi r^2/\lambda R(z) + i\phi(z)} \quad (12)$$

where:

ψ_0 = is the field amplitude

w_0 = is the 1/e radius where the beam has its minimum waist

z = is the distance from the position of the minimum beam waist

r = is the radial distance from the beam z axis ($r^2 = x^2 + y^2$)

λ = the propagated-beam wavelength

The different expressions in Equation (12) can be decomposed into several factors which can be interpreted as follows:

$\frac{w_0}{w(z)} \rightarrow$ yields the power conservation

$e^{-ir^2/w^2(z)} \rightarrow$ gives the Gaussian shape of the field distribution

$e^{-ikz} \rightarrow$ plane wave phase factor

$e^{-i\pi r^2/\lambda R(z)}$ → is a parabolic phase factor

$e^{+i\phi(z)}$ → is the phase slip parameter

The other parameters appearing in Equation (12), $w(z)$, $R(z)$, and $\phi(z)$, which define the principal characteristics and the shape of a symmetric fundamental Gaussian beam, are called the Gaussian beam parameters. Figure 24 illustrate the definition of such parameters.

The beam radius $w(z)$, of a Gaussian Beam is defined as:

$$w^2(z) = w_0^2 \left[1 + \left(\frac{\lambda z}{\pi w_0^2} \right)^2 \right] \tag{13}$$

Its radius of curvature $R(z)$, is given by:

$$R(z) = z \left[1 + \left(\frac{\pi w_0^2}{\lambda z} \right)^2 \right] \tag{14}$$

Finally, the phase shift of a Gaussian beam $\phi(z)$, is denoted:

$$\phi(z) = \arctan \left(\frac{\lambda z}{\pi w_0^2} \right) \tag{15}$$

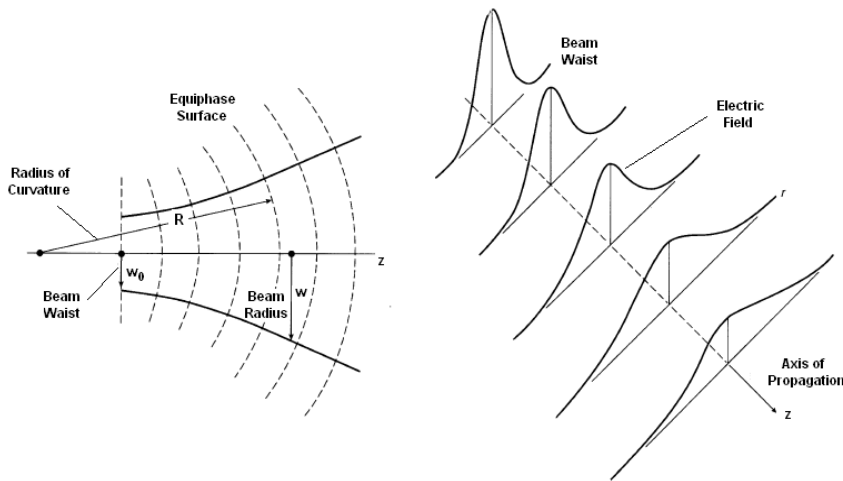


Figure 24. The Quasi-optical concepts of beam waist w_0 , beam radius w and radius of curvature R are illustrated at the left part of the figure. The electrical field cross-sections distribution as a function of z and the beam radius is shown at the right part of the figure.

The Rayleigh range or *confocal distance* defines the borderline between the near and the far field regions. For example, when $z \ll z_c$ the Gaussian beam is collimated. Otherwise, when $z \gg z_c$, the beam is divergent. This is defined as:

$$z_c = \frac{\pi w_0^2}{\lambda} \quad (\text{then } \rightarrow w(z) = \sqrt{2} \cdot w_0) \quad (16)$$

When $w(z) \rightarrow \infty$, Equation (13) can be rewritten as the *far-field divergence angle* θ_0 .

$$\theta_0 = \frac{w(z)}{z} = \frac{\lambda}{\pi w_0} \quad (17)$$

The meaning of this function is illustrated in Figure 25.

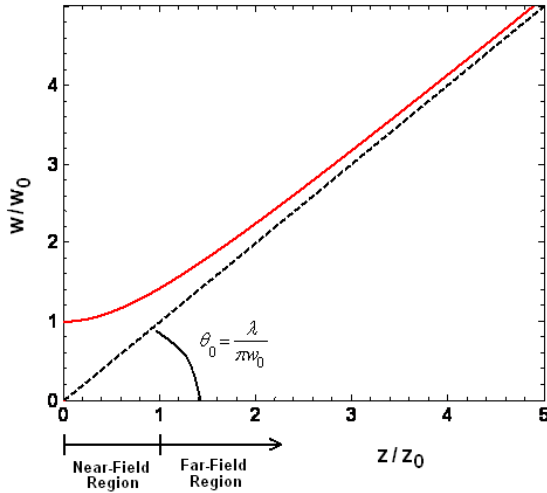


Figure 25. Quasioptical divergence angle θ_0 plot. When $z \rightarrow \infty$, then the beam radius start to grow linearly. The Far (i.e. Fresnel Region) and Near Field (i.e. Fraunhofer Region) regions and theirs boundary limit z_c , the Rayleigh range are also shown in the diagram. Adapted from reference [34].

Another important parameter is the *relative power density* distribution of a Gaussian fundamental mode which relates the losses of this EM-field distribution mode when passing through a circular aperture and part of its energy is beam truncated due to diffraction losses. It is defined as:

$$\frac{P(r)}{P(0)} = \exp\left[-2\left(\frac{r}{w(z)}\right)^2\right] \quad (18)$$

In Figure 26, the relative power density equation is being plotted as a function of different beam radius dimension related to the aperture size.

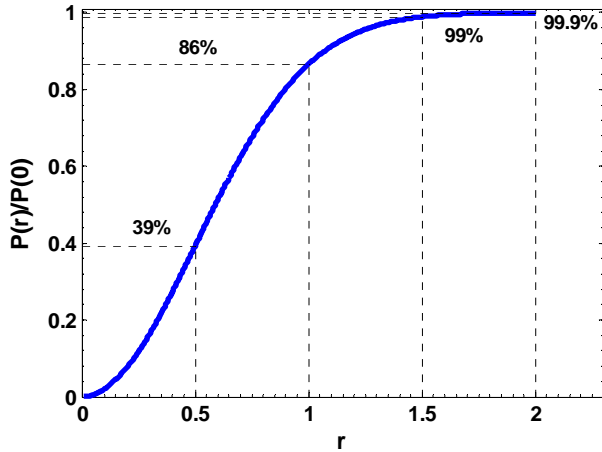


Figure 26. Fraction P_t/P_i of incident power P_i of a Gaussian beam transmitted through a circular aperture with radius a . For example to minimize the diffraction losses below the 0.1% limit, then the aperture dimension should be at least two times bigger than the beam radius at the aperture location.

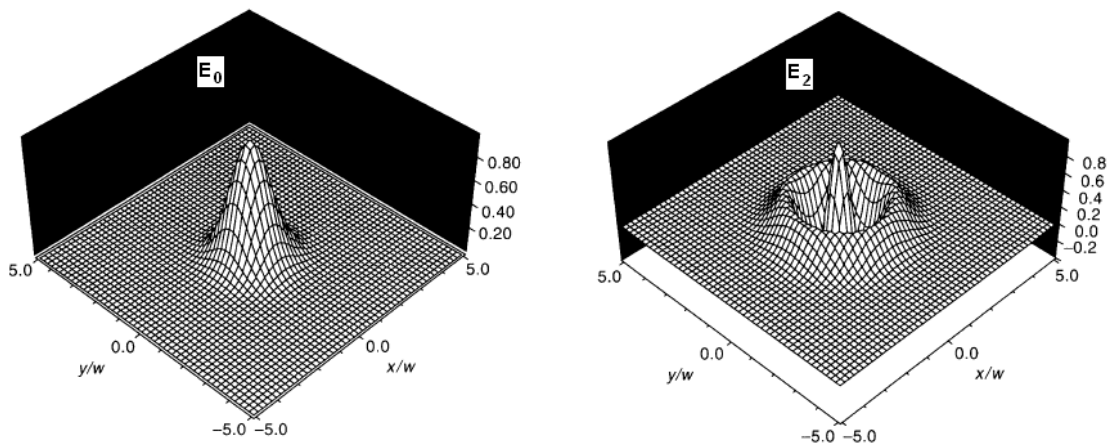


Figure 27. Two-dimensional normalized distribution of an axially symmetric Gauss-Laguerre Beam Mode. The fundamental electrical mode is described by the E_0 plot While the Second order mode corresponds to the E_2 plot. Both the E_0 and the E_2 Gaussian Beam Modes can be generated, for an example, by a corrugated conical horn. Thus, the fundamental mode generates about 98% of the total power irradiated by the horn while the second together with all the other higher order mode irradiate the remaining 2% [70].

Sometimes, in a Quasioptical system it is also important to calculate the coupling efficiency when two beams from different launchers interact. For the Band 1 optical system, this efficiency can be viewed as when the beam coming from the Cassegrain telescope focus is interacting with the beam generated by the horn together with some tertiary optical system (see Figure 28).

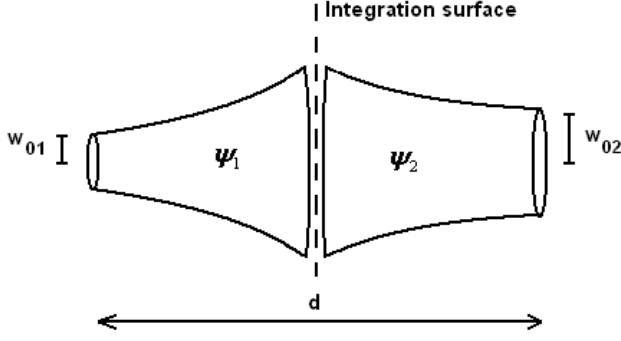


Figure 28. Coupling diagram between two Gaussian beams.

The coupling between the horn-optics and the antenna beams at a certain location along the optical axis will give the fraction of power transmitted from the first beam to the second one. The coupling is given by:

$$K_{12} = |C_{12}|^2 \quad (19)$$

where:

$$C_{12} = \langle \psi_1 | \psi_2 \rangle \equiv \int_{-\infty-\infty}^{\infty} \int \psi_1(x, y) \cdot \psi_2^*(x, y) dx dy = \int_0^{\infty} \int_0^{2\pi} \psi_1(r, \varphi) \cdot \psi_2^*(r, \varphi) dr d\varphi \quad (20)$$

In general, for two interacting Gaussian beams the coupling efficiency between them is given by:

$$K_{12} = \frac{4}{\left(\frac{w_{01}}{w_{02}} + \frac{w_{02}}{w_{01}} \right)^2 + \left(\frac{\lambda d}{\pi w_{01} w_{02}} \right)^2} \quad (21)$$

3.2.1 Focusing of Gaussian Beams (Thin Lens)

A thin lens acts as a phase transformer. The radius of curvature of the incoming beam R_1 is related to the radius of curvature of the outgoing beam R_2 by

$$e^{-j\frac{\pi r^2}{\lambda R_2}} = e^{+j\frac{\pi r^2}{\lambda f}} e^{-j\frac{\pi r^2}{\lambda R_1}} \quad (22)$$

where:

f = is the focal length of the lens

Hence, the thin lens equation will be given by:

$$\frac{1}{R_1} - \frac{1}{R_2} = \frac{1}{f} \quad (23)$$

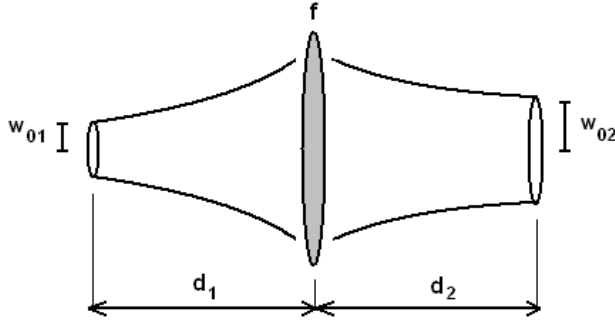


Figure 29. The Gaussian beam geometry refocused by a lens.

The sign of the radius of curvature is positive for a diverging beam when looking in the direction of propagation. Therefore, from the geometry of Figure 29, it follows that:

$$R_1 = R_1(d_1) = d_1 \left[1 + \left(\frac{z_{c1}}{d_1} \right)^2 \right] \quad R_2 = R_1(-d_2) = -d_2 \left[1 + \left(\frac{z_{c2}}{d_2} \right)^2 \right] \quad (24)$$

Not only does the phase of the beam need to be continuous at the lens but the beam radii must be equal at the lens:

$$w_1(d_1) = w_2(d_2) \quad (25)$$

Or in other words:

$$w_{01} \sqrt{\left(1 + \frac{d_1}{z_{c1}} \right)^2} = w_{02} \sqrt{\left(1 + \frac{d_2}{z_{c2}} \right)^2} \quad (26)$$

If now Equation (23) and (24) are combined:

$$\frac{1}{d_1 \left(1 + \frac{z_{c1}}{d_1}\right)^2} + \frac{1}{d_2 \left(1 + \frac{z_{c2}}{d_2}\right)^2} = \frac{1}{f} \quad (27)$$

Rearranging this equations its follows that:

$$d_2 = f \left[1 + \frac{\frac{d_1}{f-1}}{\left(\frac{d_1}{f-1}\right)^2 + \left(\frac{z_{c1}}{f}\right)^2} \right] \quad (28)$$

where:

$$Z_{c1} = \frac{\pi w_{01}^2}{\lambda} \quad (29)$$

Finally, combining Equation (26) and (27) it can be shown that:

$$w_{02} = \frac{w_{01}}{\sqrt{\left(\frac{d_1}{f-1}\right)^2 + \left(\frac{z_{c1}}{f}\right)^2}} \quad (30)$$

3.2.2 Gaussian Beam Telescope

The Gaussian beam telescope is a very useful optical system based on two lenses that if the input, intermediate, and output beam waists are located at the focal distance of the lenses as shown in Figure 30, then, the resulting input and output beam waist becomes frequency independent. Using Equation (28) and (30), the resulting relationship between w_{01} , w_{03} , f_1 , and f_2 will be the following:

$$d_1 = f \Rightarrow \begin{cases} d_2 = f \\ w_{02} = \frac{\lambda f}{\pi w_{01}} \end{cases} \quad (31)$$

and:

$$\left. \begin{aligned} w_{02} &= \frac{\lambda f_1}{\pi w_{01}} \\ w_{02} &= \frac{\lambda f_2}{\pi w_{03}} \end{aligned} \right\} \Rightarrow \frac{w_{03}}{w_{01}} = \frac{f_2}{f_1} \quad (32)$$

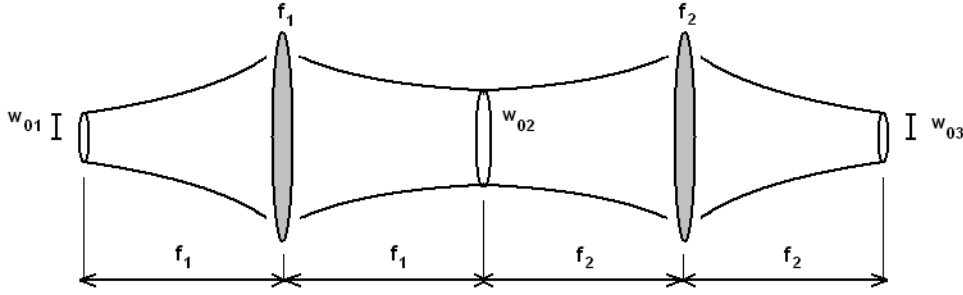


Figure 30. The Gaussian Beam Telescope. For this lens configuration, both, the input and the output beam waists are frequency independent. This will means that the resulting output beam waist will only depends on the input beam waist size and the lenses focal length magnitudes.

3.2.3 Thick Lens Corrections

Since a thin lens is practically impossible to construct, due to most of the dielectric materials (e.g. plastic materials) at mm wavelengths have low refractive index, and the size of the beam radius is closer to the sizes of the lens radius, a thicker lens that matches the wave-front phase of the incoming beam, is need it to be implemented. Such kind of lens that preserves the phase of the propagating beam is the hyperbolic lens surface. Another advantage of such lens is that it will be thinner (i.e.it will generate less noise). Other lenses with different surface designs, such as the spherical and the parabolic, will be thicker, and then, generate more unwanted noise.

In Figure 31 it is presented the geometry used to derive the hyperbolic lens profile. Here, it is required that the phase for the two ray paths F-P and F-Q, will be the same. In other words:

$$k_0 f + n k_0 t(r) = k_0 \sqrt{[f + t(r)]^2 + r^2} \quad (33)$$

where:

$t(r)$ = is the lens thickness that depends on the lens radius

n = the refraction index of the lens material.

r = the lens radius

f = the focal distance of the lens

k_0 = the wave number of the ray.

If Equation (33) is rewritten, then the hyperbolic function that describes the surface thickness of the lens with a given refractive index n , greater than 1 is:

$$t_{hyp}(r) = \frac{f}{n+1} \sqrt{1 + \frac{n+1}{n-1} \left(\frac{r}{f}\right)^2} - 1 \quad (34)$$

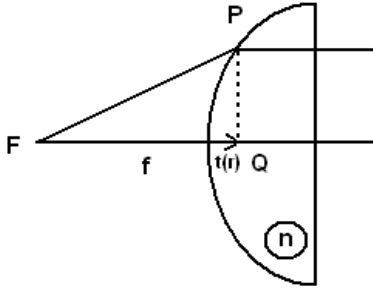


Figure 31. The geometry and the parameters needed to design the shape of a hyperbolic lens.

Or instead, equation (33) can also be expressed in term of the lens radius r :

$$r = \sqrt{(n^2 - 1)t_{hyp}^2 + 2f(n-1)t_{hyp}} \quad (35)$$

The lens thickness will be an essential parameter that it will be used to estimate the total noise contribution of such optical device (see section 3.2.1).

3.2.4 Gaussian Beam Launchers

The most efficient way to convert a waveguide transmitted signal into a Gaussian beam that propagates in free-space, and vice versa, is the use of a converter device called corrugated horn. Its launching efficiency is of about 98% and offers a wide bandwidth and low cross-polar performances [73].

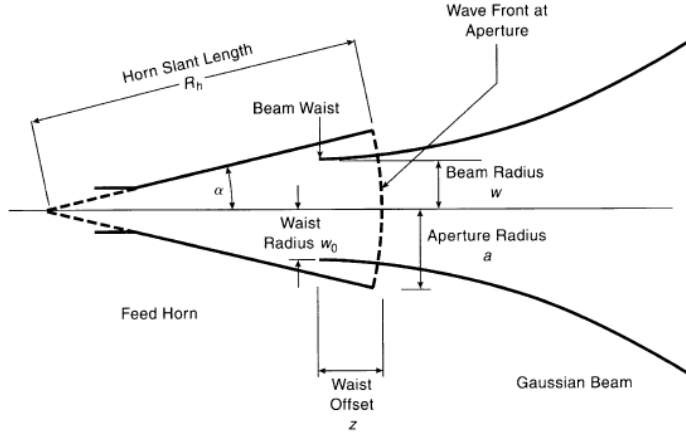


Figure 32. A feed horn launching a Gaussian Beam and its designing parameters. Adapted from reference [70].

An optimal conical corrugated horn will generate a symmetrical E and H radiated field. The beam waist at the horn aperture w and its corresponding radius of curvature R can be approached as:

$$w = 0.644a \quad (36)$$

$$R = R_h \quad (37)$$

where:

a = the horn aperture radius

R_h = horn Slant length (see Figure 32)

Putting these values in Equation (13) and (14) and rearranging them, the beam-waist size w_0 and the beam-waist position z , inside the horn can be retrieved:

$$w_0 = \frac{0.644a}{1 + \left[\pi(0.644a)^2 / \lambda R_h \right]^2} \quad (38)$$

$$z = \frac{R_h}{1 + \left(\lambda R_h / \pi(0.644a)^2 \right)^2} \quad (39)$$

3.2.5 Complex Beam parameter and Ray Matrices

The design of a complete Quasioptical system can be carried out easily and faster with the help of the ABCD transfer matrix formalism [74] and the MATLAB numerical programming language [75]. An input ray that is passing through an optical element, will be transformed by means of a geometrical optic linear transformation into an output ray according to:

$$\begin{aligned} r_{out} &= A \cdot r_{in} + B \cdot r'_{in} \\ r'_{out} &= C \cdot r_{in} + D \cdot r'_{in} \end{aligned} \quad (40)$$

In Matrix formalism, this can be rewritten as:

$$\begin{bmatrix} r_{out} \\ r'_{out} \end{bmatrix} = \begin{bmatrix} A & B \\ C & D \end{bmatrix} \cdot \begin{bmatrix} r_{in} \\ r'_{in} \end{bmatrix} \quad (41)$$

where the A, B, C, and D constants, for the 2x2 ray Matrix, are given by :

$$\begin{aligned} A &= \partial r_{out} / \partial r_{in} \\ B &= \partial r_{out} / \partial r'_{in} \\ C &= \partial r'_{out} / \partial r_{in} \\ D &= \partial r'_{out} / \partial r'_{in} \end{aligned}$$

There is a similarity between the complex Gaussian beam parameter q and the radius of curvature R of geometrical optic. The latter is defined as:

$$R_{out} = \frac{\text{position}}{\text{slope}} = \frac{r_{out}}{r'_{out}} = \frac{A \cdot r_{in} + B \cdot r'_{in}}{C \cdot r_{in} + D \cdot r'_{in}} = \frac{A \cdot R_{in} + B}{C \cdot R_{in} + D} \quad (42)$$

Now, extending this formalism into a Gaussian beam transformation we have:

$$q_{out} = \frac{A \cdot q_{in} + B}{C \cdot q_{in} + D} \quad (43)$$

where q_{in} is defined as a function of the confocal distance (equation (16)):

$$q_{in} = jz_c$$

From this value, the complete set of parameters describing a Gaussian beam, just as the beam radius, w , and radius of curvature, R , can be retrieved:

$$w = \left[\frac{\lambda}{\pi \operatorname{Im}(1/q)} \right]^{0.5} \quad (44)$$

$$R = \left[\operatorname{Re} \left(\frac{1}{q} \right) \right]^{-1} \quad (45)$$

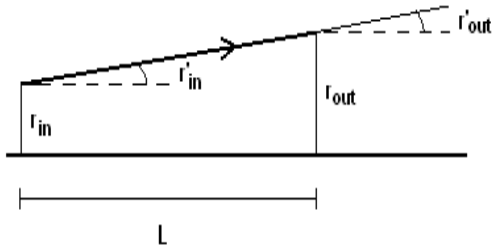


Figure 33. Distance L in uniform propagating medium.

One of the simplest Matrix that can be derived, for example, is an optic element with a distance L that travels a uniform medium with an index of refraction n (see Figure 33 for the geometry):

$$\begin{aligned} r_{out} &= A \cdot r_{in} + B \cdot r'_{in} = r_{in} + L/n \cdot r'_{in} \\ r'_{out} &= C \cdot r_{in} + D \cdot r'_{in} = 0 + r'_{in} \end{aligned} \quad (46)$$

This transformed into a Matrix gives:

$$\begin{bmatrix} A & B \\ C & D \end{bmatrix} = \begin{bmatrix} 1 & L/n \\ 0 & 1 \end{bmatrix} \quad (47)$$

A second, a very useful example, will be a curved interface element from a medium with refractive index n_1 to another with n_2 (see Figure 34):

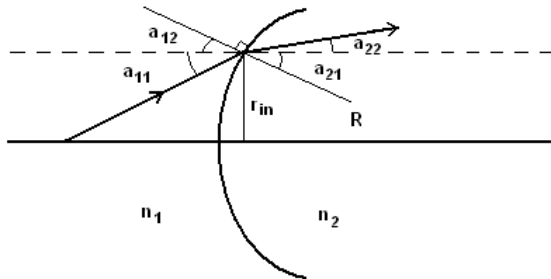


Figure 34. Curved interface with $n_1 < n_2$.

From the drawing in Figure 35 and using the Snell law [74]:

$$n_1 \cdot \theta_1 = n_2 \cdot \theta_2 \Rightarrow n_1 \cdot (\alpha_{11} + \alpha_{12}) = n_2 \cdot (\alpha_{21} + \alpha_{22}) \quad (48)$$

And since:

$$\alpha_{12} = \alpha_{21} = \frac{r_{in}}{R} \quad (49)$$

Then, combining Equation (48) and (49):

$$n_1 \cdot \left(\alpha_{11} + \frac{r_{in}}{R} \right) = n_2 \cdot \left(\alpha_{22} + \frac{r_{in}}{R} \right) \Rightarrow \alpha_{22} = r_{in} \cdot \left(\frac{n_2 - n_1}{n_2 \cdot R} \right) + \frac{n_1 \cdot \alpha_{11}}{n_2} \quad (50)$$

Comparing the previous results with the general input-output geometrical linear transformation of the type:

$$\begin{aligned} r_{out} &= A \cdot r_{in} + B \cdot r_{in}' = r_{in} \\ r_{out}' &= C \cdot r_{in} + D \cdot r_{in}' = \left(\frac{n_2 - n_1}{n_2 \cdot R} \right) \cdot r_{in} + \frac{n_1}{n_2} \cdot r_{in}' \end{aligned} \quad (51)$$

The resulting linear Matrix element of a curved surface will be:

$$\begin{bmatrix} A & B \\ C & D \end{bmatrix} = \begin{bmatrix} 1 & 0 \\ \frac{n_2 - n_1}{n_2 \cdot R} & \frac{n_1}{n_2} \end{bmatrix} \quad (52)$$

If a thick lens ABCD transfer matrix needs to be found, the linear combination of the following three matrices will give the resulting optical element:

$$M_{thick-lens} = M_3 \cdot M_2 \cdot M_1 \quad (53)$$

where:

M_1 = curved interface from refractive index n_1 to n_2 with radius of curvature R_1

M_2 = distance d in an uniform medium with refractive index n_2

M_3 = curved interface from refractive index n_2 to n_1 , with radius of curvature R_2

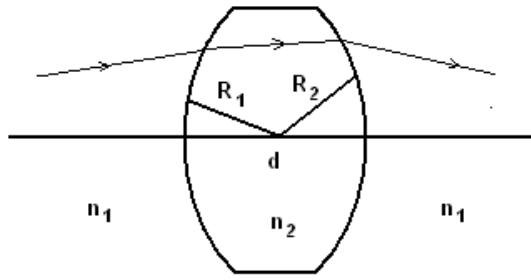


Figure 35. The thick lens geometry showing its main designing matrix parameter.

Putting everything together then, the final lens ABCD Matrix will be:

$$M = \begin{bmatrix} 1 & 0 \\ \frac{n_1 - n_2}{n_1 R_2} & \frac{n_2}{n_1} \end{bmatrix} \cdot \begin{bmatrix} 1 & d \\ 0 & 1 \end{bmatrix} \cdot \begin{bmatrix} 1 & 0 \\ \frac{n_2 - n_1}{n_2 \cdot R_1} & \frac{n_1}{n_2} \end{bmatrix} = \begin{bmatrix} 1 + \frac{(n_2 - n_1)d}{n_2 R_1} & \frac{dn_1}{n_2} \\ -\frac{1}{f} - \frac{d(n_2 - n_1)^2}{n_1 n_2 R_1 R_2} & 1 + \frac{(n_1 - n_2)d}{n_2 R_2} \end{bmatrix} \quad (54)$$

Where:

$$\frac{1}{f} = \frac{n_2 - n_1}{n_1} \cdot \left(\frac{1}{R_2} - \frac{1}{R_1} \right) \quad (55)$$

In Table 10, below, a summary of the most important ray Matrices that will be useful in this thesis are listed.

Table 10. Matrix Formalism of Some Basic Optical Elements [70].

Matrix Element	Matrix Formalism	Comments
Translation	$\begin{bmatrix} 1 & L \\ 0 & 1 \end{bmatrix}$	L = the distance traveled in medium with index of refraction n
Refraction	$\begin{bmatrix} 1 & 0 \\ \frac{n_2 - n_1}{n_2 R} & \frac{n_1}{n_2} \end{bmatrix}$	R = surface radius of curvature +R for a convex surface -R for a concave surface n ₁ = air refraction index n ₂ = materials refraction index
Mirror	$\begin{bmatrix} 1 & 0 \\ \frac{2}{R} & 1 \end{bmatrix}$	R = mirror radius of curvature +R for a convex surface -R for a concave surface

Thin Lens	$\begin{bmatrix} 1 & 0 \\ \frac{1}{-f} & 1 \end{bmatrix} \quad (56)$	$\frac{1}{f} = \frac{n_2 - n_1}{n_1} \cdot \left(\frac{1}{R_2} - \frac{1}{R_1} \right)$ <p>+f for a concave surface -f for a convex surface</p>
Thick Lens	$\begin{bmatrix} 1 + \frac{(n_2 - n_1)d}{n_2 R_1} & \frac{dn_1}{n_2} \\ -\frac{1}{f} - \frac{d(n_2 - n_1)^2}{n_1 n_2 R_1 R_2} & 1 + \frac{(n_1 - n_2)d}{n_2 R_2} \end{bmatrix}$	<p>d = Lens thickness R₁, R₂ and n₁, n₂ are index of refractions respective radius of curvatures according to Figure 35 f = see its Thin Lens definition</p>

3.2.6 Dielectric Materials Properties

The dielectric constant of an optical material is the complex vectorial sum of one real and another imaginary term given by [74]:

$$\varepsilon = \varepsilon' - j\varepsilon'' \quad (57)$$

where:

ε' = real part of the dielectric constant

ε'' = imaginary part; loss factor

If a plane wave of radiation with a initial power equals to P_{in} with a wavelength equal to λ_0 is passing through a dielectric slab with a thickness t , then the loss of power due to the loss factor of the dielectric will be:

$$P_{out} = P_{in} \exp(-\alpha t) \quad (58)$$

where:

$$\alpha = \frac{2\pi \tan \delta}{\lambda_0} \quad (59)$$

and the tangent loss of the material is:

$$\tan \delta = \frac{\varepsilon''}{\varepsilon'} \quad (60)$$

Equation (59) will be very useful when estimating the total loss of power in form of contributed added noise to different simulated optical systems that will be discussed in the next section.

3.2.7 Quasioptical treatment of Cassegrain Antennas

There are a number of important concepts that briefly resume and cover the principal aspects of the Cassegrain antenna theory [76] where Gaussian optics and classical optic treatment are combined according to [77]. The *radiation pattern* indicates the variations of the antenna *gain* with direction. It is usually represented graphically for the *far field* conditions, where the radiation angular field distribution is essentially independent of the distance from the source, in either horizontal or vertical plane. In Figure 36, the radiation pattern of a circular aperture or reflector directional antenna is schematically shown. For the case of the ALMA Cassegrain antennas, due to its large main-dish diameter, most of its radiated power is concentrated along the main lobe, and it is this part of the antenna radiation that is been concentrated in the subreflector and then coupled into the receivers. This also simplifies the Quasioptical analysis since it will be treated as on-axis optical system making the off-axis feed aberrations in ALMA Cassegrain Antennas very small as it will be discussed in the next section.

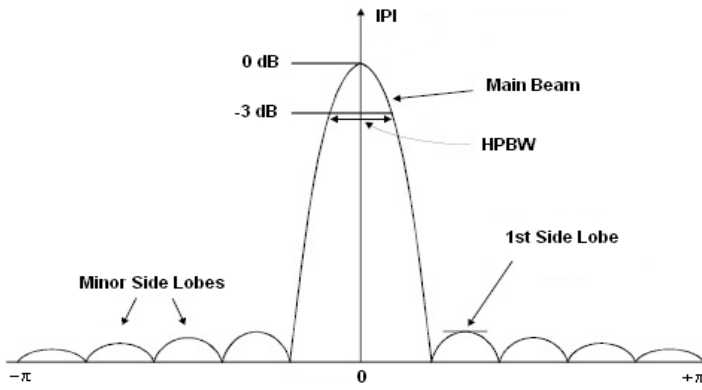


Figure 36. Typical antenna radiation pattern for a circular reflector antenna of diameter D showing the corresponding main and side lobes.

The angle between the directions at which the main-lobe antenna gain falls to half of its maximum is called *The Half Power Beam Width* (denoted HPBW). This angle is given approximately by:

$$\theta_{3dB} = 75 \frac{\lambda}{D} \quad [\text{degrees}] \quad (61)$$

Where:

D = antenna diameter [m]

λ = the wavelength of the signal being observed [m]

The *directivity* of such antenna is a figure of merit that measures the total power density that the antenna radiates in the direction of its strongest emission, compared with the same total power density radiated by an ideal *isotropic radiator* [78]. Mathematically, the equation for the antenna directivity is given by:

$$D = \frac{1}{\frac{1}{4} \int_0^{2\pi} \int_0^{\pi} |F(\theta, \phi)|^2 \sin \theta d\theta d\phi} \quad (62)$$

where:

$F(\theta, \phi)$ = normalized radiation pattern as a function in spherical coordinates.

Now, there is one particular parameter that is very close to the directivity and it is the *gain* of an antenna. This is defined as the directivity of the antennas multiplied by the antenna *efficiency*. The gain is maximal in the direction of maximal radiation. It is expressed according to the following equation:

$$G = F(\theta, \phi) \eta_A \quad (63)$$

where:

η_A = antenna total efficiency.

The antenna efficiency is defined as the ratio between the effective area of the antenna and the geometrical one (i.e. the real reflector area of the main dish antenna). The effective area is the total area of the dish antenna that is really been used when the radiation is coupled into the antenna feed. This value is always less than unity and for our Cassegrain antenna its efficiency will depends on several terms as it is stated in:

$$\eta_A = \eta_i \eta_s \eta_b \eta_p \eta_f \eta_e \eta_o \quad (64)$$

where

η_i = illumination efficiency of the aperture by the feed function

η_s = spillover efficiency of the feed and subreflector

η_b = blocking efficiency due to quadripod, subreflector, other obstruction.

η_p = polarization efficiency of the feed-reflector combination

η_f = focus error efficiency (both lateral and axial defocus)

η_e = surface error efficiency (“Ruze loss”), also called scattering efficiency

η_o = radiation efficiency of the reflector surface (ohmic loss)

In general, the principal causes of the gain degradation in a symmetrical Cassegrain antenna will be determined by its illumination efficiency, η_i , the spillover efficiency, η_s , and the blocking efficiency, η_b . The *illumination efficiency* express the power loss of a signal due to a field across the secondary which have not uniform amplitude and not being in phase over it. The *spillover efficiency* is the fraction of the total power that radiated by the tertiary optics that is being intercepted and collimated by the subreflector dish. On the other hand, the *blockage efficiency* represents the reduction in the aperture efficiency due to the subreflector central

obstruction. These 3 efficiencies can be estimated according to the antenna diagram appearing in Figure 37 and the following equations:

$$\eta_i = 2\alpha^{-1} \frac{[1 - \exp(-\alpha)]^2}{1 - \exp(-2\alpha)} \quad (65)$$

$$\eta_s = 1 - \exp(-2\alpha) \quad (66)$$

$$\eta_b = \frac{[\exp(-f_b^2 \alpha) - \exp(-\alpha)]^2}{[1 - \exp(-2\alpha)]^2} \quad (67)$$

where α and f_b , are the *edge taper* and the *blockage region* given by:

$$\alpha = \left(r_s / w_s \right)^2 \quad (68)$$

$$f_b = r_s / r_a \quad (69)$$

r_a = antenna main dish radius.

r_s = antenna subreflector radius.

w_s = radiation beam radius over the subreflector

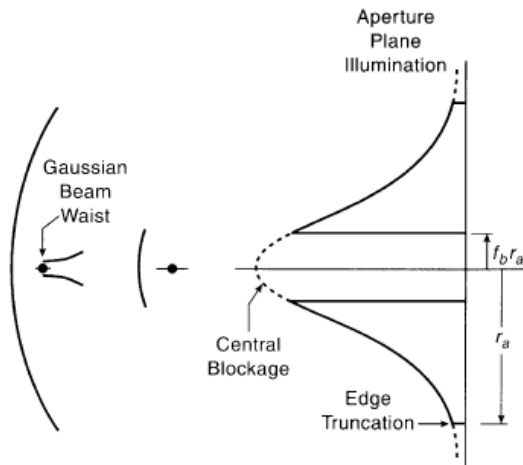


Figure 37. On axis Cassegrain antenna system been illuminated by a Gaussian Beam radiation field pattern. This figure shows also the effect of edge truncation and central blockage of such radiation field due to the central blockage region of the antenna subreflector. Adapted from reference [70].

Now, from the other 4 remaining efficiencies, probably the polarization efficiency η_p and the focus efficiency η_f are the most important to be studied in our case since both efficiency factors will deteriorate the quality of our experimental horn-lens radiation pattern measurements that will be discussed in chapter 4. The *polarization efficiency* is the factor expressing the loss of power signal over its cross-polar component, while the *focus efficiency* factor denotes the signal power loss due to radial or axial focus errors of the tertiary optics relative to the subreflector. Finally, both the “*Ruze loss*” [79] and the “*Ohmic loss*” can be neglected, i.e. both efficiencies set to be equal to 1. For the case of the Ruze loss this approximation is valid since the wavelengths in question for the Band-1 receiver are too large comparing with how the lens surface accuracy can be manufactured with today’s CNC machines. For case of the Ohmic loss, this factor can only be estimated once the whole receiver-band is installed in the Cassegrain antenna.

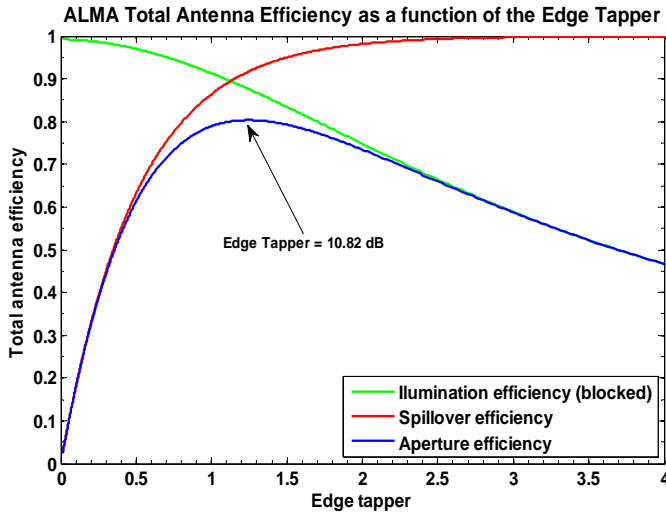


Figure 38. Total antenna efficiency for the ALMA antennas. The efficiencies in this picture were estimated using the values summarized in Table 3. Here $f_b = 0.0625$ and the “blocked” illumination efficiency is the product between illumination efficiency η_i and the blockage efficiency η_b .

In Figure 38 one can observe how the 3 main efficiencies simulated for the 12m ALMA Cassegrain antenna, with a blockage f_b of 0.0625, will have their maximum antenna efficiency of 0.8034 when its edge tapper is 10.82 dB.

3.2.8 Off-axis Feed Aberrations in Cassegrain Antennas

Since the position of all ALMA receivers, inside the cryostat, are located around the central axis of the Cassegrain antenna, optical aberrations will be introduced and it will degrade the antenna performance. This loss of antenna efficiency due to lateral receiver band displacement will be reduced since the center of the subreflector can be re-pointed towards the center of the receiver feed horn making its field amplitude symmetric to a first-order approximation [70].

According to [80], the total antenna efficiency loss due to the receiver bands off-axis displacement was estimated using classical optical aberration theory [81]. This model used the so called Seidel function which takes into account four aberration terms, namely, astigmatism, curvature, distortion, and coma, and treated the 12-meter ALMA Cassegrain Antenna as an equivalent prime focus telescope using the input parameters f , D , M and F that are stated in Table 3, section 1.1.5. It was shown then, that terms of curvature and distortion vanished and that the total antenna efficiency loss was much less than 1 % once the subreflector optical axis was re-pointed towards the center of the Band-1 feed Horn and placing the position of the same on the Petzval surface [77] .

Hereby in this document, it will be assumed in this work that the antenna efficiency loss due to astigmatism, curvature, distortion and coma are negligible and will not be further discussed or take into account when analyzing the experimental measurement results that will be presented in the next sections. However, it will be of interest to estimate how much the antenna subreflector needs to be adjusted when, for example, the subreflector is been tilted to illuminate the center of the Band-1 receiver horn and find the best axial focus to optimize the antenna efficiency. This can be done using the well known Cassegrain antenna *magnification* M and *focal shift* ΔS equations given by:

$$M = \frac{f_e}{f_m} = \frac{\tan(\phi_v)}{\tan(\phi_r)} = \frac{L_r}{L_v} = \frac{e+1}{e-1} \quad (70)$$

where (see Figure 39 for details):

f_e = antenna effective focal length

f_m = antenna main dish focal length

ϕ_v = half angle subtended by the primary

ϕ_r = half angle subtended by the secondary

L_r = back focal distance

L_v = distance between main dish foci and the secondary apex

e = eccentricity of the hyperbola

The focal shift is defined as [70]:

$$\Delta S \cong -M^2 \delta \quad (71)$$

where:

δ = is the subreflector displacement

$M = 20$

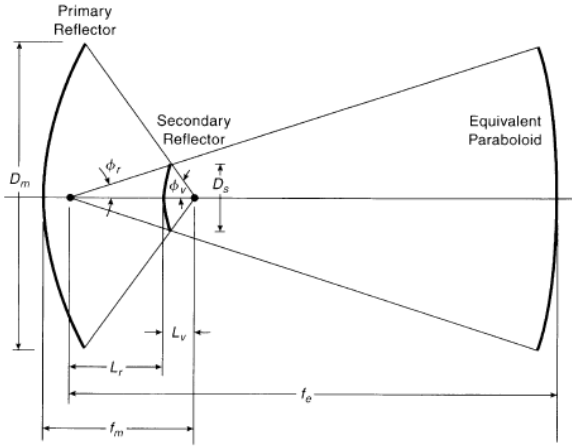


Figure 39. The geometry and the most relevant parameters for the calculation of the magnification M and the focal shift ΔS of a Cassegrain Antenna. Adapted from reference [70].

Observe that if the secondary focus needs to be known, then from the regular diverging lens convention, its focus f_s is given by:

$$\frac{1}{f_s} = \frac{1}{L_r} - \frac{1}{L_v} \quad (72)$$

3.3 Optical System Design Examples and Their Noise Estimation

First, in this section, we will present the detailed position of the ALMA Band-1 receiver with respect to the ALMA cryostat, the subreflector, and the free space that remains between the top plate of the cryostat and the ALMA Calibration Device (ACD) that it will set the constraints of how the Band-1 optical system can be designed and located. As it is discussed in [82], this optical system will need a refocusing element between the horn and the subreflector that will makes the launched beam-waist size inside the feed horn small enough, so the size of the horn becomes not too large and thereby be placed together with the other receiver elements (such as the OMT and the HEMT amplifier) on top of the 14-K receiver shield.

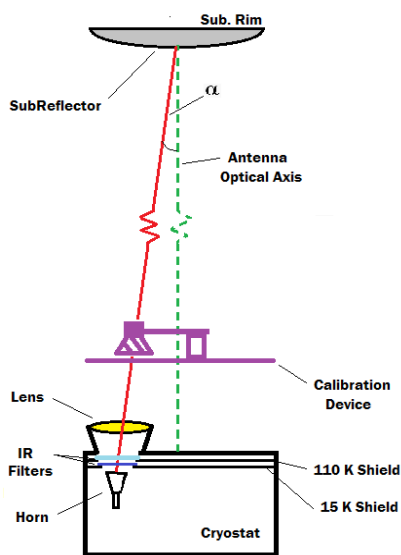
Secondly, in the next part of this section, four different optical layout candidates for the ALMA Band1 receiver will be presented. They use one or two dialectical lenses, and sometimes a vacuum window. In each one of the cases, the system will be optimizing by illuminating the radiation at the subreflector with 12.3 dB of edge taper at all frequencies [70] and, then, the best optical system will be selected according to the lowest estimated total noise contribution to the receiver. Observe that a couple of mirrors could also be used to refocus the beam into the receiver, but since the used wavelengths in question are large (large beam waist diameter requires large mirrors) and the space to place the optics without blocking the other bands is very limited, then the preferred solution for this particular optical system design is the use of lenses as refocusing elements.

3.3.1 Optical Dimensions between Receiver and Subreflector

The receiver and the subreflector locations and dimensions of the different optical parameters used to design this band are presented in this section. Those values are of importance when estimating the truncation losses and the edge taper of the receiving signal when using Quasioptical beam analysis. In Table 11 are summarized the most relevant optical parameters that it were used in all our different simulations [70][83].

Table 11. Band 1 updated optical dimensions (Dewar = Cryostat)

PARAMETER	VALUE
Distance dewar top center to subreflector rim center	5.99380 m
Distance dewar top center to subreflector apex	5.88287 m
Dewar-top total diameter	0.97 m
Angle horn to subreflector apex	2.48 deg.
Optimal horn z-distance to dewar top	93 mm
Optimal horn x,y-distance to dewar center	263.6 mm
15 K and 110 K stage z-distance to dewar top	83 mm, 51 mm
15 K and 110 K stage clearance aperture diameter	40 mm, 60 mm
Dewar-top hole clearance diameter	110 mm
Dewar-top and ACD distance	300 mm



3.3.2 Feed Horn with or without optical arrangement

The requirements on the beam waist will determinate the size of the horn and it is feasible to be used in our Bandd1 receiver. As it was stated in section 1.1.6, the dimensions of the Band-1 receiver cartridge will determinate the maximum size of the horn that can be placed on top of the 15K Shield plate (this will also house the OMT and the HEMT-LNA). Thus, the first case that can be analyzed is when the subreflector focus its placed inside the receiver horn aperture without using any tertiary optics as a refocusing elements. This means that the standard Cassegrain antenna focus position of 5.6670 m, measured from the subreflector (Table 3), will be placed at 6.060 m. The difference between this two focus positions is of 0.393 m which means that according to Equation (71), the change of focus will require an axial subreflector displacement,

towards the Band-1 receiver, equal to approximately 1 mm. Now, using the following input parameters:

$$\left. \begin{aligned} w = w_s &= 0.3151 \text{ m} && \text{(subreflector Tapper efficiency - 12.3 dB)} \\ R = f_s &= 6.060 \text{ m} && \text{(distance subreflector - horn aperture)} \\ \lambda_{38GHz} &= 0.008 \text{ m} && \text{(center frequency wavelength)} \end{aligned} \right\} \quad (73)$$

and rearranging the beam-radius Equation (13), we get the beam-waist:

$$w_0 = \frac{w_s}{\left[1 + \left(\pi w_s^2 / \lambda f_s \right)^2 \right]^{0.5}} = 0.0478 \text{ m} \quad (74)$$

Now, to estimate the aperture size and the length of this horn, a good estimation it will be given by the optimum gain horn approach [76]:

$$\left. \begin{aligned} w &= \sqrt{2} w_0 \\ d_{\text{horn}} &= w / 0.6436 \end{aligned} \right\} \Rightarrow r_{\text{horn}} = \sqrt{2} \times 0.0468 / 0.6436 = 0.105 \text{ m} \quad (75)$$

$$\left. \begin{aligned} z_c &= \pi w_0^2 / \lambda \\ l_{\text{horn}} &= 2 z_c \end{aligned} \right\} \Rightarrow l_{\text{horn}} = 2\pi \times 0.0468^2 / 0.008 = 1.816 \text{ m} \quad (76)$$

As it was showed in the previous calculations, this is clearly a very impractical example since the horn length is much larger than the length and diameter of the Band-1 cartridge (0.47 m x 0.17 m). Thus, the use of refocusing elements is needed to minimize the size of the beam-waist at the horn aperture, which it will also minimize the horn length. For this second case, the original focus position of the Cassegrain antenna will be kept (e.g. sub-focus = 5.6670 m) and performing the same calculation as in the first case:

$$\left. \begin{aligned} w = w_s &= 0.3151 \text{ m} && \text{(subreflector Tapper efficiency - 12.3 dB)} \\ R = f_s &= 5.6670 \text{ m} && \text{(distance subreflector - rim to subreflector original focus)} \\ \lambda_{38GHz} &= 0.008 \text{ m} && \text{(center frequency wavelength)} \end{aligned} \right\} \quad (77)$$

Using the beam-waist equation:

$$w_0 = \frac{w_s}{\left[1 + \left(\pi w_s^2 / \lambda f_s\right)^2\right]^{0.5}} = 0.0447 \text{ m} \quad (78)$$

and applying this beam waist size to the thin-lens Equation (28) and (30) from section 3.2.1, with the following assumptions:

$$\left. \begin{array}{l} d_2 = d_1 = d \\ d = 0.393/2 = f \\ w_0 = w_{02} = 0.0447 \end{array} \right\} \Rightarrow w_{01} = \frac{\lambda f}{\pi w_{02}} = \frac{0.08 \times 0.1965}{\pi \times 0.0447} = 0.011 \text{ m} \quad (79)$$

The estimation of the horn aperture size and its length are given by:

$$\left. \begin{array}{l} w = \sqrt{2} w_{01} \\ d_{\text{horn}} = w/0.6436 \end{array} \right\} \Rightarrow r_{\text{horn}} = \sqrt{2} \times 0.011/0.6436 = 0.0243 \text{ m} \quad (80)$$

$$\left. \begin{array}{l} z_c = \pi w_0^2 / \lambda \\ l_{\text{horn}} = 2z_c \end{array} \right\} \Rightarrow l_{\text{horn}} = 2\pi \times 0.011^2 / 0.008 = 0.097 \text{ m} \quad (81)$$

In conclusion, the use of a thin lens with a focal length equal to 0.1965 m, placed at the same distance between the position of the Cassegrain focus and the horn aperture, it will give a horn with a length of about 0.1 m with an aperture diameter less than 0.05 m. This is a good starting point when designing our optical setup arrangement for the Band-1 receiver.

3.3.3 Four Different Optical System Design Examples

Since in the 12-meters ALMA antennas there will not be moving optical parts, except for the subreflector, the design of the all the ALMA bands optical setups must be frequency independent (i.e. the illumination at the subreflector must approximately be constant for all wavelengths) [77]. Thus the antenna efficiency will be maximized in our simulations when a 12.3 dB illumination edge taper is achieved at the subreflector at all frequencies. Once this is done, the system that does have the lowest total optical noise will be selected. Furthermore, and from its optimized result, the values of the lens focal distance, its separation from the horn, and the beam radius of the propagating beam between the lens and the subreflector will be obtained. Finally, the lens/lenses thickness can be derived using the bi-hyperbolic lens design formula (Equation (34) and (35)).

In all our models we are assuming that the center of subreflector is pointing to the center of the receiver feed. In other words this means that we are working with an on-axis focused optical system which minimized the optical aberrations discussed in section 3.2.3. To achieve consistent Quasioptical simulation results, the assumed horn beam waist and its location were taken from reference [83]. Those values are presented in Table 12.

Table 12. Beam waist size and location inside the horn that were assumed for the simulations.

Parameter:	Frequency [GHz]		
	31	38	45
Horn waist (mm)	9.49	9.43	9.35
Horn phase center (mm)	4.95	7.20	9.94

The details of the studied optical configuration layouts are the following:

A) Optical layout 1: In this configuration a single HDPE lens at 300 K was used. The lens optimal simulation result gave us a diameter was of 20 cm and the total thickness was 5.72 cm. The single lens used here acts also as a vacuum window.

B) Optical layout 2: Two HDPE lens system. A small one placed inside the cryostat 15 K stage and the second one locate between the top of the Dewar and the ALMA calibrator device at 300 K.

C) Optical layout 3: As in the first optical layout, this system also uses a single lens at 300 K but now we assume that this is made of quartz instead. A quartz vacuum window is also used at the top of the Dewar.

D) Optical layout 3: Here, the quartz lens used in the previous layout was replaced with a silicon lens design. It also has a quartz vacuum window at 300 K.

3.3.3.1 Beam Ray-tracing, HDPE Lens System

The dielectric-material properties used in this optical arrangement and their optimized input parameters, such as dimension, focal-length, and distances with respect to the horn location, are summarized in Table 13. Figure 40 shows the final quasi-optical beam propagation, while in Table 14, the estimated gain a noise performance of this simulated optical system is presented.

Table 13. Optical layout 1, simulation input Parameters.

Parameter:	Value:
Lens Material	HDPE
Refraction index n	1.5259
Loss tangent γ	2.7267e-004
Focal length f	0.1740 m
Total lens thickness	0.0581 m
Lens radius	0.100 m
Distance horn-lens	0.1790 m
Distance horn-subreflector-top	5.9965 m
Distance horn-15K_dewar_shield_Top	0.0100 m
Subreflector illumination Tapper:	31GHz = -12.3190 dB 38GHz = -12.3317 dB 45GHz = -12.3576 dB

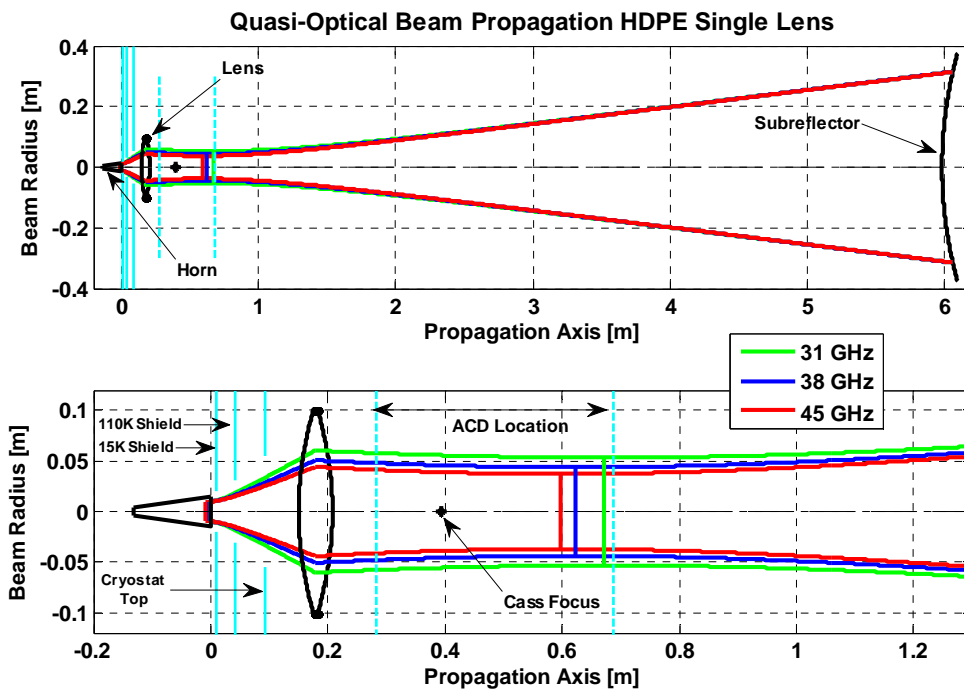


Figure 40. Resulting horn-subreflector Gaussian beam propagation through a HDPE Lens and IR-Filters.

Table 14. Total gain and noise contribution of one HDPE Lens and IR-Filters

Component Description:	Component Gain [dB]			Cumulative Gain [dB]			Component Noise [K]			Cumulative Noise [K]		
	31GHz	38GHz	45GHz	31GHz	38GHz	45GHz	31GHz	38GHz	45GHz	31GHz	38GHz	45GHz
Lens (Dielect. Loss)	0.984	0.981	0.978	0.984	0.981	0.977	4.681	5.729	6.797	4.681	5.729	6.797
Lens (Reflect. Loss)	0.990	0.990	0.990	0.975	0.971	0.968	2.050	2.050	2.050	6.763	7.819	8.894
Lens (Truncat. Loss)	0.996	0.999	1.000	0.971	0.971	0.968	0.833	0.081	0.006	7.618	7.902	8.900
CryoTop Aper. (Trunc.)	0.996	0.999	0.999	0.967	0.970	0.968	0.819	0.108	0.014	8.461	8.014	8.915
110K-filter (Diel. Loss)	0.998	0.997	0.996	0.964	0.967	0.964	0.274	0.335	0.397	8.745	8.359	9.326
110K-filter (Refl. Loss)	0.997	0.997	0.997	0.961	0.964	0.961	0.498	0.498	0.498	9.262	8.874	9.842
110K-filter (Trun. Loss)	0.997	0.999	0.999	0.958	0.964	0.961	0.481	0.126	0.042	9.763	9.005	9.886
15K-filter (Diel. Loss)	0.999	0.999	0.999	0.958	0.963	0.960	0.007	0.009	0.010	9.770	9.014	9.897
15K-filter (Refl. Loss)	0.997	0.997	0.997	0.955	0.960	0.957	0.198	0.198	0.198	9.976	9.219	10.103
15K-filter (Trun. Loss)	0.999	0.999	0.999	0.954	0.959	0.957	0.055	0.043	0.037	10.034	9.264	10.142

3.3.3.2 Beam Ray-tracing, HDPE Gaussian Telescope System

The dielectric-material properties used in this optical arrangement and their optimized input parameters, such as dimensions, focal-lengths, and distances with respect to the horn location, are summarized in Table 15. Figure 41 shows the final quasi-optical beam propagation, while in Table 16, the estimated gain a noise performance of this simulated optical system is presented.

Table 15. Optical layout 2, simulation input Parameters.

Parameter:	Value:
Lens Material	HDPE
Refraction index n	1.5259
Loss tangent γ	2.7267e-004
Focal length Lens1, f1	0.0382 m
Focal length Lens2, f2	0.1778 m
Total Lens1 thickness	0.0373 m
Total Lens2 thickness	0.0577 m
Lens1 radius	0.0382 m
Lens2 radius	0.100 m
Distance horn-lens1	0.0682 m
Distance horn-lens2	0.2618 m
Distance horn-subreflector-top	6.0615 m
Distance horn-15K_dewar_shield_Top	0.08 m
Subreflector illumination Tapper:	31GHz = -12.1791 38GHz = -12.3584 45GHz = -12.4855

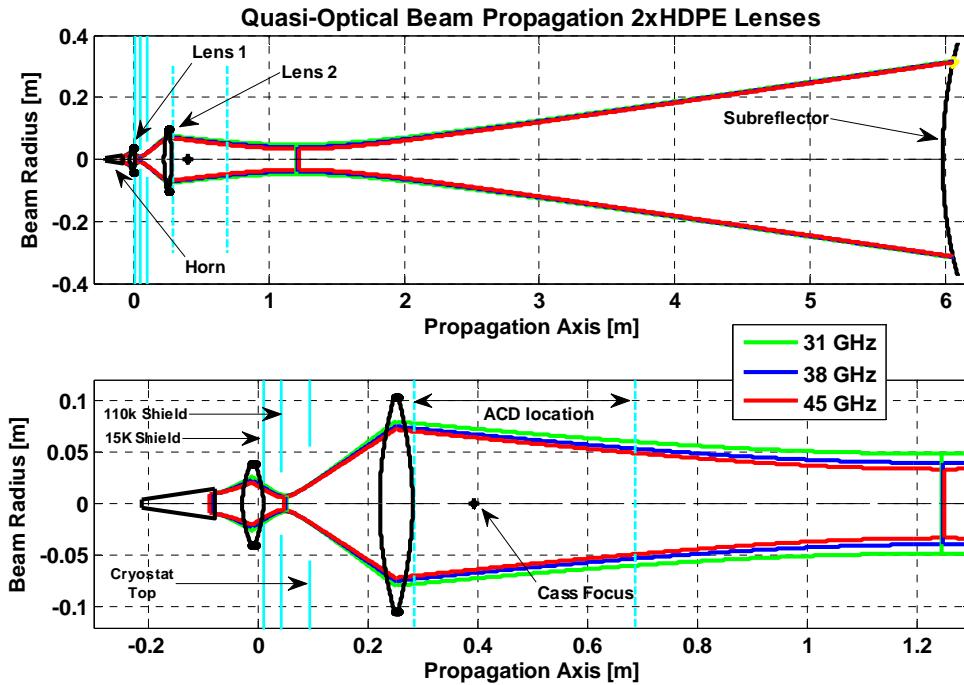


Figure 41. Resulting horn-subreflector Gaussian beam propagation through a couple of HDPE Lenses and IR-Filters.

Table 16. Total gain and noise contribution of two HDPE Lenses and Filters

Component Description:	Component Gain [dB]			Cumulative Gain [dB]			Component Noise [K]			Cumulative Noise [K]		
	31GHz	38GHz	45GHz	31GHz	38GHz	45GHz	31GHz	38GHz	45GHz	31GHz	38GHz	45GHz
Lens2 (Dielect. Loss)	0.985	0.981	0.978	0.985	0.981	0.978	4.729	5.788	6.866	4.729	5.788	6.866
Lens2 (Reflect. Loss)	0.990	0.990	0.990	0.975	0.971	0.969	2.050	2.050	2.050	6.811	7.877	8.963
Lens2 (Truncat. Loss)	0.966	0.977	0.983	0.942	0.949	0.951	6.979	4.632	3.491	13.972	12.646	12.569
CryoTop Aper. (Trunc.)	1.000	1.000	1.000	0.942	0.949	0.951	0.000	0.000	0.000	13.972	12.646	12.569
110K-filter (Diell. Loss)	0.998	0.997	0.996	0.939	0.946	0.948	0.274	0.335	0.397	14.264	12.999	12.987
110K-filter (Refl. Loss)	0.997	0.997	0.997	0.936	0.943	0.945	0.498	0.498	0.498	14.794	13.525	13.513
110K-filter (Trun. Loss)	1.000	1.000	1.000	0.936	0.943	0.945	0.000	0.000	0.000	14.794	13.525	13.513
15K-filter (Diell. Loss)	0.999	0.999	0.999	0.936	0.943	0.944	0.007	0.009	0.010	14.801	13.534	13.523
15K-filter (Refl. Loss)	0.997	0.997	0.997	0.933	0.939	0.941	0.198	0.198	0.198	15.013	13.744	13.733
15K-filter (Trun.Loss)	0.922	0.972	0.990	0.860	0.913	0.932	4.847	1.778	0.628	20.209	15.636	14.399
Lens1 (Dielect. Loss)	0.989	0.988	0.986	0.852	0.902	0.918	0.152	0.187	0.221	20.386	15.840	14.637
Lens1 (Reflect. Loss)	0.990	0.990	0.990	0.843	0.893	0.909	0.150	0.150	0.150	20.563	16.006	14.800
Lens1 (Truncat. Loss)	0.966	0.977	0.983	0.815	0.873	0.894	0.511	0.339	0.255	21.168	16.386	15.081

3.3.3.3 Beam ray-tracing, Quartz Lens and Quartz Vacuum Window System

The dielectric-material properties used in this optical arrangement and their optimized input parameters, such as dimensions, focal-lengths, and distances with respect to the horn location, are summarized in Table 17. Figure 42 shows the final quasi-optical beam propagation, while in Table 18, the estimated gain a noise performance of this simulated optical system is presented.

Table 17. Optical layout 3, simulation input Parameters.

Parameter:	Value:
Lens and vacuum Window Material	Quartz
Refraction index n	2.1056
Loss tangent γ	4.5500e-004
Focal length f	0.1740 m
Total lens thickness	0.0326 m
Lens radius	0.1000 m
Vacuum Window diameter	0.110 m
Vacuum Window Thickness	6.5 mm
Distance horn-lens	0.1790 m
Distance horn-subreflector-top	5.9815 m
Distance horn-15K_dewar_shield_Top	0.0100 m
Subreflector illumination Tapper:	31GHz = -12.3190 38GHz = -12.3317 45GHz = -12.3576

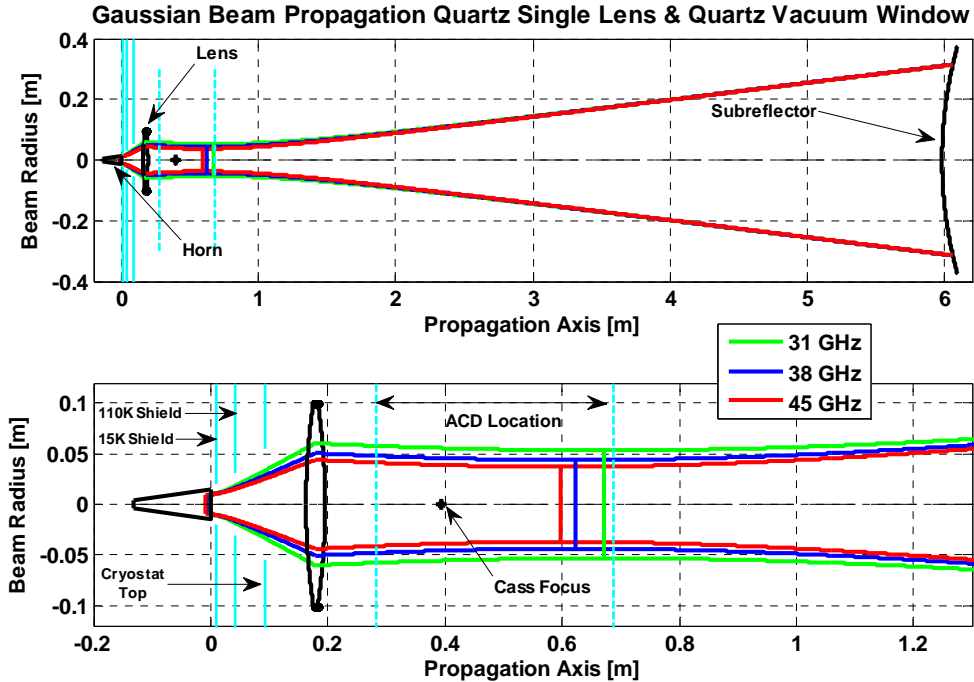


Figure 42. Resulting horn-subreflector Gaussian beam propagation through one Quartz Lens, one quartz vacuum window, and a couple of IR-Filters.

Table 18. Total gain and noise contribution of one Quartz Lens, a Vacuum Quartz Window, and Filters.

Component Description:	Component Gain [dB]			Cumulative Gain [dB]			Component Noise [K]			Cumulative Noise [K]		
	31GHz	38GHz	45GHz	31GHz	38GHz	45GHz	31GHz	38GHz	45GHz	31GHz	38GHz	45GHz
Lens (Dielect. Loss)	0.998	0.998	0.997	0.998	0.998	0.997	0.601	0.735	0.871	0.601	0.735	0.871
Lens (Reflect. Loss)	0.990	0.990	0.990	0.988	0.988	0.987	3.000	3.000	3.000	3.608	3.743	3.880
Lens (Truncat. Loss)	0.996	0.999	1.000	0.984	0.987	0.987	1.219	0.118	0.009	4.841	3.862	3.889
Vacuum Win. (Diel. Loss)	1.000	1.000	1.000	0.984	0.987	0.987	0.000	0.000	0.000	4.841	3.862	3.889
Vacuum Win. (Refl. Loss)	0.997	0.997	0.997	0.981	0.984	0.984	0.648	0.648	0.648	5.499	4.519	4.546
Vacuum Win. (Trun. Loss)	0.996	0.999	0.999	0.977	0.984	0.984	0.819	0.108	0.014	6.335	4.629	4.560
110K-filter (Diel. Loss)	0.998	0.997	0.996	0.975	0.981	0.980	0.274	0.335	0.397	6.616	4.970	4.964
110K-filter (Refl. Loss)	0.997	0.997	0.997	0.971	0.977	0.977	0.498	0.498	0.498	7.127	5.478	5.472
110K-filter (Trun. Loss)	0.997	0.999	0.999	0.969	0.977	0.977	0.481	0.126	0.042	7.622	5.607	5.515
15K-filter (Diel. Loss)	0.999	0.999	0.999	0.968	0.976	0.976	0.007	0.009	0.010	7.630	5.615	5.526
15K-filter (Refl. Loss)	0.997	0.997	0.997	0.965	0.973	0.973	0.198	0.198	0.198	7.834	5.818	5.728
15K-filter (Trun. Loss)	0.999	0.999	0.999	0.964	0.972	0.973	0.055	0.043	0.037	7.890	5.862	5.767

3.3.3.4 Beam Ray-tracing, Silicon Lens and Quartz Vacuum Window System

The dielectric-material properties used in this optical arrangement and their optimized input parameters, such as dimensions, focal-lengths, and distances with respect to the horn location, are summarized in Table 19. Figure 43 shows the final quasi-optical beam propagation, while in Table 20, the estimated gain a noise performance of this simulated optical system is presented.

Table 19. Optical layout 4, simulation input Parameters.

Parameter:	Value:
Lens Material	Silicon
Refraction index n	3.410
Loss tangent γ	4.0e-004
Vacuum Window Material	Quartz
Refraction index n	2.1056
Loss tangent	0.4550e-004
Focal length f	0.1740 m
Total lens thickness	0.0195 m
Lens radius	0.100 m
Vacuum Window diameter	0.11 m
Vacuum Window Thickness	6.5 mm
Distance horn-lens	0.1790 m
Distance horn-subreflector	5.9815 m
Distance horn-15K_dewar_shield_Top	0.0100 m
Subreflector illumination Tapper:	31GHz = -12.3190 38GHz = -12.3317 45GHz = -12.3576

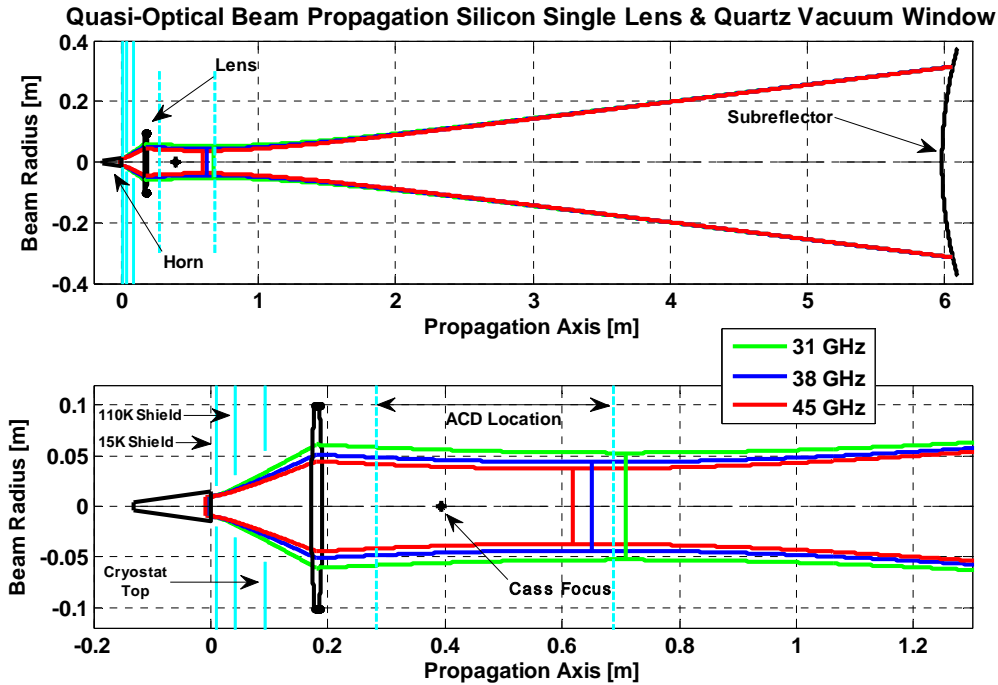


Figure 43. Resulting horn-subreflector Gaussian beam propagation through one silicon lens, one quartz vacuum window, and a couple of and IR-Filters.

Table 20. Total gain and noise contribution of one Silicon Lens, a Quartz Vacuum Window, and Filters

Component Description:	Component Gain [dB]			Cumulative Gain [dB]			Component Noise [K]			Cumulative Noise [K]		
	31GHz	38GHz	45GHz	31GHz	38GHz	45GHz	31GHz	38GHz	45GHz	31GHz	38GHz	45GHz
Lens (Dielect. Loss)	0.983	0.979	0.975	0.983	0.979	0.975	5.142	6.295	7.469	5.142	6.295	7.469
Lens (Reflect. Loss)	0.990	0.990	0.990	0.973	0.969	0.966	3.000	3.000	3.000	8.194	9.359	10.545
Lens (Truncat. Loss)	0.995	0.999	1.000	0.969	0.969	0.966	1.383	0.141	0.012	9.615	9.504	10.557
Vacuum Win. (Diel. Loss)	0.999	0.999	0.999	0.968	0.968	0.965	0.122	0.149	0.176	9.741	9.659	10.740
Vacuum Win. (Refl. Loss)	0.997	0.997	0.997	0.965	0.965	0.962	0.648	0.648	0.648	10.411	10.327	11.411
Vacuum Win. (Trun. Loss)	0.996	0.999	0.999	0.961	0.965	0.962	0.819	0.109	0.014	11.259	10.440	11.426
110K-filter (Diel. Loss)	0.998	0.997	0.996	0.959	0.962	0.958	0.274	0.335	0.397	11.544	10.787	11.840
110K-filter (Refl. Loss)	0.997	0.997	0.997	0.956	0.959	0.955	0.498	0.498	0.498	12.064	11.305	12.359
110K-filter (Trun. Loss)	0.997	0.999	0.999	0.953	0.958	0.955	0.482	0.126	0.042	12.568	11.436	12.403
15K-filter (Diel. Loss)	0.999	0.999	0.999	0.953	0.958	0.954	0.007	0.009	0.010	12.575	11.445	12.414
15K-filter (Refl. Loss)	0.997	0.997	0.997	0.949	0.955	0.951	0.198	0.198	0.198	12.783	11.652	12.621
15K-filter (Trun. Loss)	0.999	0.999	0.999	0.949	0.954	0.951	0.055	0.043	0.037	12.840	11.697	12.660

3.3.4 Discussion of Simulation Results

An important part of the simulation work that was performed in the previous section was to use different lens configurations where different dielectric materials were tested to minimize the total losses, thus minimizing also the bi-hyperbolic lens thickness. Table 21 presents the material properties used for the different investigated optical layouts. The IR-filters dimensions and properties (from Table 8) are also included in this table.

Table 21. Dielectric properties of materials used in the simulations.

Dielectric Material for:	Material	Souranding Temp. (K)	Refractive index n	Tan loss (10 ⁻⁴)
Lens:	HDPE*	300, 15	1.5259	2.73
	Quartz*	300	2.1056	0.45
	Silicon*	300	3.4165	4.00
Vac.Window:	Quartz*	300	2.1056	0.45
IR Filter:	SolidPTFE	110	1.5000	3.00
	Gore-Tex	15	1.2000	2.00

* Refractive index and tan-loss values where averaged from well know experimental measured data taken from [3] and [8].

The Quasi-optics analysis of the ALMA Band-1 system was carried out using the thin-lens approximation for the focusing elements. Further on, in this design we optimized very carefully the system total gain and its total noise contribution, taking into account the lens dimensions, its refractive index, thickness, focal distance, and as well as the IR filters dimensions, and material properties. The final simulated results for the 4 different layouts are summarized in Table 22.

Table 22. Band-1 optical parameters for the four different simulated layouts.

	Layout 1	Layout 2	Layout 3	Layout 4
Lens 1.				
Material:	HDPE	HDPE	Quartz	Silicon
Distance to horn [m]:	0.1812	0.2620	0.1812	0.1812
Focal length [m]:	0.1750	0.1778	0.1750	0.1750
Diameter [m]:	0.2000	0.2076	0.2000	0.2000
Thickness [m]:	0.0578	0.0598	0.0325	0.0194
Vacuum Window.				
Material:			Quartz	Quartz
Distance to horn [m]:	None	None	0.0930	0.0930
Diameter [m]:			0.1100	0.1100
Thickness [m]:			0.00065	0.00065
Lens2.				
Material:		HDPE		
Distance to horn [m]:	None	0.0700	None	None
Focal length [m]:		0.0382		
Diameter [m]:		0.0782		
Thickness [m]:		0.0379		
Edge Taper [dB].				
31GHz	-12.31	-12.43	-12.31	-12.31
38GHz	-12.33	-12.51	-12.33	-12.33
45GHz	-12.35	-12.58	-12.35	-12.35
	-			

After optimizing the illumination efficiency of each one of the optical system layouts, we estimated the total gain and noise contribution of each one optical layout configurations. The gain and noise contribution related to the beam truncations, dielectric losses, and reflection losses of

the lens and IR-Filters were included in the overall noise calculations. Truncation and reflection termination temperatures were taken as average of both shield sides temperatures. The reflection losses in the lenses and IR-filters were modeled assuming perfect surface matching. Therefore those losses were estimated to be of about -20 dB for the lens and -25 dB for the IR-filters. Focus efficiency of the antenna has been placed at a lower priority since it is assumed that the secondary can be refocused. Figure 44 shows the total optic noise contributions estimated for each one of the systems.

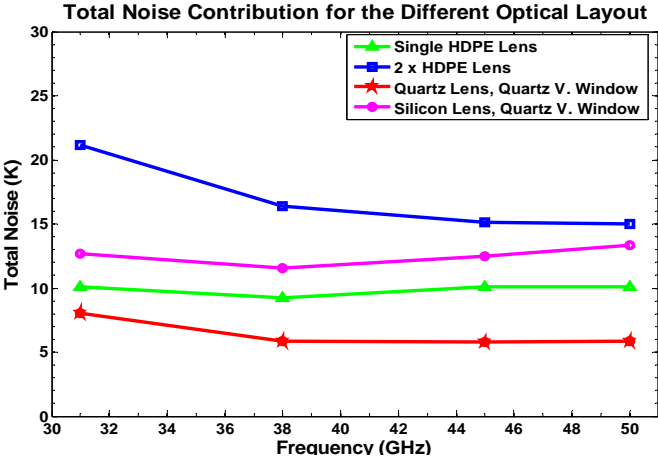


Figure 44. Total noise estimation of the 4 different studied optical layouts.

Layout 3 (quartz lens + quartz vacuum window) provides the lowest system noise contribution. This is the result of the high refractive index value and low tangent loss characteristics of the quartz, making its total thickness very small. However, from the practical and economic point of view, layout 1 (single HDPE lens design) is a more competitive system since it is easier to construct with a CNC machine.

3.4 Final Lens Design and Construction

From the results obtained in the previous section, the chosen optical system was the one using a simple HDPE lens design. The optical parameter corresponding to this optical system is summarized as Layout 1 in Table 13. Inserting those parameters in Equation (34), the lens profile thickness is obtained for one side part of the lens which is shown in Figure 45 with a red line.

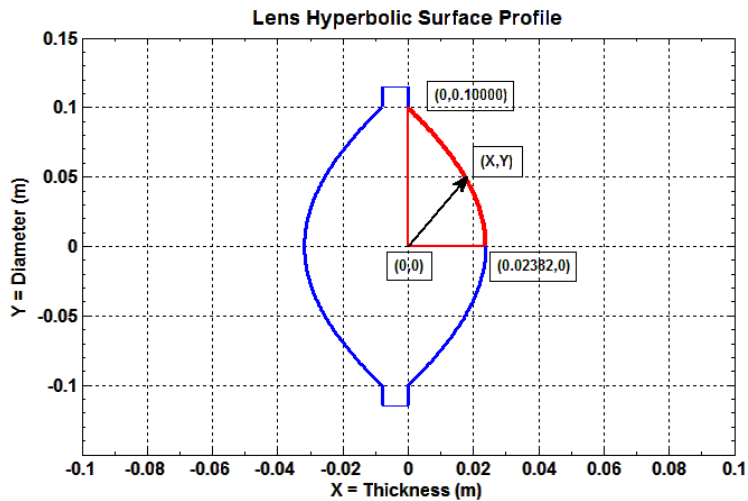


Figure 45. *The final Band-1 designed HDPE lens profile.*

The total lens design includes 2 hyperbolic faces and, in between, a 0.8 cm HDPE slab section that will work as flange section. In Figure 46, it is shown the constructed bi-hyperbolic HDPE lens that is being mounted in top of the test cryostat for the ALMA Band-1 receiver. In this cryostat configuration, the horn aperture to the lens center distance was set to 0.1812 m and the angle horn-lens was tilted 2.48 degrees to face the ALMA Cassegrain subreflector apex center. The test results of this constructed lens will be performed and summarized in the next chapter, once the best horn design is being chosen and constructed. The CAD detail of the final and constructed lens design is presented in appendix section 7.1.



Figure 46. *The constructed HDPE lens mounted in top of the test cryostat for the ALMA Band1 prototype receiver.*

3.5 Lens Antireflection Layer

To reduce the losses of power due to reflections at the lens surface and standing waves that are generated inside the lens, an antireflection layer surface can be cut in the form of concentric machined grooves on the lens surface. This lens surface treatment helps to minimize the reflections since it create an intermediate impedance discontinuity between the air and the lens material.

According to [84] for a single matching layer between the air and the lens, the optimum thickness of such antireflection layer can be estimated using the following expression:

$$d_{opt} = \frac{\lambda}{4\sqrt{n}} \quad (82)$$

where:

n = the refraction index of the lens material.

λ = the central frequency wavelength

Now, depending on the groove width and the distance between two consecutive straight grooves (width a depth equal to d_{opt}), an incoming plane wave which is perpendicular polarized and is that hitting the matching layer surface with a perpendicular incident angle (see Figure 47), it will “sense” that the refractive index n of the layer in can be expressed in two main cases.

First, if the E-field is perpendicular to the groove direction,

$$n_p^2 = \alpha + (1 - \alpha)n^2 \quad (83)$$

Second, if the E-field is in parallel to the groove direction,

$$n_n^2 = \frac{n^2}{1 - \alpha + \alpha n^2} \quad (84)$$

where:

n = the refraction index of the lens material.

α = the groove width to pitch ratio (see Figure 47)

The α constant is given by:

$$\alpha = \frac{a}{p} \quad (85)$$

where p is the pitch constant.

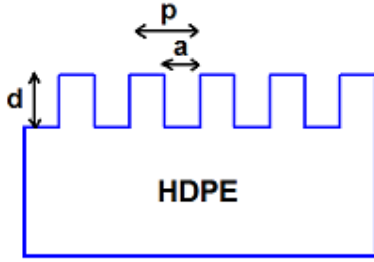


Figure 47. Straight matching layer cross-section geometry. d is the optimum antireflection layer thickness, a is its groove width, and p in its corresponding pitch constant.

For example, if the lens is constructed using HDPE with a refractive index $n=1.5259$ (which is the refractive index of the dielectric material used in the simulations in section 3.3.2) the optimal groove depth d_{opt} will be 1.6 mm when the lens is designed at around the center frequency of 38 GHz. Equation (83) and (84) can be plotted in a same graph as a function of α (see Equation (85)), and by extrapolating where these two curves intersect the line represented with $n = 1.5259$, then the value of each different refractive index can be obtained. In Figure 48, this extrapolation process is illustrated. The optimum groove to pitch ratio for a perpendicular incident E-field is 0.4, while for the parallel E-field, the α -constant is equal to 0.6.

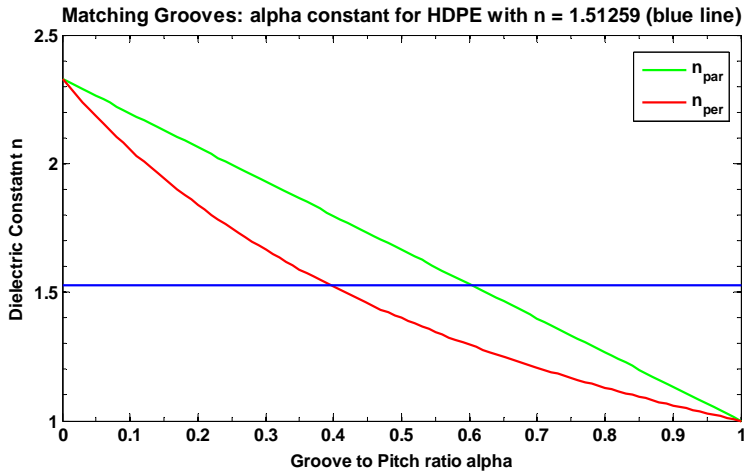


Figure 48. Matching grooves dielectric properties for parallel and perpendicular incident E-field.

To confirm that the obtained matching groove parameters are suitable when designing the antireflection layer of our HDPE lens device, the lens reflection losses were modeled using Ansoft HFSS [85] (see chapter 4 for a proper description of HFSS). The model used consists of a piece of HDPE of length 5.81 cm inside a WR-22 square waveguide. Then, by varying the corrugation profile at both sides of the lens surface (see Figure 49), the simulated reflection losses S_{11} of the HDPE lens were obtained. The results are shown in Figure 50, where a constant pitch of 1 and 3 different grooves widths were used.

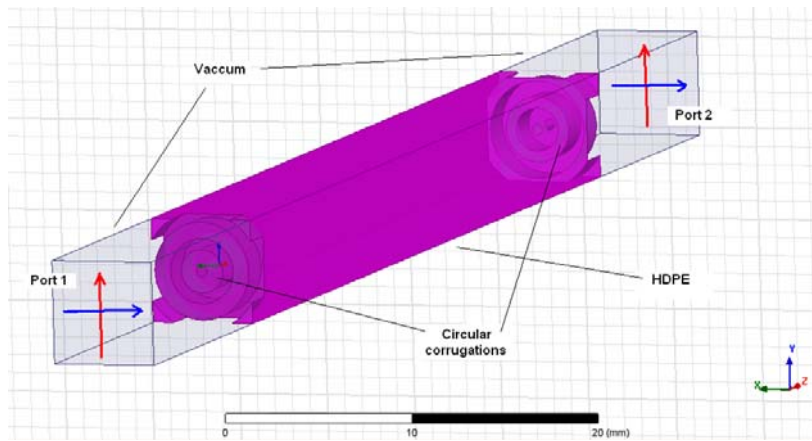


Figure 49. Circular surface matching grooves geometry used during the HFSS simulation for our 30 to 46 GHz HDPE lens design. The blue and red arrows denoted the orientation of the vertical and horizontal E-field excitations inside the square waveguide. Port 1 is the input of the simulated E-field while the port 2 is its output.

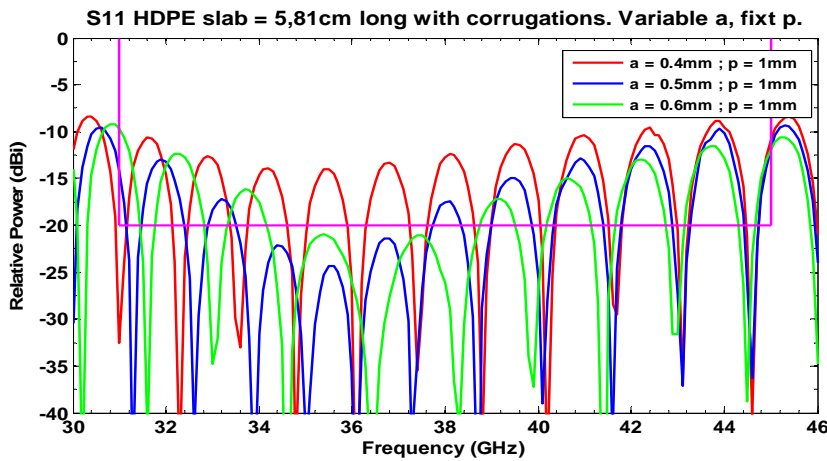


Figure 50. Circular surface Matching grooves simulations for our HDPE designed lens between 30 to 46 GHz. The different results correspond to matching groove-widths of 0.4, 0.5, and 0.6 mm, and constant pitch ratio equal to 1. The vertical magenta line close in the working bandwidth of the optical system, while the horizontal line shows the -20dB reflection boundary region that correspond to 1 % of losses.

When looking at the results shown in Figure 50, it can be confirmed that the best reflection losses correspond to a groove width of 6 mm and a tooth width of 4 mm. With these values, it will correspond to machine 100 grooves on the lens surface. This is a large number of corrugations that could be difficult to achieve because of two reasons. First, the milling tool needs to have a diameter of 0.6 mm and, second, because the size of the tooth distance in between consecutive grooves. The later means that the tooth may not be accurately constructed if the CNC late does not have a great accuracy and also due to the fact that the dielectric material as the HDPE, are hard to work with (difficult to remove the plastic chips from the machined grooves). Therefore, by increasing this time both, the pitch ratio size and the groove size, but keeping the α -ratio constant between these two parameters, the groove and tooth sizes were increased by a factor of 2 each (resulting in a number of 50 grooves instead of 100) while

keeping the reflection performance as in the previous case. These results are summarized in Figure 51.

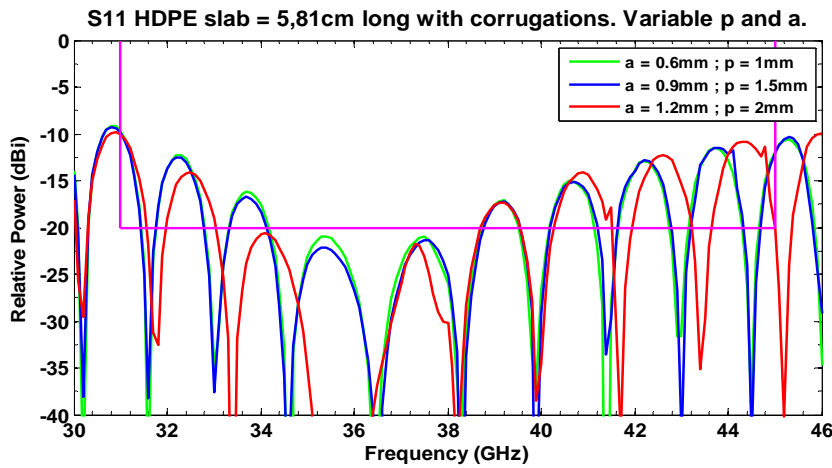


Figure 51. Circular surface Matching grooves simulations for our HDPE designed lens between 30 to 46 GHz. The different results presented here correspond to matching groove-widths and pitch of different sizes and ratios.

It is important to mention that the HFSS-simulated reflections obtained in this section, are not so accurate since the used model simulates a piece of a HDPE inserted in a WR-22 waveguide and not using a more realistic model that uses the whole lens profile embedded in air box which, for example, is excited by a plane-wave. The main problem of using the second more complex model is that it will need both, a powerful computer (e.g. a cluster) and a large amount of RAM memory that can take care of a large number of calculations that will be required for this setup. On the other hand, when using our “simple” model, though not accurate enough when estimating the reflection loss parameter S_{11} , it will help us to find the best optimized parameters to minimize the reflection losses at the center of the working bandwidth. According to [83], the reflection losses for our matching layer design at the band edges should be around -20 dB (about 1% of losses), while according to the HFSS simulation results using the simplified waveguide model, the worst case was at the band edges where the reflection losses were of around -12 dB (or 6% of losses).

Now, if the quartz lens arrangement (Layout 3, in Table 23) is going to be used in our optical system, a proper antireflection thin layer made of a dielectric material should be used on both sides of the lens surface [86]. Thus, the coating layer thickness can also be determined by using Equation (82). For example, by using a dielectric material such as PTFE with a refractive index n equal to 1.43 [35], around the center frequency of 38 GHz (i.e. λ equals to 7.895 mm), then Equation (82) gives an approximately PTFE layer thickness of 1.65 mm.

3.6 Conclusions

Quasioptical theory using first order Gaussian beam propagation, and thin lens approximation were used in all the 4 optical system simulations. The quartz lens optical design (layout 3) gave the best noise performance of all the 4 different optical layouts presented in section 3.3.2. However, the single HDPE lens design, originally proposed by ALMA (layout 1), continues to provide a good noise performance given the layout constraints of the cryostat. Moreover, the main advantage of choosing the HDPE lens is that it is easier and less expensive to construct using a CNC lathe machine than using a lens made of quartz.

The lens system corresponding to layout 1 was constructed (without an antireflection matching layer treatment) and its performance will be tested and qualified in the next chapter 4. After analyzing those results, and correcting possible values of lens focus and its location between the horn-subreflector system, which maximize the antenna efficiency, a second corrected HDPE lens needs to be constructed. The results will also demonstrate the importance of the antireflection matching pattern. The designed parameters of such antireflection “coating” that minimize the reflection losses are discussed in section 3.5.

Chapter 4

Horn Design and Construction

This chapter is intended to describe the details of the design, optimization, construction and testing of the 31.3-to- 45 GHz corrugated horn that will be used as a feeder in our optical system. It is important to mention that there is a previous ALMA Band-1 horn model designed by M. Carter [87], that was also constructed and measured [88]. Those results will be used for comparison reasons in this work. Here, we propose to design a similar Horn design that keeps the same performance, but with a more compact size. In this way, it will be easily accommodated on top of the cryo-cooled thermal plate together with the other microwave components that belong to the 15-K stage.

In summary, two designs were studied, a classical conical corrugated horn, and a spline-line corrugated horn. Once both horns were optimized, using different electromagnetic designing tools for each one of them, those were compared in terms of return loss, side-lobe level, and co and cross polar radiation patterns. The simulation results showed that both horns have almost similar performances as Carter's horn. However, the spline-horn the chosen one to be constructed and tested experimentally due to its short length, which it was less than half of the size of the conical corrugated horn.

4.1 Introduction

Circular symmetrical corrugated horns produce radiation patterns with high beam symmetry, high beam efficiency, low cross-polarization levels, very low side lobe levels, and provide wide-bandwidth performances. The generation of the high beam symmetry is due to the fact that this kind of horn supports the propagation of the so called *hybrid-modes* within the horn structure, which makes them the best choice of feeder to be used in reflectors antennas [44]. Basically, the hybrid-modes are a combination of TE and TM modes that propagate with a common velocity. For example, the fundamental mode HE_{11} , which is a hybrid-mode that matches the TE_{11} fundamental mode of the horn circular input waveguide section with the fundamental TEM_{00} mode that propagates from the horn corrugated thread section into the free space. The HE_{11} mode is accomplished by an appropriate variation of the slots depths of the horn *mode launching* section (see Figure 15 on page 31), which then matches the impedances of the circular waveguide and thread section parts of the horn [89].

To design the horn, we have determinate a set of goals that are summarized in Table 23 [71].

Table 23. ALMA Band-1 horn specifications expected at all frequencies.

Parameter:	Specification:
Reflections:	< - 20 dB
Cross polarization:	< - 30 dB
Side lobe levels:	< - 25 dB
Bandwidth	= 31-45 GHz
Total antenna efficiency ⁽¹⁾	> 80 %

⁽¹⁾ Of the horn+lens system when illuminating the subreflector.

4.2 Classical Corrugated Conical Horn

The theory presented here is based in [90][91], as they summarize the most important topics of the design and construction of high-performance symmetrical corrugated horns. Other references will be indicated in the corresponding paragraphs.

4.2.1 Theory and Design of a Preliminary Horn

First, the design of the corrugated horn starts by defining four different quantities of frequency, which are used later on within the horn designing parameters. Those quantities are the following.

f_{min} = lowest operating frequency = 31 GHz

f_{max} = highest operating frequency = 45 GHz

f_c = center frequency .

f_o = output frequency.

When designing a wide-band corrugated horn, which is the case for the ALMA Band-1 horn, the following bandwidth condition must be met:

$$1.4 \times f_{min} \leq f_{max} \leq 2.4 \times f_{min} \Leftrightarrow 43.4 \text{ GHz} \leq 45 \text{ GHz} \leq 74.4 \text{ GHz} \quad (86)$$

Since the condition was met, then the center frequency is given by:

$$f_c = 1.2 \times f_{min} = 37.2 \text{ GHz} \quad (87)$$

and the output frequency can be set equal to:

$$1.05 \times f_c \leq f_o \leq 1.25 \times f_c \Leftrightarrow 39.06 \text{ GHz} \leq f_o \leq 74.4 \text{ GHz} \Rightarrow f_o = 40.92 \text{ GHz} \quad (86)$$

Secondly, there are several parameters related to the shape and dimensions of the horn that need to be estimated. Figure 52 shows the geometry of a linear corrugated horn profile that shows the main designed parameters to be considered when designing this kind of horn. The symbols used for those parameters are summarized in Table 24:

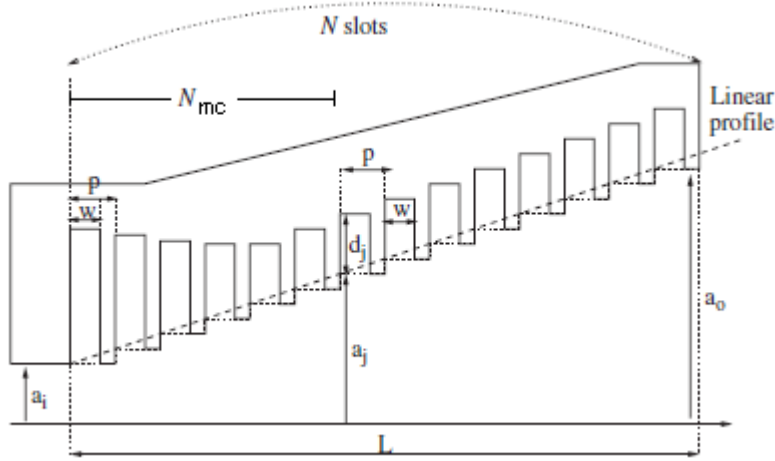


Figure 52. Conical corrugated linear horn profile geometry. Figure adapted from reference [91].

Table 24. The corrugated -orn parameters that need to be estimated (see Fig. 52).

Quantity	Symbol
input radius	a_i
output radius	a_o
horn length	L
horn flare-angle	α
total number of slots	N
corrugation pitch	$p = L/N$
width of the slot teeth	w_j
corrugation pitch-to-width ratio	$\delta = w_j/p$
mode converter type	<i>variable-dept-slot</i> , or <i>variable-pitch-to-width-slot</i>
depths of the slots of the thread section	d_j
depths of the slots of the mode converter	d_{jmc}
number of slots in the mode converter	N_{mc}
corrugated-surface profile	<i>Linear, Sinusoid, Gaussian, etc</i>

The *input radius* of the horn circular waveguide is given by the fundamental mode TE_{11} cut-off frequency, but this is a modified version that uses the central wavelength to assure that the waveguide size cut-off the fundamental mode at a lower frequency than the f_{min} which is equal to 31 GHz. This equation is then given by:

$$a_i = \frac{3 \times \lambda_c}{2\pi} = \frac{3 \times 8.06 \cdot 10^{-3}}{2\pi} \approx 3.85 \text{ mm} \quad (87)$$

The horn *output radius* it designed to have a certain illumination taper on the Cassegrain subreflector. However, as it was stated before, in page 62 (Equations (73) trough (76)), if the horn aperture is directly illuminating the subreflector, the horn size will be have a length of 1.816 m and an aperture radius of 0.105 m, a dimension that is not feasible to be installed in the receiver cartridge. Therefore, a lens placed in between the horn and the subreflector is need it to refocus the beam. The preliminary calculations were performed in page 63 (Equations (77) trough (81)), where the lens, with a radius of 0.1 m, was placed at a distance from the horn that equals the lens focal point or 0.1965 m. Using this fact, the horn output radius can be determined with the help of the horn design curves summarized in [92], and the geometry shown in Figure 53.

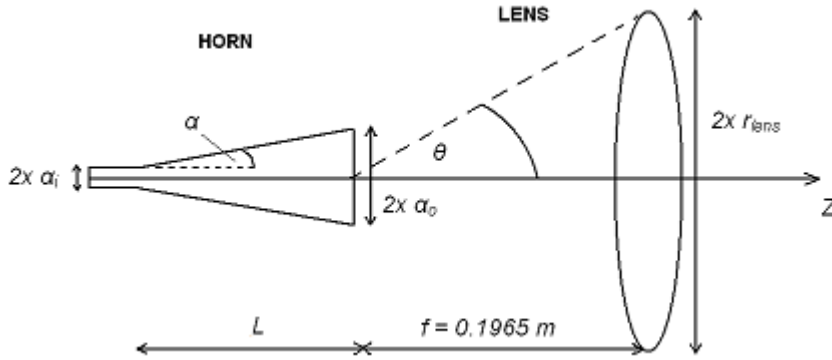


Figure 53. Geometry of the horn location with respect to refocusing lens. The angle θ is the illumination angle of the horn, while α is the horn flare angle.

When estimating the illumination angle of the horn over the lens surface, the following calculation was made:

$$\theta = \tan^{-1}\left(\frac{r_{lens}}{f}\right) = \tan^{-1}\left(\frac{0.1}{0.1965}\right) \approx 27^\circ \quad (88)$$

Using this illumination angle of 27° and requiring, for example, that the truncation losses of the horn radiation over the lens surface will of -20 dB (i.e. 1% of losses), then the extrapolated directivity is obtained from the design curve shown in Figure 2 of the reference [92], giving about 21 dB. Taken this directivity value on designing curve shown on Figure 3 (same reference), it will return the following ratio from which the horn output radius a_o can finally be extracted:

$$D/\lambda_c = 3.4 \Rightarrow a_o = \frac{3.4 \times 8.06 \times 10^{-3}}{2} \approx 14.0 \text{ mm} \quad (89)$$

From the extracted values in equation (88) and (89) in the same Figure 3 (reference [92]), the *horn flare angle* can be extracted and it will be equal to:

$$\alpha \approx 5^\circ \quad (90)$$

The *horn length* L will be then given by (see the geometry in Figure 53):

$$L = \frac{(a_o - a_i)}{\tan(\alpha)} = \frac{(0.014 - 0.00385)}{\tan(5^\circ)} \approx 0.120 \text{ m} \quad (91)$$

When deciding what will be the *total number of slots* in horn corrugated section, one needs first to decide what will be a reasonable *pitch* ratio to have, which it will need to be in the range of $\lambda_c/4$ but less of $\lambda_c/2$. A good choice of p it will then be:

$$p = 3 \text{ mm} \quad (92)$$

From the above value, the *total number of slots* can be calculated from the following relationship:

$$p = \frac{L}{N} \Leftrightarrow N = \frac{L}{p} = \frac{120}{3} = 40 \quad (93)$$

The *width of the slots* sometimes is not constant over the whole horn corrugation profile. This parameter will depend, as the *depth of the slot* parameter. It also does on which *mode converter type* we are going to use for our horn design. There are two different kinds of mode converter that it will be used in this work. Namely the *variable-depth-slot*, and the *variable-pitch-to-width-slot* mode converters [93].

The *variable-dept-slot* mode converter is the easiest one to design and fabricate since its *pitch-to-width ratio* is constant for all the slots in the corrugation profile. For example, if our choice of pitch p was set to 3 mm, then in general the *width of the slot* can be chosen to be equal to half of this value:

$$w = 1.5 \text{ mm} \quad (94)$$

and its *pitch-to-width ratio* will be given by :

$$\delta = \frac{w}{p} = \frac{1.5}{3} = 2 \quad (95)$$

The *depth of the slot* can be estimated from the following equation:

$$\left\{ \begin{array}{l} d_{jmc} = \left\{ 0.45 - \frac{j-1}{N_{mc}} \left(0.45 - \frac{1}{4} A_j \right) \right\} \lambda_c \quad \text{for : } 1 \leq j \leq N_{mc} + 1 \\ d_j = \frac{\lambda_c}{4} A_j - \left(\frac{j - N_{mc} - 1}{N - N_{mc} - 1} \right) \left\{ \frac{\lambda_c}{4} B_j \right\} - \frac{\lambda_c}{4} C_j \quad \text{for : } N_{mc} + 2 \leq j \leq N \end{array} \right. \quad (96)$$

where:

$$A_j = \exp \left[\frac{1}{2.114 \times (k_c a_j)^{1.134}} \right]$$

$$B_j = \exp \left[\frac{1}{2.114 \times (k_o a_o)^{1.134}} \right]$$

$$C_j = \exp \left[\frac{1}{2.114 \times (k_o a_o)^{1.134}} \right]$$

$$k_c = \frac{2\pi}{\lambda_c} ; k_o = \frac{2\pi}{\lambda_o}$$

N_{mc} = mode converter number of corrugations which gave us the best results when = 7
 a_j = horn diameter at a certain distance inside the horn.

The second mode converter, the *variable-pitch-to-width-slot* mode converter, is a little more complex to design than the previous one. In this case we have:

$$\left\{ \begin{array}{l} d_{jmc} = \left\{ 0.45 \frac{\lambda_c}{1.15} + \frac{j-1}{N_{mc}-1} \left(\frac{\lambda_c}{4} - 0.45 \frac{\lambda_c}{4} \right) \right\} \times A_j \quad \text{for : } 1 \leq j \leq N_{mc} + 1 \\ d_j = \frac{\lambda_c}{4} A_j - \left(\frac{j - N_{mc} - 1}{N - N_{mc} - 1} \right) \left\{ \frac{\lambda_c}{4} B_j \right\} - \frac{\lambda_c}{4} C_j \quad \text{for : } N_{mc} + 2 \leq j \leq N \end{array} \right. \quad (97)$$

where:

$$N_{mc} = 12$$

Finally, the *width of the slot* of the *variable-pitch-to-width-slot* mode converter is given by:

$$w_{jmc} = 0.25 \left(1 + \frac{j-1}{N_{mc}-1} \right) \quad (98)$$

There are several choices of *corrugated surface profile* as it can be found in [93]. Probably the most commonly used profile is the *linear* one, which is the one we chose here for its simplicity when drawing such structure before simulating it.

4.2.2 Preliminary Corrugated Horn Simulation

Figure 54 shows the horn profile geometry. The horn parameters were determined in the previous section using the results from Equations (86) through (93), and also using equations (97) and (98), that determines the depth and the width of the variable-pitch-to-width-slot mode converter section of this horn. The total length of the horn became 14.0 cm from which the corrugation section has a length of 12.0 cm. The horn output throat section has a diameter of 2.8 cm while the input circular waveguide has a diameter of 0.78 cm.

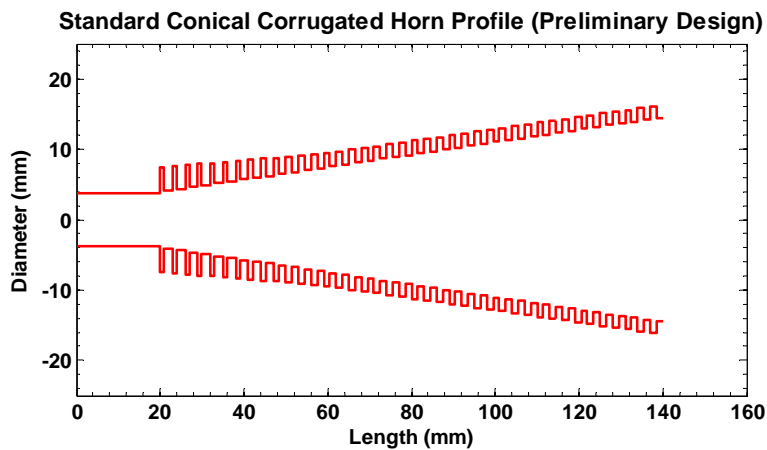


Figure 54. The resulting profile geometry of the preliminary horn design. Its corrugation section length is 12.0 cm, the output throat has a diameter of 2.8 cm, and the flare angle is of about 4.85° . The circular waveguide has a diameter of 0.77 cm. A variable-pitch-to-width-slot mode converter was used in this design.

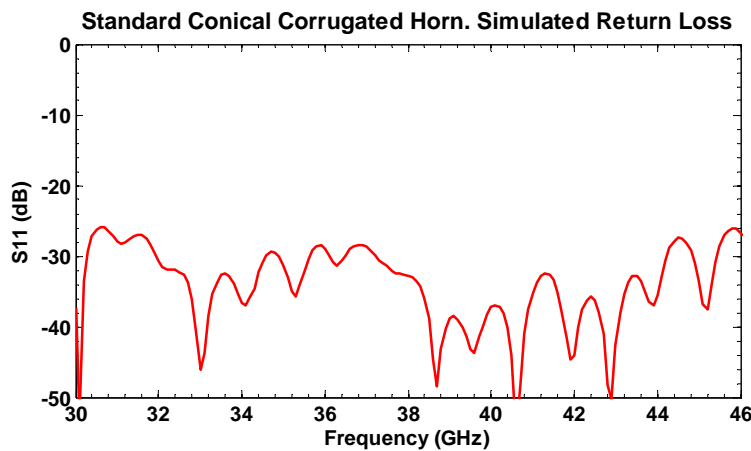


Figure 55. HFSS simulated reflection results of the preliminary horn design. Observe that the reflection losses comply the -20 dB for entire bandwidth according to the ALMA Band-1 specifications.

In Figure 56 the HFSS-simulated radiation pattern performances for this horn are shown at 31, 38, and 45 GHz. Figure 55 shows their respective simulated return losses from 30 GHz up to 46 GHz. By analyzing these results, it can be determined that our preliminary horn design does comply with the reflection-loss specifications stated in Table 23. On the other hand, it does not fulfill with the cross polar specifications, which peaks are higher than -30 dB at 31 or 45 GHz, and neither with E-field and H-field beam symmetry at 31 GHz, that a well designed corrugated conical horn should have when illuminating a Cassegrain antenna [95]. Thus, this preliminary horn design needs to be optimized to find the right feeder that it does comply with all the specifications.

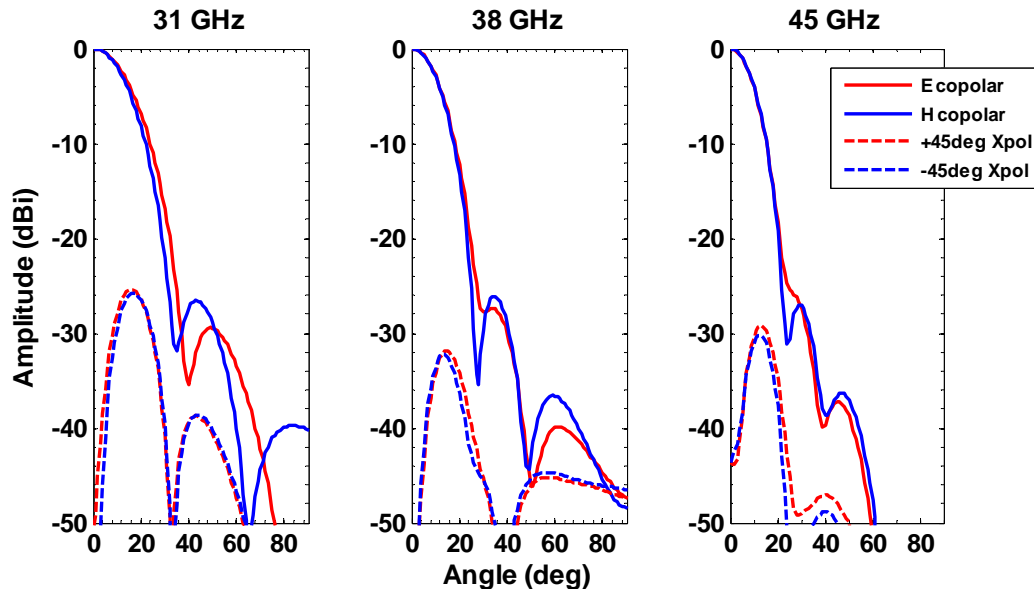


Figure 56. Simulation results of the co-polar and cross-polar radiation patterns at 31, 38, and 45 GHz of the preliminary horn design, which geometry is shown in Figure 54. Note how the E-field shows a wider Gaussian profile than the corresponding H-field at 31 GHz. At the same frequency, the cross-polar levels are much higher than the required -30 dB.

4.2.3 Optimizing the Preliminary Corrugated Horn Design

As it was stated in the previous section, our corrugated conical horn needs to be optimized to comply with the required specifications. Therefore, several changes were made in the length, input and output apertures size, and mode launching horn section. After simulating and optimizing with several designs with the help of HFSS, it was founded that a horn with similar designing characteristics as the Carter horn [87], was the one that it did come closer to fulfill the specifications. The optimization process of the simulation was achieved by first fixing the horn length, output aperture, and flare angle during the simulation while the number of corrugation slots, slot width, pitch, pitch-to-width-radio, slot depth, and mode converter type were varied (one parameter at the time).

The final length of the horn was of 13.6 cm, the throat output diameter of 3.0 cm, and the circular input waveguide diameter of 0.79 cm, which together generate a flare angle of about 4.79° . This horn was designed using a variable-depth-slot mode converter (i.e. fixed pitch with variable depth) instead of using the more complex variable-pitch-to-width-slot mode converter that is was used in the preliminary design. The final profile is shown in Figure 57.

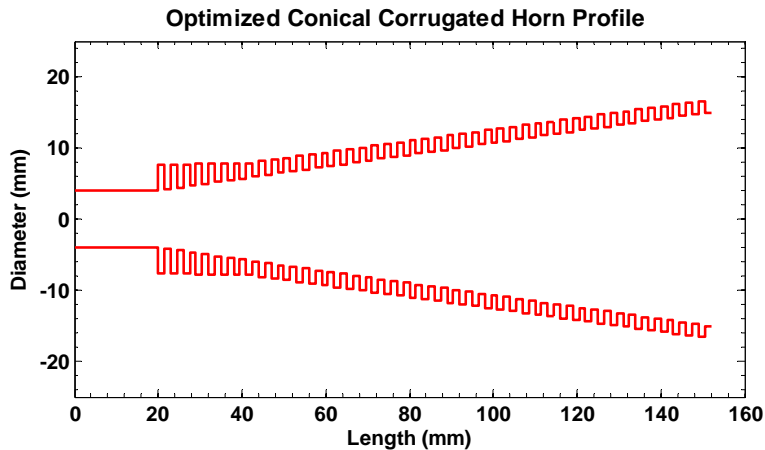


Figure 57. The final optimized corrugated conical horn profile geometry. Its corrugation section length is 13.6 cm, the output throat has a diameter of 3.0 cm, and the flare angle is of about 4.79° . The circular input waveguide has a diameter of 0.79 cm. This horn was designed using a variable-depth-slot mode converter.

The return loss of this horn design is shown in Figure 58. This result is not as good as the reflection losses obtained with the previous horn design, but it still comply with the -20 dB specification. The beam-pattern simulations are shown in Figure 59. Here it can be noted that both, the cross-polar levels and the beam symmetry at 31 GHz were improved much more improved, but still the cross polar level at this frequency is still slightly out of the specs. On the other hand, at 38 and 45 GHz, the radiation patterns fulfill the horn designing requirements.

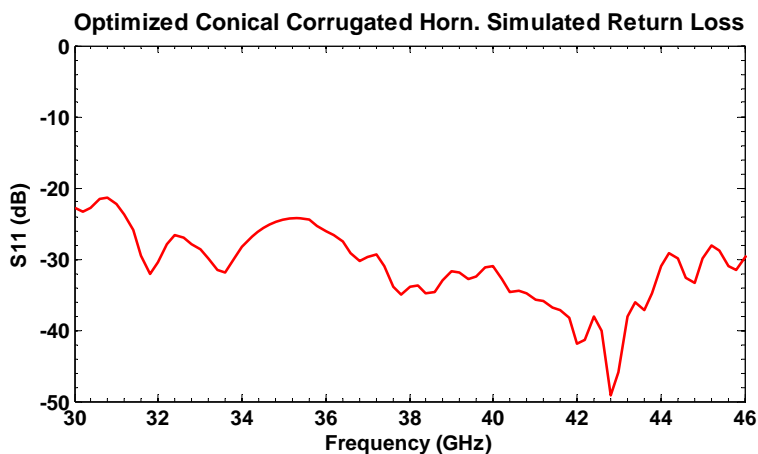


Figure 58. The HFSS-simulated return loss of the optimized corrugated conical horn

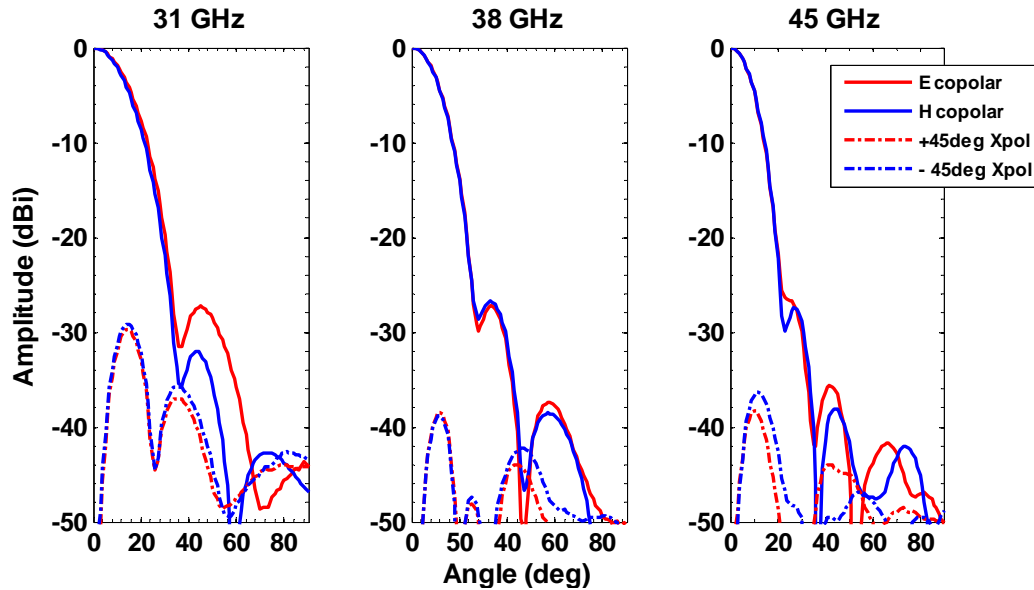


Figure 59. Co-polar and cross-polar radiation pattern simulations of the optimized corrugated horn design performed at 31, 38 and 45 GHz, which geometry is shown in Figure 57.

4.3 Corrugated Spline-line Horn Design Using Mode Matching Techniques

There is another interesting horn design alternative to be study which is the so called “Smooth-Walled Spline-Profile horn” developed by C. Granet [96]. In order to achieve the stringent specifications imposed over the horn, in particular its large coverage bandwidth, two different profiles were studied and optimized using mode-matching techniques [97]. The horn requirements are the same as those stated in Table 23. The optimization procedure description is defined step by step in [96] and [98]. The first design was based on a smooth-walled profile while the second model was a corrugated spline-profile horn.

As it was shown in [99], the spline-profile corrugated horn design was the best choice to construct since it met all the specifications in a much better way than the simple smooth walled horn. As an additional advantage, the corrugated spline-profile horn resulted in a total length which is almost less than half of the size of the conventional conical corrugated horns, e.g. those designed and simulated in the previous sections. The small resulting size of the smooth-walled corrugated horn makes it easier to be implemented in the Band-1 receiver. This is particularly important in ALMA as the available space for implementing the receiver is limited as it was discussed before.

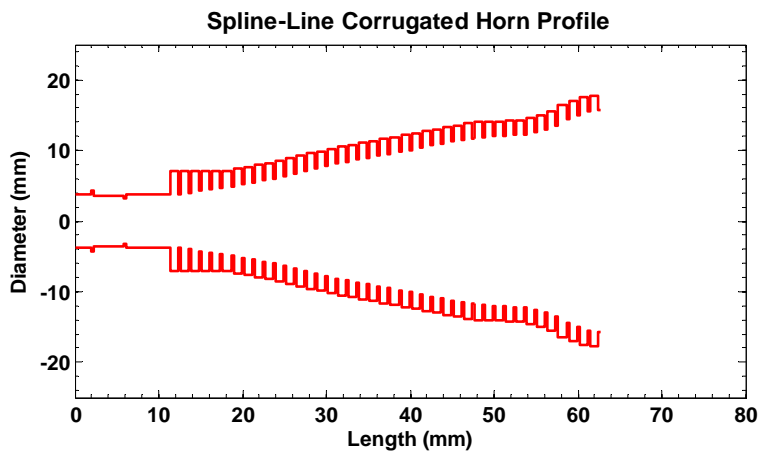


Figure 60. Profile of the spline-profile corrugated horn. The dimensions are given in Table 25.

The corrugation profile of the selected horn is shown in Figure 60 and Table 25 summarizes its physical dimensions. After the design, the horn was simulated using Ansoft HFSS electromagnetic software. The simulated horn geometry is shown in Figure 60. As in case of the two previous classical horn designs, this horn one was characterized in terms of reflection losses and co and cross polar pattern performance.

Table 25. Dimensions of the different sections of the spine-line corrugated horn.

Horn Section	Dimension (mm)
Horn total length	62.37
Circular waveguide length	11.42
Corrugated section length	51.25
Input diameter	7.62
Output diameter	31.50
Teeth width	0.94
Grove width	0.31
Grove depth	2.01–3.35

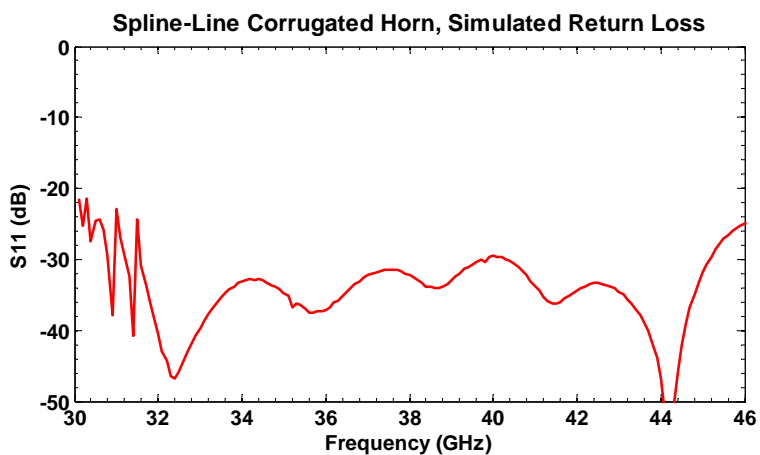


Figure 61. The corrugated spline-line horn simulated return-loss results with HFSS.

Figure 61 shows the return losses from 30 GHz up to 46 GHz. This simulation fulfill the horn reflections loss specification of <-20 dB for the entire Band. In Figure 62, the HFSS-simulated radiation pattern performances at 31.3, 38, and 45 GHz are shown. The co-polar curves look very symmetric for both, the E and the H-fields. Their corresponding cross-polar peaks and side-lobe levels do also comply with the expected specifications that were stated in Table 23. Figure 63 shows the spline-line horn geometry used to perform the HFSS simulations.

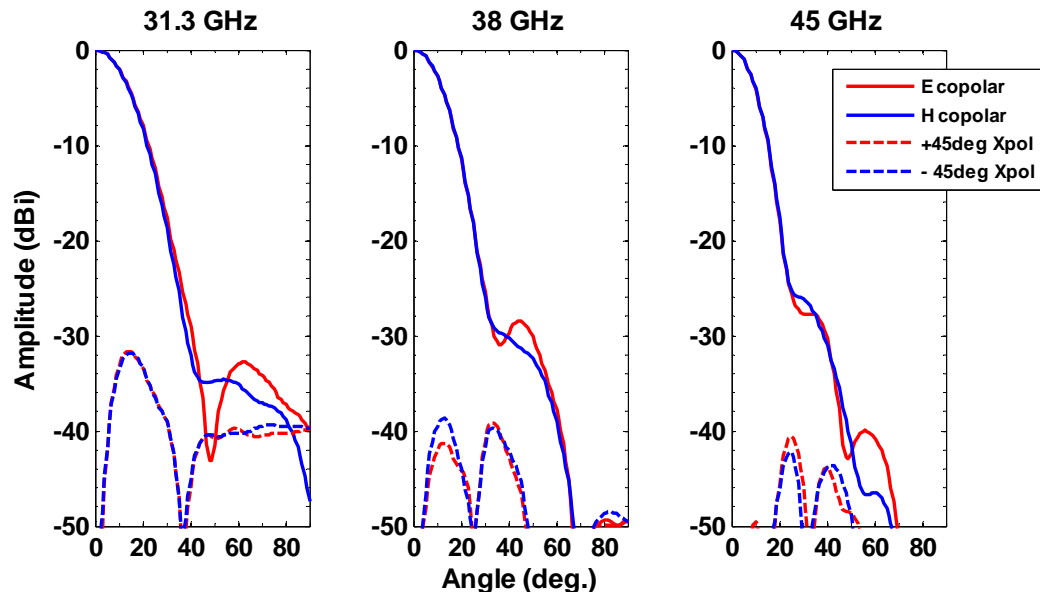


Figure 62. Resulting co-polar and cross-polar simulated beam patterns for the spline-line horn profile shown in Figure 60.

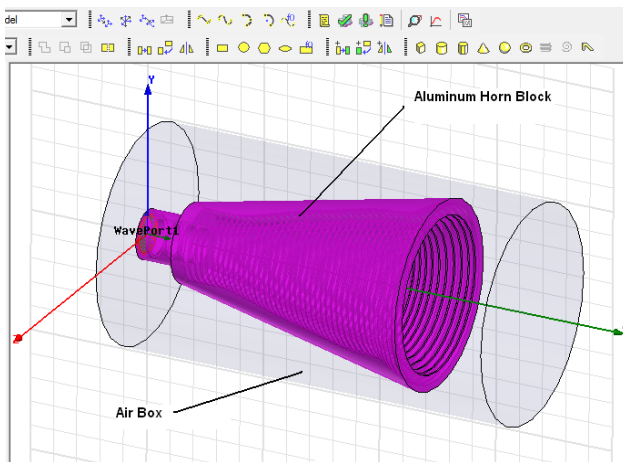


Figure 63. The spline-line corrugated horn geometry that was simulated whit the HFSS electromagnetic software tool.

4.4 Comparison of Horn Designs

In this section the three different designed feed horns are compared in terms of their dimensions and simulation performances. Table 26 presents the details of this horn design comparison.

Table 26. Parameter designs and simulation results of the 3 different corrugated horn profiles.

HORN PROFILE GEOMETRY:	Preliminary Conical			Optimized Conical			Spline-line with Corrugations		
Input aperture (mm): a_i	3.85			3.95			3.81		
Output aperture (mm): a_o	14			15			15.75		
Corrugation length (mm): L	120			132			51.25		
Total length ⁽¹⁾ (mm): L_{tot}	140			152			62.67		
Flare angle (deg): α	4.85°			4.79°			-		
Mode converter type:	<i>variable-pitch-to-width-slot</i>			<i>variable-depth-slot</i>			<i>variable-depth-slot</i>		
Slot depth MC ⁽²⁾ (mm): d_{mc}	3.5 – 1.8			3.5 – 1.8			3.35 - 2.2		
Slot depth TS ⁽³⁾ (mm): d_j	1.8			1.8			2.2		
pitch ratio: p	3			3			1.25		
Total number of slots: N	40			44			41		
Total number of slots MC: N_{mc}	12			7			6		
pitch-to-width ratio MC: δ_{mc}	0.83 – 0.5			0.5			0.248		
slot teeth width MC (mm): w_{jmc}	2.5 - 1.5			1.5			0.31		
pitch-to-width ratio TS: δ_{ts}	0.5			0.5			0.248		
slot teeth width TS (mm): w_{jts}	1.5			1.5			0.31		
corrugated-surface profile type:	Linear			Linear			Gaussian		
HORN SIMULATION RESULTS:	Preliminary Conical			Optimized Conical			Spline-line with Corrugations		
	31GHz	38GHz	45GHz	31GHz	38GHz	45GHz	31.3GHz	38GHz	45GHz
Reflection (dB):	-28	-33	-32	-22	-35	-30	-31	-32	-30
Cross polarization +45deg (dBi):	-25	-32	-29	-29	-38	-28	-31	-39	-40
Cross polarization -45deg (dBi):	-25	-32	-30	-29	-38	-30	-31	-38	-42
Side lobe levels, E-field (dBi):	-29	-27	-25	-27	-27	-26	-32	-28	-28
Side lobe levels, H-field (dBi):	-26	-26	-27	-32	-27	-27	-34	-30	-26
$1/e^2$ beam radius, E-field (deg):	22.38	17.08	14.32	21.14	16.32	13.42	20.89	17.45	14.27
$1/e^2$ beam radius, H-field (deg):	20.53	16.65	14.39	20.01	16.18	13.58	20.50	17.57	14.41
Reflection loss 100% band (dB):	< -26			< -22			< -23		

(1) The total length of the horn includes the thread section plus the input circular waveguide length.

(2) MC = Mode Converter of the horn profile.

(3) TS = Thread Section of the horn profile.

After a careful comparison of the three different designs it is clear that the spline-line horn design will be the best choice to be implemented in our receiver. Its major advantages are its compact size, good beam symmetry, low cross-polarization levels, complying with all the specifications. However, probably its biggest drawback will be when constructing the corrugation profile with the milling machine due to the tooth size with respect to the pitch ratio. It also remains to check how good it will be the alignment of the two block pieces and how it will affect the measurements when testing this horn.

4.5 Horn Construction and Experimental Measurements

4.5.1 Construction of the Corrugated Spline-line Horn

The spline-profile corrugated horn was constructed using the split-block technique. Both split sections were milled using a five-axis high-precision CNC milling machine [68]. The horn was milled in aluminum due to its good machinability and suitability for cryogenic applications. The corrugation profile at the split plane was checked with an optical microscope. No construction errors and misalignment of the corrugations were found. This sets the construction and alignment precision in less than 10 μm . Instead of using standard alignment pins, four pins were machined directly in one of the block surfaces minimizing in this way the alignment errors once the horn was assembled. The constructed horn is presented in Figure 64 and a more detailed CAD drawing is attached at the appendix section 7.2 of this document.

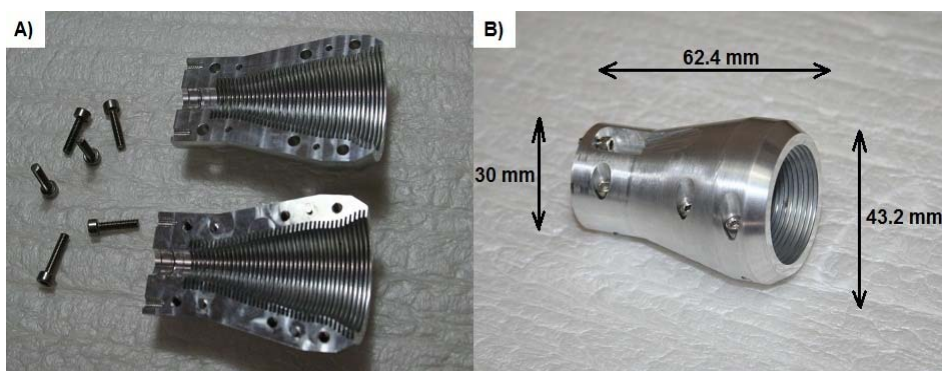


Figure 64. Constructed Spline-Line corrugated profile horn using CNC machining and split-block techniques.

4.5.2 Beam-pattern Measuring Setup

For the characterization of the horn, a vertical planar near-field beam-pattern measurement setup [100][101] was designed and built specifically for this work [102]. The near-to-far-field data-transformation algorithm, which uses a Fast Fourier Transform (FFT), and the probe amplitude pattern corrections were adapted from [103]. The beam scanner setup consists in an transmitting 30-50 GHz probe attached to a XY θ -linear scanner, a mount holding the horn to be tested, a XY-scan controller, an Agilent 10-MHz-50-GHz Vector Network Analyzer, and a PC used to and control the other hardware devices (through an Ethernet-bus and RS-232 interfaces) and store the measured data. The Vector Network analyzer output channel is connected to the transmitting horn while its input channel is connected to the receiver horn. Both connection channels use flexible 1-to-50 GHz coaxial-cables of 2-meter long each. The probe is attached to a θ -rotating stage that can set at 0° when performing co-polar beam measurements or be manually rotated to 90° when taken the cross-polar scans. In Figure 65 it is shown the schematic beam-scanner arrangement.

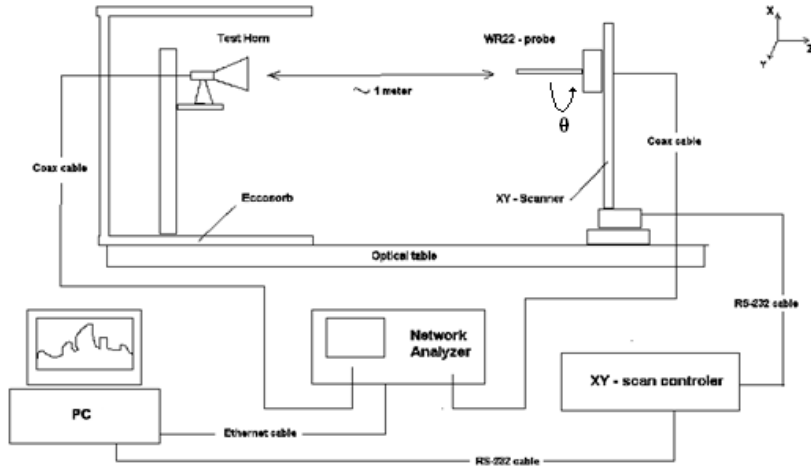


Figure 65. Schematic view of the lab setup arrangement that it was used to test the performance of the horn, and the horn-lens arrangement.

4.5.3 Horn Measurements

In this section we present the measured horn reflections at all frequencies, and the co-polar and cross-polar radiation pattern, horn directivity, phase and phase center location at 31.3, 38 and 45 GHz. All the measured data presented here includes the corresponding HFSS simulations for comparison purposes. The resulting measured far-field data were consistent within a dynamical range of greater than 50 dB. For determining the phase center a phase model with amplitude weighting correction was used [104].

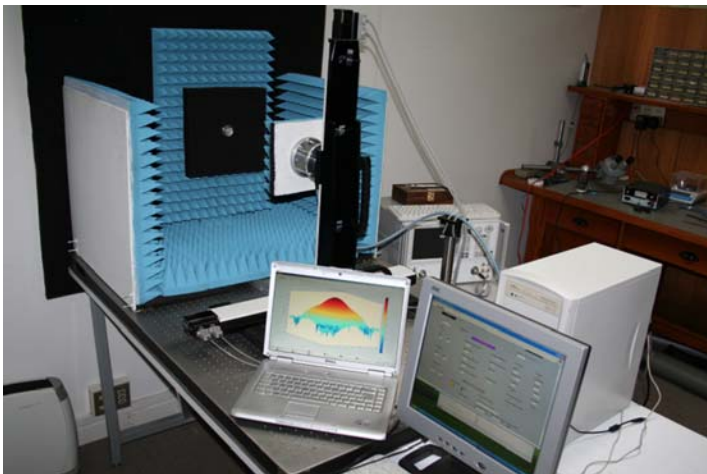


Figure 66. Near-field beam scanner setup showing the XY-scanner, the Horn, the VNA and the main computer used to control the measuring setup.

The picture shown in Figure 66 shows the measuring setup used to characterize the corrugated horn. Note how the pyramidal Eccosorb absorbers [105] were placed around the horn under test and behind the probe to minimize reflection interferences when performing the measurements.

4.5.3.1 Reflection Coefficient

Figure 67 presents the measured reflection losses at the input port of the horn. The measurements correspond to the real circular waveguide input. The contribution of the rectangular-to-circular waveguide transition was subtracted using a previous calibration step. The measurements show that the reflection losses are less than -20 dB for the complete band of interest in excellent agreement with the simulations.

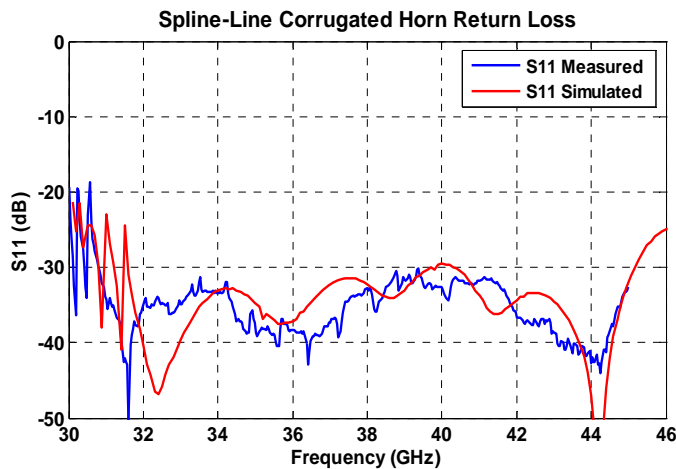


Figure 67. Measurements of the horn input reflections (*red line*) compared to the HFSS simulated expected S11 values (*blue line*).

4.5.3.2 Co- and Cross-polar Patterns

The co-polar and cross-polar radiation patterns are shown in Figure 68. The copolar measurements are identical to the simulated ones down to -25 dB at all frequencies. At lower amplitude values, especially around the first sidelobe levels, the measurements are always somewhat large with respect to the simulations. The difference in cross-polar amplitude between the simulations and measurements, especially at 38 and 45 GHz, are of about $+5$ dB. However, all the cross-polar and first sidelobe level measurements fulfill the horn-performance specifications.

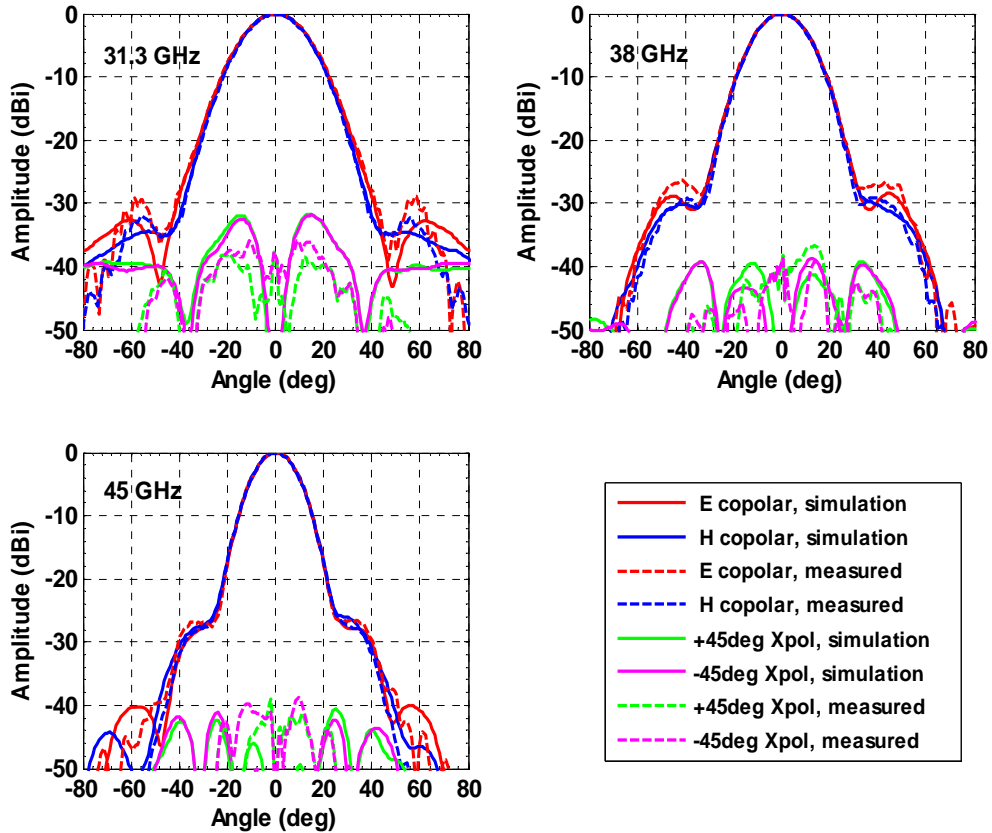


Figure 68. Measured and simulated co-polar (E and H planes) and cross-polar (45 and -45 planes) radiation pattern comparison for 31.3, 38 and 45 GHz. Dotted lines correspond to the measurements results while the straight lines corresponds to the simulation results.

4.5.3.3 Directivity and Level of the First Side-lobe

From the simulated and measured radiation patterns we have obtained the directivities and the levels of the first side-lobes. The results are summarized in Figures 69 and 70. In both cases, the measured and simulated values show similar frequency dependence. In the case of the measured directivities, they are slightly overestimated in around 0.3 dB for each case. This is probably due to the uncertainty when predicting the total isotropic radiated power of our horn from the planar near-field measurement once the far-field transformation is done using the FFT methods. Regarding the first side-lobe level, it is typically below -26 dB across the whole band, which implies that the specifications set for the horn are satisfied.

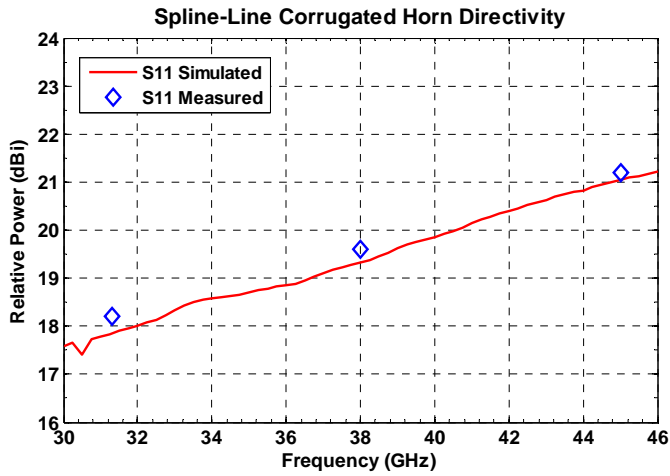


Figure 69. Measured and predicted directivity of the constructed horn.

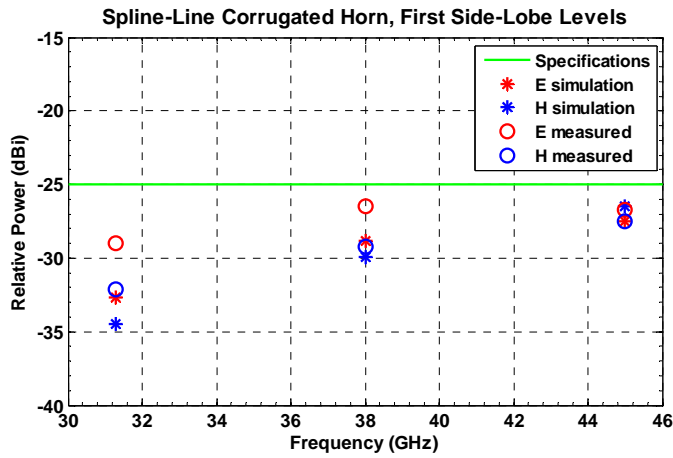


Figure 70. Measured and simulated first side-lobe levels. The *green dotted line* denotes the maximal first side-lobe level specification of the horn.

4.5.3.4 Phase Plots and Phase-center Location

The measured phase of the E and H fields and their corresponding simulated HFSS values at 31.3, 38 and 45 GHz are shown in Figure 71. The measured results agree very well with the simulations since the phase diagrams are quite flat in the region where the amplitude radiation reaches its maximum. In Figure 72 the phase center location (PCL) retrieved from the measured and simulated cases are presented. The measured PCLs coincide with the simulated cases within about 0.5 mm. The exception is the PCL of the H-field at 45 GHz, where the difference with its corresponding simulated value is of about 1.5 mm. This discrepancy may be attributed to small construction imperfections in the corrugation profile which is more sensitive at higher frequencies.

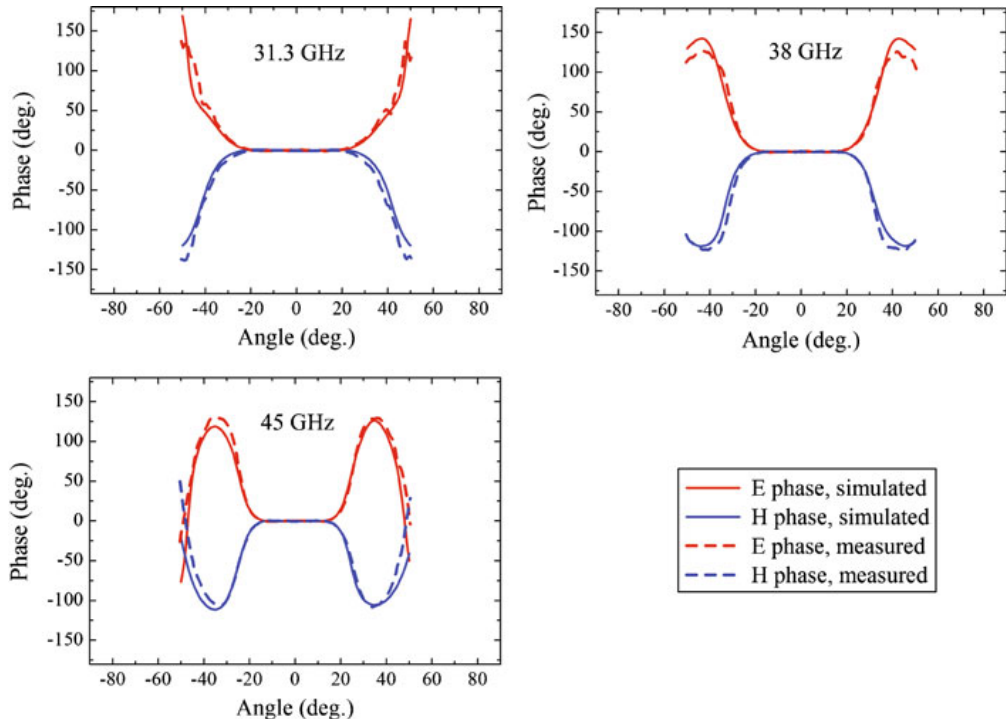


Figure 71. Measured and simulated phase plots results for the E (red lines) and H planes (blue lines) at 31.3, 38 and 45 GHz.

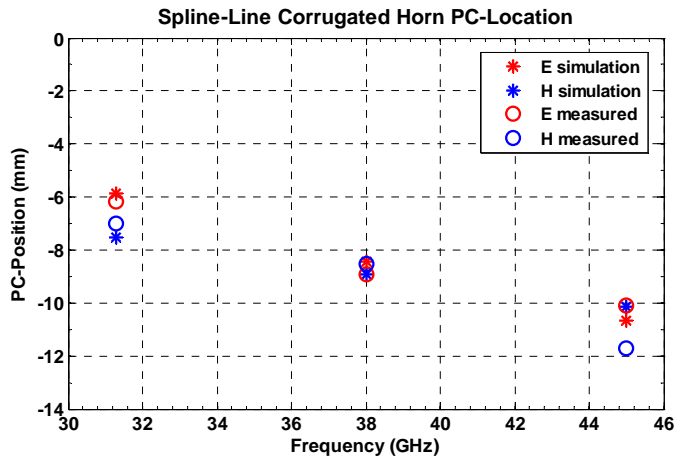


Figure 72. Measured and simulated phase center locations for the E (red) and H fields (blue).

4.5.4 Horn and Lens Measurements

The performance of the dielectric lens together with the corrugated horn was tested by using the same beam-scanner system setup, but now placing this lens in between the horn-probe arrangement. The lens was attached on top of a xyz-stage flexure platform that can be tuned with millimetre precision, which then provides that the lens center becomes align with the horn center optical axis. The stand holding the xyz-stage flexure platform was also cover with Eccosorb to minimize reflexion interferences. This optical beam scanner modified arrangement is shown in Figure 73. The horn lens distance was set to 19.1 cm and the distance between the lens and the scanner probe aperture was of 66.0 cm. Once the arrangement was set and aligned, the co-polar and cross beam scanner measurements were performed.

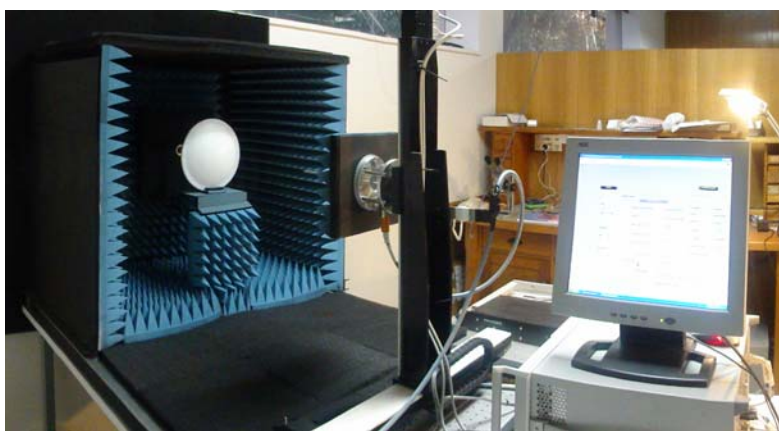


Figure 73. *Near-field beam-scanner arrangement setup used for the horn-lens co and cross-polar beam measurements.*

4.5.4.1 Co-polar Pattern Measurements

Figure 74 shows a two-dimensional representation of the measured co-polar beam pattern measurements at 31.3, 45, and 45 GHz. The left-side plots correspond to the near-field measurements, while the right-side ones correspond to the far-field transformed plots. In these plots it can be found that the far-field transformed patterns contained inside the subreflector surface area (cyan circle) are very symmetric but having a little offset towards the x and y positive axis. This offset is probably due to a not-well-aligned horn-lens setup while performing the measurements. The low side-lobe, measured levels outside the subreflector area are consistent with the specifications since the maximum peak is less than -25 dB.

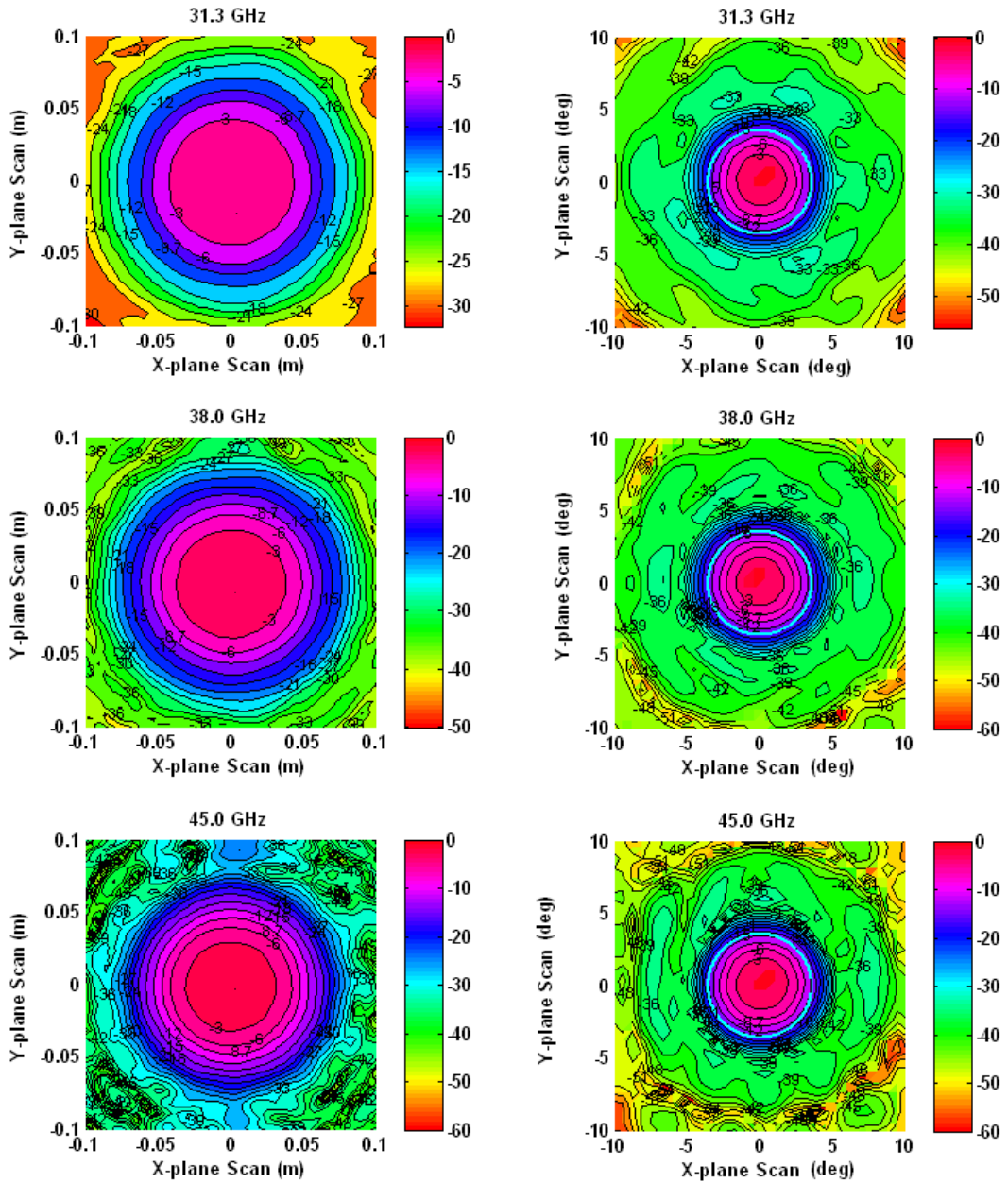


Figure 74. Near-field co-polar horn-lens measurements (left) and their corresponding far-field transformation (right) at 31.3, 38, and 45 GHz. Note also the cyan circle that denotes the subreflector rim projection on the far-field patterns. Contour levels are shown at every -3dB .

4.5.4.2 Cross-polar Pattern Measurements

The measured near field cross-polar patterns at 31.3, 38, 45 GHz are shown at the left side part of Figure 75. Their corresponding far-field transformed pattern is presented at the right side of the same figure. The cross-polar peaks were found to be less than -30 dB for all the three measured patterns which comply with the designed goals.

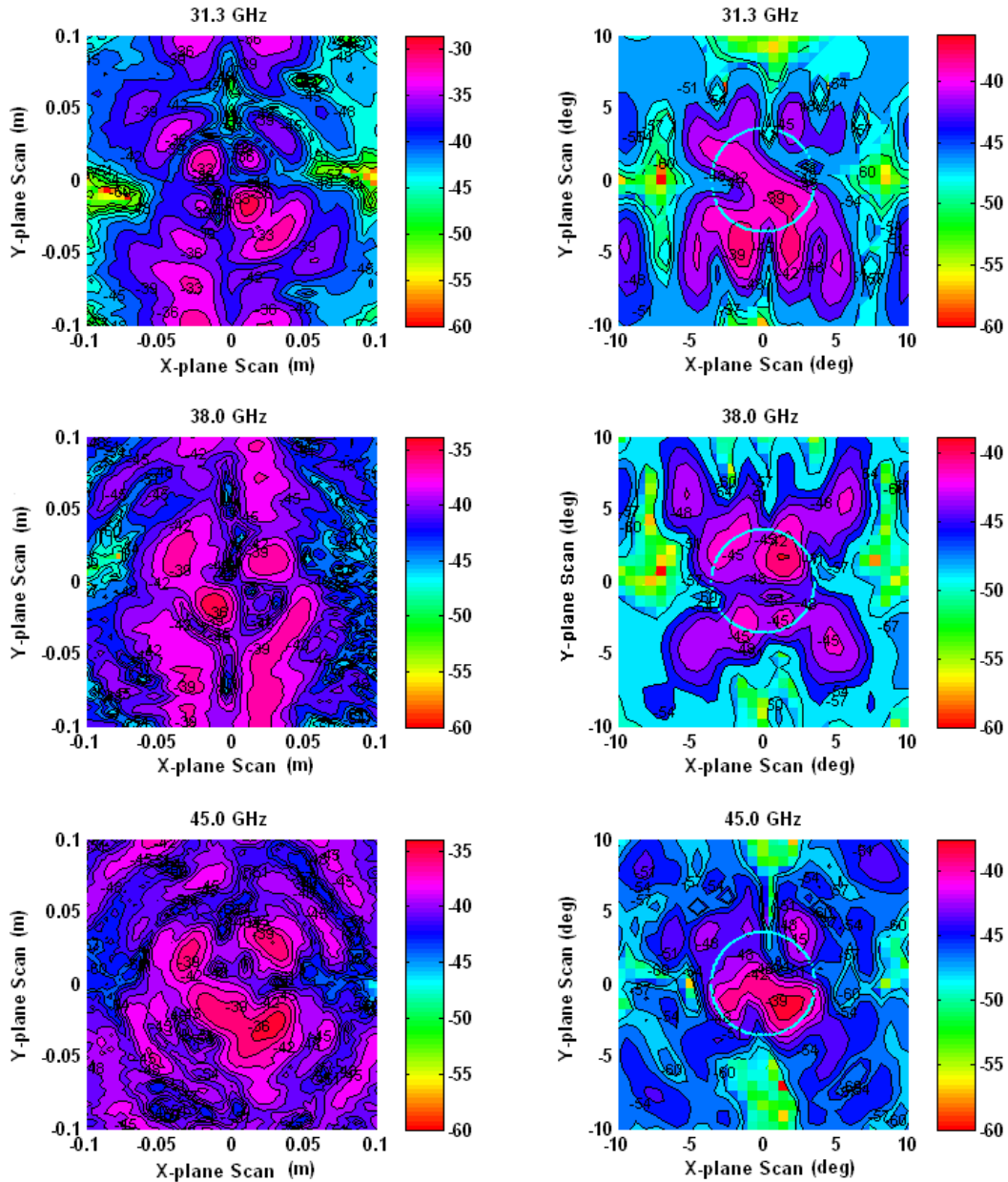


Figure 75. Near-field horn-lens cross-polar measurements (left) and their corresponding far-field transformation (right) at 31.3, 38, and 45 GHz. The cyan circle denotes the subreflector maximum radius. Contour levels are shown at every -3dB.

4.5.4.3 Experimental Antenna Efficiency Estimation

From the far-field transformed patterns the antenna efficiency can be estimated at the subreflector within its 0.75 m of diameter, which corresponds to a projection radius of 3.58° over the far field beam patterns. The details of this projection are shown in Figure 76, where the far-field co-polar patterns are presented at 31.3, 38, and 45 GHz.

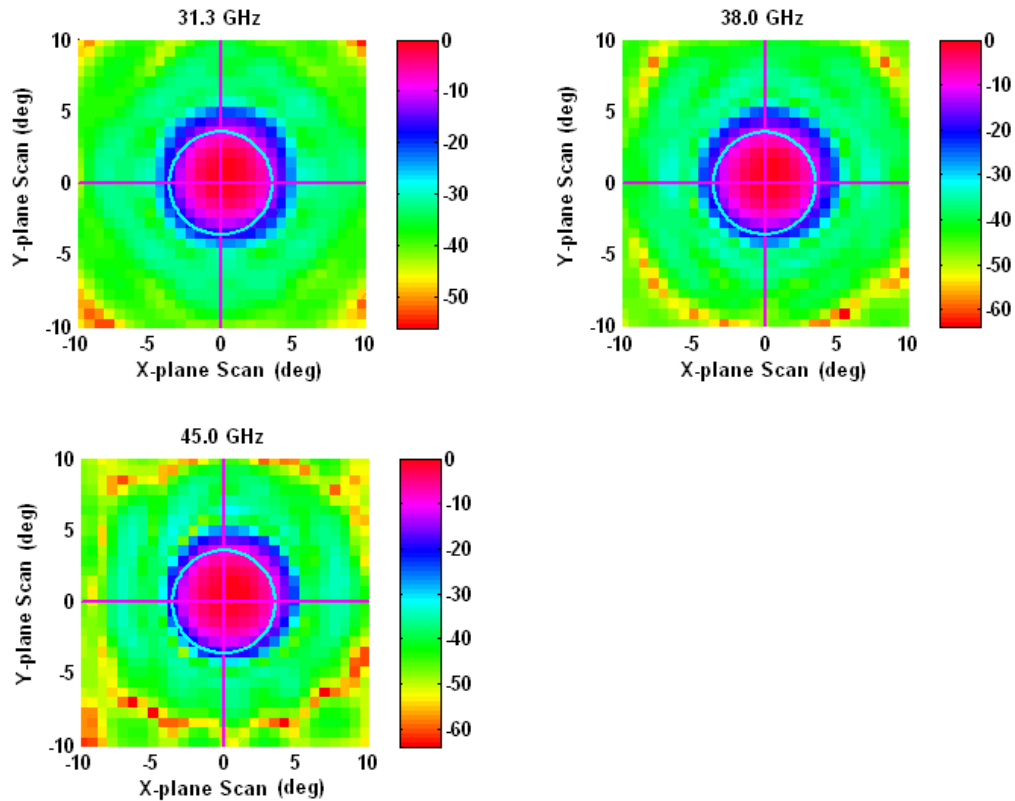


Figure 76. Full resolved far-field co-polar horn-lens measurements. This figure shows also the far-field projection of the subreflector over the measured patterns from which it can be noted that the horn-lens alignment was not perfect during the tests.

The different antenna efficiencies terms and they overall total contribution were calculated according to the methods presented in [106][107]. In Table 27 are presented the different antenna efficiency terms that were estimated from the measured co and cross-polar patterns. Those are: the spillover, polarization, taper, and phase efficiencies. The total predicted antenna efficiency, which is also been listed in the same table, will be then the product of these four individual terms.

As it can be noted, the estimated total antenna efficiency is lower than the expected specification of 80% listed in Table 23. This is probably caused by the lens radial and axial misalignment with respect to the optical axis determinate by our corrugated horn. In Figure 76, the effect of lateral defocus can be noted since all the measured beam patterns show an offset of about $+1^\circ$ with respect to the center of the subreflector rim in both x and y positive directions.

Table 27. Band-1 estimated antenna efficiencies summary.

Freq. (GHz)	n_{spil}	n_{pol}	n_{tap}	n_{phase}	n_{tot}
31.3	0.9095	0.9993	0.8542	0.9999	0.7764
38.0	0.9329	0.9996	0.8348	0.9999	0.7786
45.0	0.9324	0.9997	0.8409	0.9999	0.7838

4.6 Quasioptical Beam Analysis Corrections

Finally, as the last section part of this Chapter 4, it is important to estimate how the measured patterns and phase-center positions from section 4.5.3, change the beam propagation in our simulated optical system from section 3.3.3.1. These new measured horn parameters will then determinate the new lens surface shape, its focal length, and its distance to the corrugated horn aperture. In Table 28 we summarize the most important designing parameters of our simulated optical system with the new corrected parameters. Figure 77 shows the final Quasioptical beam-propagation that corresponds to the “corrected values” parameter column listed in Table 28.

Table 28. Corrected optical beam propagation estimated from the spline-line corrugated horn measurement results.

Parameter:	Simulation Values:	Corrected Values	Δ Difference:
Beam waist w_0 : ⁽¹⁾	31.3 GHz = 9.780 mm 38.0 GHz = 9.540 mm 45.0 GHz = 8.840 mm	31.3 GHz = 8.456 mm 38.0 GHz = 8.211 mm 45.0 GHz = 8.486 mm	+ 1.324 mm + 1.329 mm + 0.354 mm
Phase center location:	31.3 GHz = - 6.240 mm 38.0 GHz = - 9.670 mm 45.0 GHz = - 16.210 mm	31.3 GHz = - 6.590 mm 38.0 GHz = - 8.735 mm 45.0 GHz = -10.895 mm	+ 0.350 mm - 0.935 mm + 5.315 mm
Focal length f: Total lens thickness: Distance horn-lens:	0.1740 m 0.0581m 0.1790 m	0.1700 m 0.0591 m 0.1800 m	- 0.0040 m + 0.0010 m + 0.0010 m
Subreflector illumination Tapper: ⁽²⁾	31.3 GHz = -12.3190 dB 38.0 GHz = -12.3317 dB 45.0 GHz = -12.3576 dB	31.3 GHz = -12.2173 dB 38.0 GHz = -12.8011 dB 45.0 GHz = -12.3975 dB	- 0.1017 dB + 0.4694 dB + 0.0399 dB
Total Noise Contribution:	31.3 GHz = 10.034 K 38.0 GHz = 9.264 K 45.0 GHz = 10.142 K	31.3 GHz = 14.427 K 38.0 GHz = 10.622 K 45.0 GHz = 10.372 K	+ 4.393 K + 1.356 K + 0.230 K

⁽¹⁾ Estimated using the average of the E and H-field $1/e^2$ beam radius (deg) and applying Equation (17).

⁽²⁾ Optimization target criteria = -12.3 dB.

The results presented in Table 28 were obtained in the following way:

- i) All the theoretical simulation values listed in the second column comes from section 3.3.3.1. More specifically from Tables 12, 13, and 14.
- ii) The corrected values of the phase-center location correspond to the measured phase center locations presented in Figure 71, section 4.5.3.4.
- iii) The Beam waist corrected values were estimated using the average of the measured E and H-field $1/e^2$ beam radius, which were extracted from Figure 68, and applying Equation (17).
- iv) Finally, the total noise contribution corresponding to the constructed spline-line horn measurements was estimated by changing the lens position and its focal length until a subreflector illumination target of -12.3 dB was achieved.

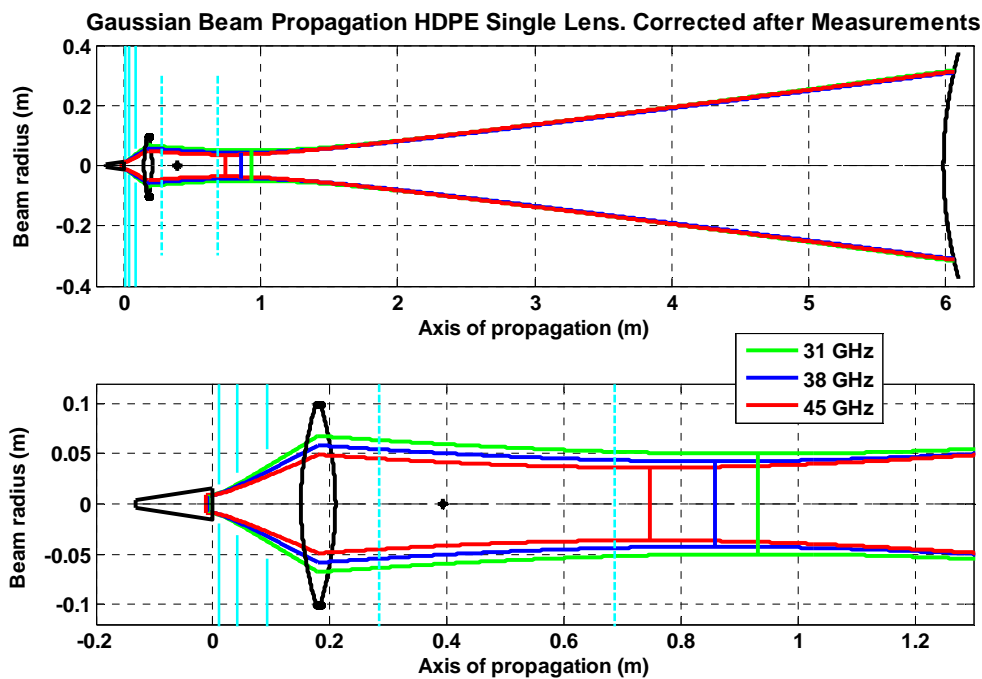


Figure 77. Corrected horn-subreflector Gaussian beam propagation through the HDPE Lens and IR-Filter.

The new corrected Quasioptical beam propagation was optimized using the -12.3 dB subreflector illumination criteria. As it can be seen in Table 28, the subreflector taper efficiency could not be optimized with the target criteria at all frequencies, meaning that the antenna is not 100% perfectly frequency independent as desired. Another important fact that can be extracted from this table is that the noise temperature increases, especially at the lower frequencies due to the fact that the outgoing beam becomes wider and more truncated by the aperture size of the IR-filters and the lens optical components. A more detailed noise estimation of the final optical-system resulting design is presented in Table 29.

Table 29. Corrected Total gain and noise contribution of the optical system estimated from the horn experimental results.

Component Description:	Component Gain [dB]			Cumulative Gain [dB]			Component Noise [K]			Cumulative Noise [K]		
	31.3GHz	38GHz	45GHz	31.3GHz	38GHz	45GHz	31.3GHz	38GHz	45GHz	31.3GHz	38GHz	45GHz
Lens (Dielect. Loss)	0.984	0.981	0.978	0.984	0.981	0.977	4.792	5.828	6.914	4.792	5.828	6.914
Lens (Reflect. Loss)	0.990	0.990	0.990	0.974	0.971	0.967	2.050	2.050	2.050	6.875	7.918	9.012
Lens (Truncat. Loss)	0.987	0.999	1.000	0.962	0.968	0.967	2.661	0.575	0.041	9.607	8.511	9.055
CryoTop Aper. (Trunc.)	0.989	0.999	0.999	0.950	0.965	0.967	2.421	0.597	0.062	12.124	9.176	9.120
110K-filter (Diel. Loss)	0.998	0.997	0.996	0.948	0.962	0.963	0.276	0.335	0.397	12.419	9.425	9.530
110K-filter (Refl. Loss)	0.997	0.997	0.997	0.945	0.959	0.960	0.498	0.498	0.498	12.940	9.992	10.047
110K-filter (Trun. Loss)	0.993	0.999	0.999	0.938	0.957	0.960	1.162	0.376	0.084	14.167	10.384	10.135
15K-filter (Diel. Loss)	0.999	0.999	0.999	0.937	0.957	0.959	0.007	0.009	0.010	14.177	10.393	10.146
15K-filter (Refl. Loss)	0.997	0.997	0.997	0.934	0.953	0.956	0.198	0.198	0.198	14.388	10.600	10.352
15K-filter (Trun. Loss)	0.999	0.999	0.999	0.934	0.953	0.956	0.036	0.021	0.020	14.427	10.622	10.372

4.7 Conclusions

We have successfully designed and constructed a spline-profile optimized corrugated horn using split-block techniques. The measurements of its return losses, directivity, first side-lobe levels, and its co- and cross-polar radiation pattern measurements agree very well with the HFSS simulation results and fulfill all the required specifications imposed by ALMA for its Band 1. Furthermore, it was demonstrated that the construction discontinuities, due to the horn being split in two parts, were negligible and causes no detectable anomalies in the cross polar measured pattern. But probably the main advantage is that our horn design is about 9 cm shorter in length than the conventional horn design, which make it our horn easier to be installed on top of the 15-K cryostat-plate together with the other cold receiver components, such as the HEMT amplifier.

The horn-lens measured co-polar patterns look very symmetric for both, the E and H-fields, and the measured cross-polar peaks are less than -30 dB for all the measured frequencies. However, we estimated that the total noise contribution at lower frequencies, i.e. 31.3 GHz, was about 3K higher than expected. This probably was due to the uncertainty when estimating the beam waist size from the beam divergence angle that was taken from the radiation pattern at that frequency. In that particular measured pattern it was found that the total intensity at the top of such curve decreased within 0.2 to 0.4 dB (e.g. loss of power due to reflections at the lens surfaces), causing that, when normalized the measured pattern, it will give us a wider divergence angle and, thereby, it increased the estimated noise performance at 31.3 GHz due to truncation losses. Therefore this measurement must be repeated once the lens being treated with a proper antireflection layer that minimizes the power losses

Chapter 5

OMT Design and Construction

Among the three different OMT designs described in section 2.7, we have chosen the design introduced by S. Asayama for ALMA Band-4 [108]. This design support a wide range of frequencies, its implementation can be very compact, it has the great advantage that can be easily machined using only three block pieces, and it does not require extra alignment effort as in the case of other mentioned designs. This chapter starts with a brief description of waveguide theory [109]. Afterward, this chapter describes with the details of the independent design and optimization of the three most important parts of the OMT. Then, all these three sections are connected together and re-optimized to get the best possible performance. Finally, the device was constructed and measured.

5.1 Introduction

In millimeter and sub-millimeter receivers there are two different kinds of techniques to achieve dual-polarization detection. One is the quasi optical scheme that uses a polarizer grid in between of an arrangement of mirrors that split the input beam into two orthogonal linear polarizations. The second method is by using a special waveguide polarization diplexer called Ortho-Modal Transducer (OMT). For millimeter operation, as is the case of ALMA Band-1 receiver, the chosen technique is the OMT due to its compactness and wideband support rather than using the Quasioptical arrangement, which can be large and bulky at low frequencies. For our ALMA Band-1 prototype receiver, the main technical specifications for this OMT are summarized in Table 30 [71].

Table 30: The ALMA Band1 OMT main specifications are:

Parameter:	Specification:
Reflections:	< - 20 dB
Cross polarization:	< - 30 dB
Isolation	< - 50 dB
Bandwidth	= 31-45 GHz

5.2 Waveguide Basics

A waveguide is a hollow conductive metal-pipe structure that guides radio or microwaves. Inside the waveguide, the wave signals are confined inside due to total reflection from its walls. There are different shapes of waveguides, most commonly having circular and rectangular cross-sections. The transversal size of the latter is commonly selected such that its long side is twice its short side. The rectangular waveguide is very useful for carrying microwaves signals that have a horizontal or vertical polarization respect to them. One of the most important parameters that characterize such waveguide is the so called *cut-off frequency*, which is the lowest frequency that a certain mode can propagate through the guide. The *propagation mode* is the possible solution form that the wave equation can generate due to the boundary conditions constraints imposed by this kind of waveguide. They are limited in frequency and shape, and according to [110], the relationship between those frequencies and the corresponding modes for a rectangular waveguide are given by the following equation:

$$f_{cutoff} = \frac{1}{2\pi\sqrt{\epsilon\mu}} \sqrt{\left(\frac{m\pi}{a}\right)^2 + \left(\frac{n\pi}{b}\right)^2} \quad (99)$$

Where:

a = waveguide width

b = waveguide height

m = integer number of $\frac{1}{2}$ -wavelength variations of fields in the " a " direction

n = integer number of $\frac{1}{2}$ -wavelength variations of fields in the " b " direction

ϵ = permittivity of the material inside the waveguide

μ = permeability of the material inside the waveguide

The dominant mode, also called fundamental mode, in a rectangular waveguide is the "Transverse Electric" TE_{10} (see Fig. 78). This mode is the one that concentrates most energy than the other higher modes since is the less attenuated. Note that for the TE_{mn} mode, m or n can be zero but not at the same time. Most of the microwave devices that use waveguides use the fundamental TE_{10} mode in their design. However, rectangular waveguides do also allow the propagation of "Transverse Magnetic" modes TM_{mn} where Equation 99 can be used to calculate the corresponding cutoff frequency. As in most of rectangular-waveguide devices, our OMT will use the fundamental mode in its design and the standard waveguide size to be used will be WR-22, which have a cross section width of 5.69 mm and height of 2.845 mm.

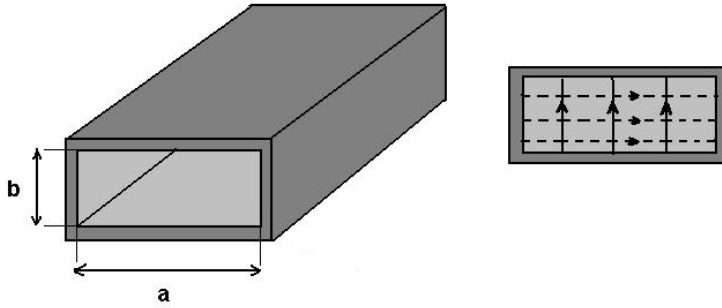


Figure 78. The geometry of a rectangular waveguide (left figure) with width a and height b . The field lines (right figure) for the TE_{10} mode where the solid lines correspond to the E -field while the dashed lines show the H -field.

Table 31 presents the first five TE and TM mode orders that can propagate, according to Equation 99, through the standard WR-22 waveguide and their corresponding cutoff frequencies. Note that only the TE_{10} mode can be excited within the 31-to-45 GHz frequency band, and the other higher TE_{20} and TE_{01} modes, and the first allowed TM_{11} mode will be excited at much higher frequencies, which is very straightforward for our design since the fundamental TE_{10} mode will not be share any energy with the other higher modes. Equation 99 also tells us that the TE_{10} mode depends only of the waveguide-width parameter a , which means that the height b can change in size (thus changing the waveguide impedance) without affecting the propagation of this mode [111].

Table 31: WR-22 rectangular waveguide lowest cutoff frequency modes.

Cut-off freq. / Order	$m=1, n=0$	$m=2, n=0$	$m=0, n=1$	$m=1, n=1$	$m=2, n=1$
TE_{mn} (GHz)	26.36	52.72	52.72	58.95	74.56
TM_{mn} (GHz)	-	-	-	58.95	74.56

Another important basic parameter that is needed in the design of microwave waveguide components is the so called *guided wavelength*, which is defined as the as the distance between two equal phase planes along the waveguide. This quantity depends on the lower cutoff frequency of the waveguide and is longer than the corresponding wavelength in free space, meaning that the dielectric constant inside the waveguide is less than unity. The guided wavelength is very useful when designing stepped waveguide transformers sections [112] that match smoothly waveguide sections with different cross-section sizes and therefore with different impedances. The typical waveguide length of these sections are equal or closer to the $\frac{1}{4}$ of a guided wavelength, calculated at the center frequency of the designed device bandwidth, which then results in a minimization of the standing waves generated between two waveguides with different impedances [113]. The guided wavelength in a rectangular waveguides is given by:

$$\lambda_{guided} = \frac{c}{f} \times \frac{1}{\sqrt{1 - \frac{c}{2af}}} \quad (100)$$

Where:

a = waveguide inside width

c = speed of light

f = frequency

In general, rectangular waveguides are made of high conductivity metals such as steel, aluminum, copper or even brass, but then coated internally with a very thin layer of a high conducted metal such as silver or gold. Thus, there will be attenuation on the transmitted signal that will depend on the frequency, waveguide material, propagation mode type, cutoff wave-number, waveguide cross-section dimensions, and length of the waveguide section. Table 32 summarizes the most common materials used to construct (or to coat) waveguides and waveguide devices and their corresponding conductivities.

Table 32: The conductivity of different materials chose to coat the inside walls of the rectangular waveguide. Values were taken from [114].

Material	Conductivity σ [S/m]
Silver	6.17×10^7
Copper	5.80×10^7
Gold	4.10×10^7
Aluminum	3.54×10^7
Brass	1.54×10^7

According to [115], the attenuation losses of the TE₁₀ mode inside a waveguide was can be calculated from the following equation:

$$\alpha_{TE_{10}} = \frac{R_m}{ab\beta_{10}k_0Z_0} (2bk_{c,10}^2 + ak_0^2) \quad [\text{Np/m}] \quad (101)$$

Where the surface resistance R_m is given by:

$$R_m = \sqrt{\frac{\omega\mu_0}{2\sigma}} = \sqrt{\frac{2\pi f\mu_0}{2\sigma}} = \sqrt{\frac{\pi f\mu_0}{\sigma}} \quad [\Omega]$$

And the phase constant β_{10} , the wave number in free space k_0 , and the TE₁₀ mode cutoff wave-number $k_{c,10}$ are given by:

$$\beta_{10} = \sqrt{k_0^2 - k_{c,10}^2} \quad [\text{m}^{-1}]$$

$$k_0 = \frac{2\pi}{\lambda_0} = \frac{2\pi f}{c_0} \quad [\text{m}^{-1}]$$

$$k_{c,10} = \frac{\pi}{a} \quad [\text{m}^{-1}]$$

The impedance of free space $Z_0 = 377\Omega$, permeability of vacuum $\mu_0 = 4\pi \cdot 10^{-7}$ H/m, speed of light in vacuum $c_0 = 3 \cdot 10^8$ m/s (speed of light in vacuum), and the conductivity σ of the waveguide material (see Table 32).

Figure 79 illustrates the different theoretical attenuation obtained when using equation 101 for a WR-22 standard waveguide size made of (or coated with) different materials listed in Table 32. The calculations were performed with the help of Matlab and cover the frequency range from 31-to-45 GHz.

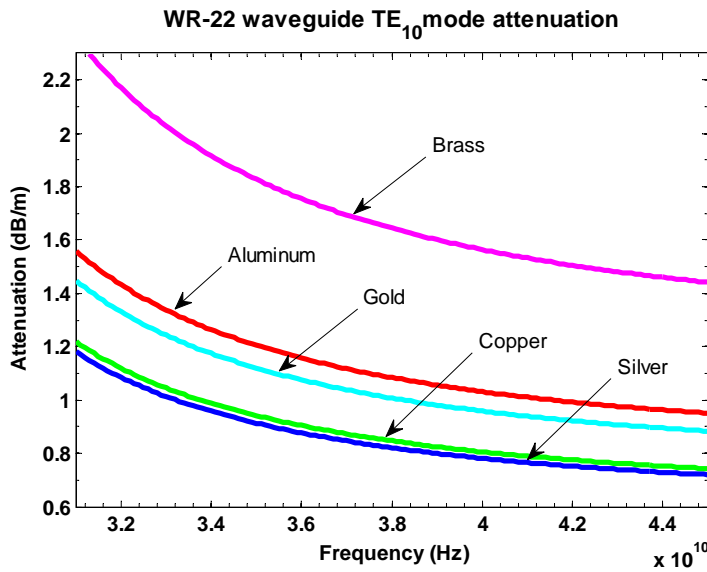


Figure 79. The TE_{10} mode attenuation as a function of frequency for a WR-22 waveguide using different materials.

As it can be confirmed in the attenuation results shown in Figure 79, the material that contributes with more attenuation is brass, while the best performance is given by silver and copper. The problem when using silver and copper materials is that they oxide with time, which is the opposite case gold and aluminum that are much less sensitive for oxidation. However, gold is too expensive and, therefore, for the construction for our OMT device, as it was also for the case of the spline-line corrugated horn, the choice of material was aluminum. Moreover, aluminum is easy to machine, cheap for mass production and, even if it attenuates more the signal than other materials, this is not a big concern since the waveguide channels of the proposed OMT design will only be few centimeters long, making the total signal attenuation of such device not very significant.

5.3 Orthomodal Transducer Design

The “Dual Ridge” Orthomodal Transducer that we are interested to construct is based on S. Asayama’s work for the ALMA Band-4. This OMT device was designed to work from 125-to-169 GHz, which corresponds to a 30% of bandwidth, and should be fully scalable. On the other hand, our Band-1 design will cover the frequency range of 31-to-45 GHz that corresponds to a 36% of bandwidth. Then, if the Band-4 OMT is scaled down to fit the Band-1 requirements, this fitted polarization diplexer device will have approximately a 6% of bandwidth out of specifications. In summary, we will need to optimize and redesign the most critical section parts of the original Asayama’s design. Those sections are: (1) the dual-ridge section which splits the vertical and horizontal components of the detected signal in two different channels, (2) the E-bend section that changes the propagation direction with 90 deg of the outgoing vertical polarization signal generated by the dual-ridge section, and (3) the Y-combiner section that brings the two horizontal output channels that were split with equal amount of power by the dual ridge section.

All simulations and optimizations were performed using Ansoft HFSS. The optimizations were carried out using Optimetrics which is a powerful in-built HFSS capability that can perform fast automated parametric analysis and optimization. The main steps used to find the best optimized design on each one of the OMT main sections and the final OMT devices were the following:

- 1) A preliminary scaled model, taken from a previous existing and published literature design, was simulated in HFSS.
- 2) If the performance was not good enough, we proceeded to identify the most critical waveguide parts of each section that needed to be optimized. Then, we made an improvement in its geometrical structure according to the proper designing theory. We used a reflection minimum optimization target of -20 dB or less, to conclude the simulation.
- 3) We proceeded to a further optimization that takes into account a size reduction on the OMT section under study, keeping the same reflection target as before to finish the optimization.
- 4) If all the sections do fulfill the specifications, the next step is to connect all the parts together and perform a new fine tune optimization of the whole OMT until all the requirements listed in Table 30 are reached.
- 5) If the final OMT design is satisfactory, the device is constructed and measured. If not, steps 2 through 4 are repeated again until we reach the desired performance.

5.3.1 Dual-ridge Section Design

The dual-ridge waveguide polarization splitter concept was first introduced by A. Dunning [116], which it is the most important OMT section since it is responsible to split the measured signal into two orthogonal polarization channels. In this design, the vertical polarization input signal is concentrated between the two ridges at the center of the square waveguide and then exits the section through a straight waveguide called “main-arm”. Meanwhile, the horizontal polarization is split through into two independent “side-arm” channels (with an equal amount of power) using the so called right-angle-miter bends design for each arm [117] (see Fig. 80). Due to its symmetrical geometry, the higher order modes are very unlikely to be excited inside the dual-ridge section structure.

When optimizing this section, it was noted that the reflection losses decrease with the ridge thickness, but then, the number of steps need to be increased. For the case of the horizontal polarized signal, its reflection loss did decrease as the size of the main arm height decreased, but it also depended of how the so called E-plane bifurcation aspect ratio between b_m (mitre-wall-to-right-corner edge to the displacement) and the waveguide height b was designed [119]. Even when optimizing each polarization S-parameter independently, there was found that when improving one polarization channel performance, the other got worse and vice versa. So both polarization channels needed to be optimized at the same time when using Optimetrics, which was a very time consuming simulation process. In Figure 80 are shown the final simulated dual-ridge optimized results (left) and the final geometry (right). The simulated return loss was better than -22 dB for vertical polarization channel, while for the horizontal channel, a performance less than -28 dB.

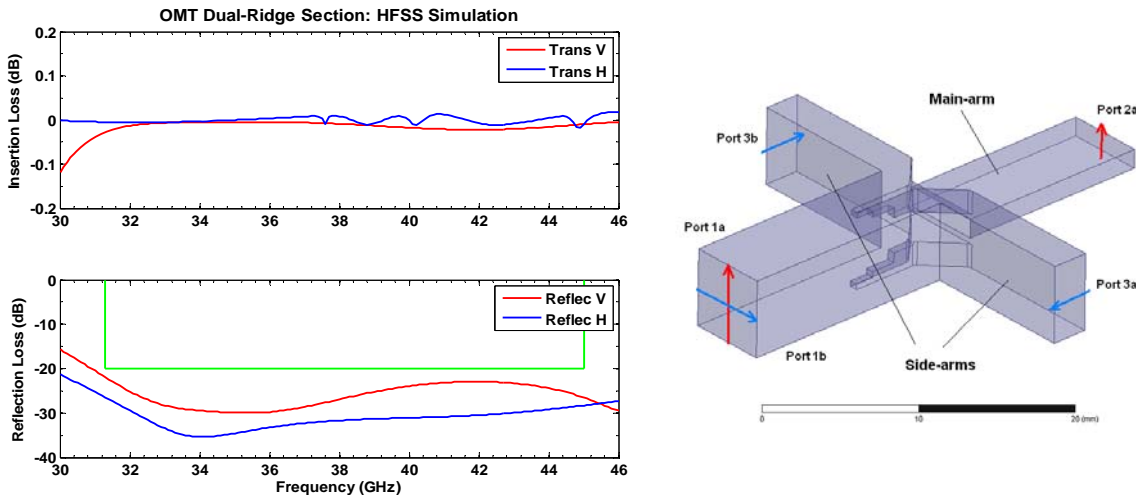


Figure 80. Left, the optimized OMT dual-ridge simulated insertion and reflection losses results. Right, the HFSS simulated section geometry showing its input ports 1a and 1b, output ports 2a and 3a-3b, and their respective polarization defined states V (vertical) and H (horizontal). Note also that the red arrow denotes the vertical polarization part of the signal while the blue one denotes the horizontal polarization.

5.3.2 E-bend Section Design

The main arm output of the OMT dual-ridge section that transmits the vertical polarized signal, has a height of 1.395 mm. Therefore it needs to use a stepped waveguide transform section [110] to match properly with the impedance of the OMT vertical output port that uses a WR-22 standard dimension. Furthermore, this waveguide output port needs to be re-directed by using an E-bend section of 90 degrees [118] not to collide with the OMT horizontal output port. Taking into account these two facts and also adding the need of minimizing the section size and accomplish the -20 dB reflection requirement, we found out that the best optimization results of this section was achieved when using a 3-step stepped transform section together with a 2-step E-bend section designs. The final geometry shape of this section is shown in right part of Figure 81. At the left panel of Figure 81, the final optimized simulation results of the E-bend section are presented. The return loss was less than -25 dB for the whole band.

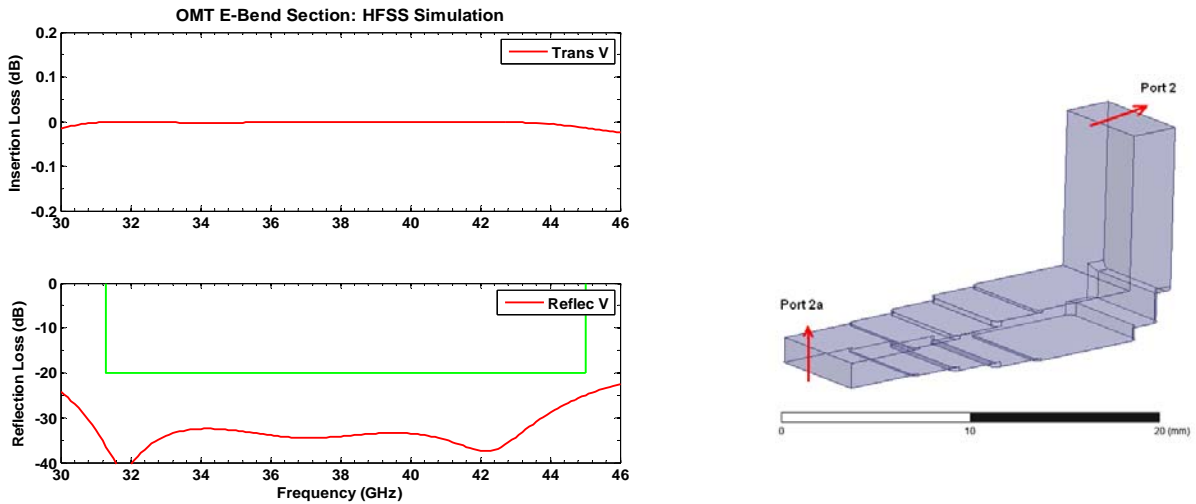


Figure 81. Left, the optimized OMT E-bend simulated insertion and reflection losses results. Right, the HFSS simulated section geometry showing it input port 2a, output port 2, and it respective polarization state V.

5.3.3 Y-combiner section Design

The Y-combiner, also called Y-power combiner [119], is used to simultaneously combine or separate two orthogonal linearly-polarized microwave signals. In our case it will be used to join together the two horizontal polarized side-arm channels that were split by the dual-ridge OMT section. Our design is based on the design presented in [120], which is similar to the Asayama's design, but with the only difference that we used a 3 stepped waveguide transformer [121] to match those signals with the WR-22 output port3, rather than the 2 stepped one used in the ALMA Band-4 OMT. The final optimized section geometry is shown at the right panel of

Figure 82, while the simulation results are shown at the left side panel of the same figure. The simulated return loss was better than -22 dB for our final design.

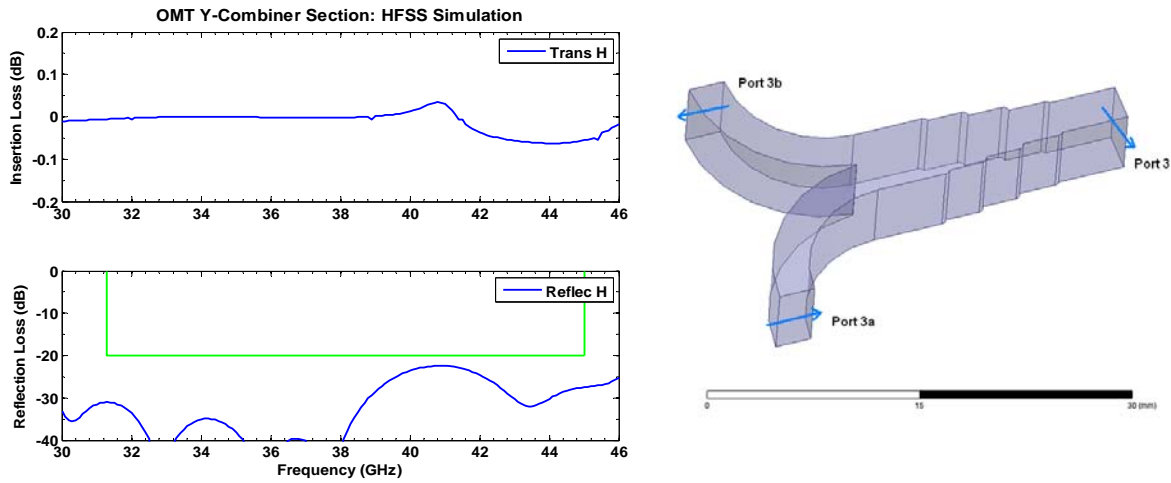


Figure 82. Left, the optimized OMT Y-combiner simulated insertion and reflection losses results. Right, the HFSS simulated section geometry showing its input ports 3a and 3b, output port 3, and its respective polarization state H.

5.3.4 The Final Optimized OMT Design

After the optimization of each one of the OMT's three main sections, they were joined together to give the final device's shape and size. First the vertical dual ridge output waveguide was connected directly to the input waveguide of the E-bend section. Secondly, the dual-ridge horizontal ports were connected to both input ports of the Y-combiner junction by using E-bend sections with a common radius on all the four bend section corners. By re-optimizing the dimensions of the stepped waveguide transition of the input part of the E-bend section, and also optimizing the radius of curvature of each one of the horizontal waveguide channels corners, the final model of our OMT design was achieved as it is shown in Figure 83. Its final dimensions were $30 \times 50 \times 70 \text{ mm}^3$. In the appendix, section 7.3, the CAD dimension details of this final OMT design can be found.

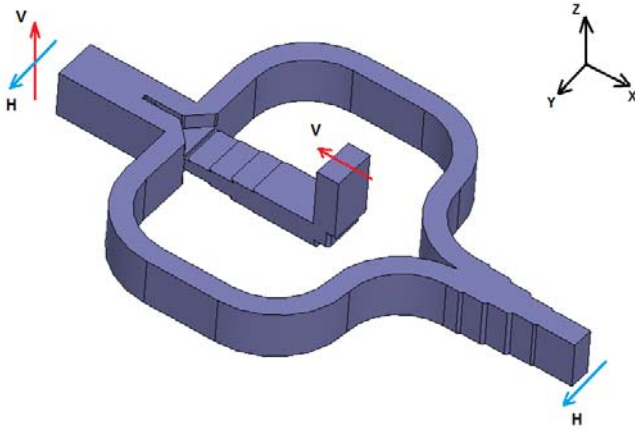


Figure 83. The final optimized HFSS OMT geometry showing its main section parts, input and output ports with their respective defined polarization states.

The final predicted performance is shown in Figures 84 and 85. The reflection losses, for both polarization channels were equal or less than -20 dB, while the cross-polar loss and isolation were better than -55 dB and -70 dB respectively. It seems that the periodical cross-polar peaks appearing on Figure 84 are some kind of resonances that start at 32 GHz, appear again at 39 GHz, and finish closer to 45.3 GHz.

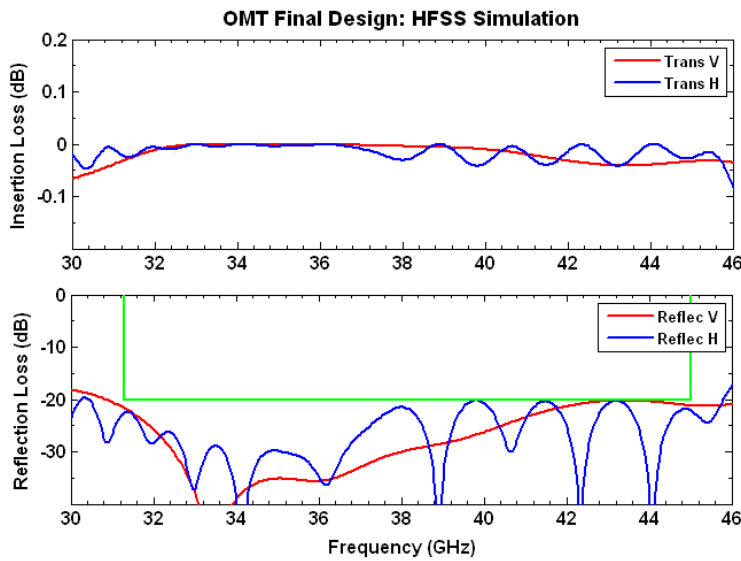


Figure 84. Isolation and reflection losses simulations of the final optimized OMT design shown in Figure 82. Observe that the reflection losses fulfill for both polarizations with the -20 dB specification even if the results are very tight at the end of the band.

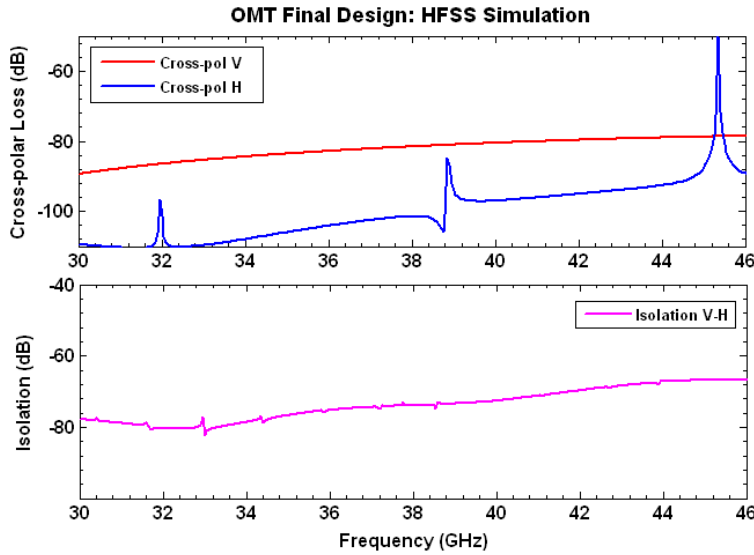


Figure 85. Simulated cross-polarization and isolation results obtained for our final optimized OMT model shown in Figure 82. Both, the cross-polarization and isolation results fulfill the requirements with large margin for the entire band.

5.4 Circular to Square Transition

An “octagonal” shaped square-to-circular waveguide transition was designed to couple the horn circular waveguide output together with the square input port section of the OMT. This device splits the unpolarized signal received by the feed horn into two orthogonal linearly-polarized components V and H. In other words, it decomposes the TE_{11} mode signal incoming from the horn circular waveguide output into a couple of orthogonal polarized TE_{01} and TE_{01} modes that propagated through the square waveguide input of the OMT. The main advantage of such transition geometry, which was first adopted by S. Asayama for the ALMA Band-5 receiver project [121], is that it is very fast to be optimized with HFSS, and compact and easy to be constructed.

This waveguide transition structure can be fully determined with a two box geometry, each one of them centered at the same point but with one of the boxes rotated by 45 deg with respect to the other. Then, by using three variables, the depth, being common for both boxes, and the side-length, one for each square box, the transition was fully optimized with the help of Optimetrics. The intersecting area between the two boxes makes the wanted transition as it is shown in Figure 85. The final simulated transition showed reflection losses better than -30 dB, and its insertion loss was quite low and flat at all frequencies as shown in Figure 86. The final dimensions were of 2.21 mm in length, and the radius of the octagonal aperture varies between 2.69 to 3.21 mm.

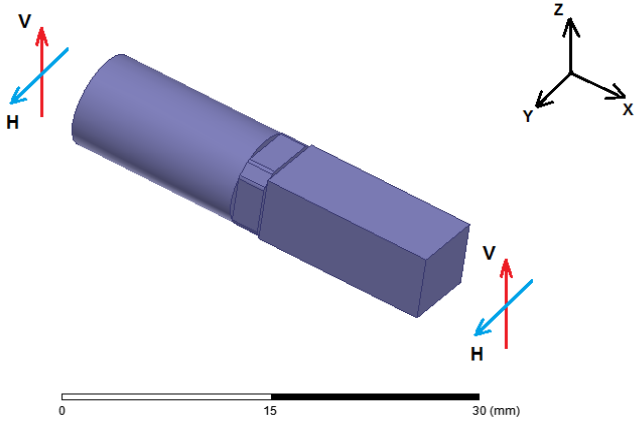


Figure 86. The HFSS structure used to simulate the performance of the transition showing it defined polarization states *V* and *H*.

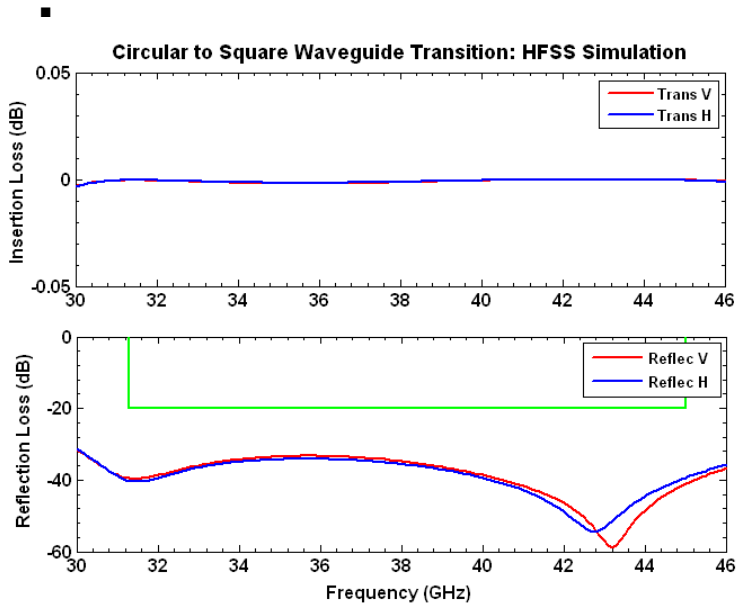


Figure 87. Insertion and return loss of both polarizations obtained from the HFSS simulated structure shown in Figure 86.

5.5 Construction of the Devices

The final optimized dual-ridge OMT design was constructed using a high precision CNC milling machine using split-block techniques made of Aluminum. The left panel of Figure 87 shows the 3 main split-block sections. The right panel shows the final assembled device with the flange holes and pins adapted to WR-22 standard waveguide connections. The final overall dimensions of the OMT were of $30 \times 50 \times 70 \text{ mm}^3$. In Figure 88, the constructed square-to-circular waveguide transition is shown. It also uses a standard WR-22 waveguide flange that surrounds the octagonal waveguide aperture, which varies in size between 2.69 to 3.21 mm, and with a depth of 2.21 mm. The CNC construction accuracy on both devices was less than $10 \mu\text{m}$.

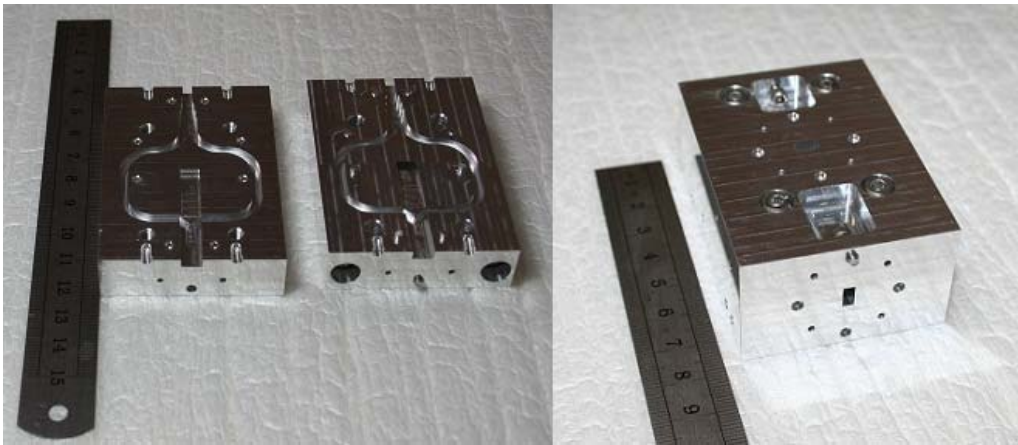


Figure 88. Left, the dual-ridge OMT, which it was constructed using split block techniques. Right, the assembled OMT having a dimension of approximately $30 \times 50 \times 70 \text{ mm}^3$.



Figure 89. The constructed square-to-circular waveguide transition that it will be used to connect the horn with the OMT. It height is of 2.21 mm the radius of the octagonal aperture varies between 2.69 to 3.21 mm.

5.6 Experimental Results

5.6.1 Description of the OMT Measuring Setup

The experimental setup shown in Figure 90 was used for testing the OMT's overall performance. It uses an Agilent vector network analyzer, model E8364C, which has one of its ports connected to the OMT input while the other one is connected to the output port of the OMT. The remaining third port is connected to a proper load termination. Then, by rotating the connections over all the device ports, a complete set of S-parameters can be obtained as a function frequency range that we want to measure. It is important to mention that a rectangular-to-squared waveguide stepped-transition and a special proper symmetric-termination was designed and constructed in our Lab, to connect or terminated properly the square input of the OMT.

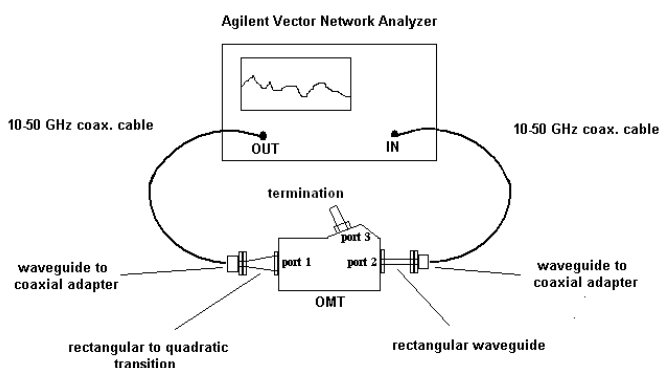


Figure 90. Lab setup arrangement that it will be used to test the OMT performance.

The most important OMT parameters that can be measured and characterized with this setup are: transmission, reflections, cross-polarization, and isolation losses.

5.6.2 OMT Measurements

Figure 91 shows the constructed 31-to-45 GHz dual-ridge OMT connected to the network analyzer while performing the isolation measurements, where each one of the OMT output ports are connect to a network analyzer line. The square input OMT port is terminated with a circular load, which is first connected to square-to-circular wave guide transition. When performing the transmission, reflection, and cross-polar measurements, the input port, one polarization port at the time, is connected to the transmitting spectrum analyzer lines (which use an especial designed rectangular-to-square waveguide adapter) while the other output ports, one is been connected to the spectrum analyzer input cable and the other is terminated with a proper WR-22 rectangular

load. The vector network analyzer was calibrated using Trough-Reflect-Line (TRL) calibration standards [122].

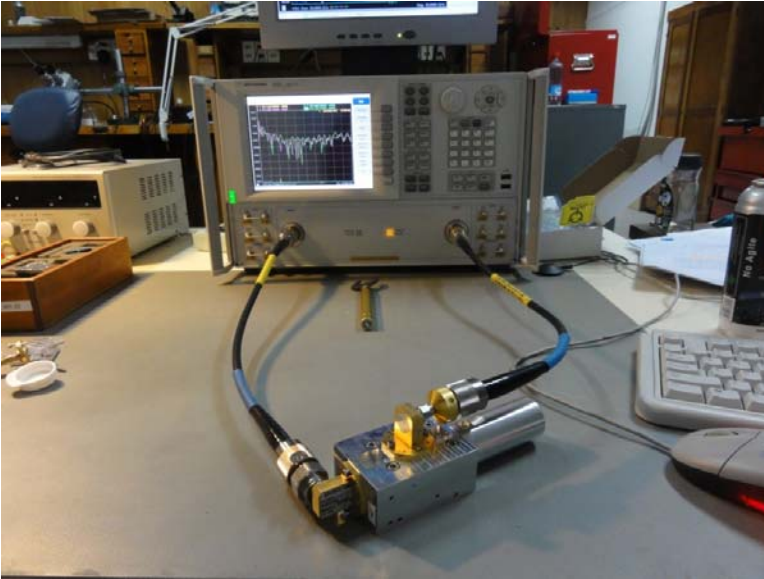


Figure 91. This picture shows how the OMT isolation measurement were performed using the Agilent vector network analyzer and coupling it coaxial cables to the corresponding OMT's vertical and horizontal waveguide outputs. The OMT square waveguide input was terminated with a proper load that was also designed and constructed at our Lab.

The insertion and reflection losses of the constructed OMT are shown in Figure 92. The reflection loss is better than -18 dB, which is -2 dB higher than the simulations. The measured cross-polar and isolation of the OMT shown in Figure 92, are less than -35 dB and better than -59 dB respectively, which are higher than the expected simulated results performed with HFSS. Despite these discrepancies, both measurements do comply with the OMT specification stated in Table 30. The $+0.1$ dB insertion loss offset is probably due to the fact that the used calibration standards are not as good as desired. Finally, it seems that the cross-polar resonant peaks shown in Figure 93, are probably due to a poor impedance matching design in the constructed rectangular-to-square waveguide transition used to connect the vector network analyzer output cable with the OMT square input port.

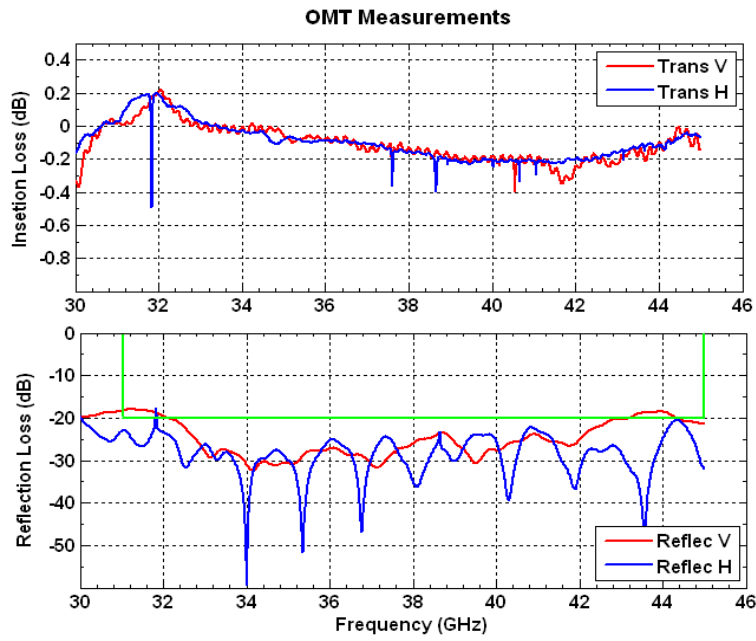


Figure 92. Insertion and reflection losses taken for both polarization between 30 and 45 GHz.

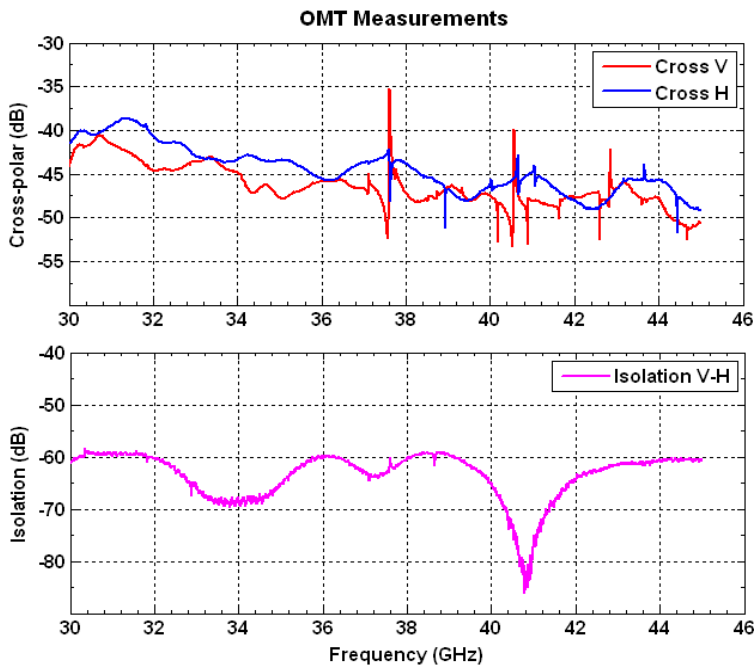


Figure 93. Measured cross-polar and isolation between 30 and 45 GHz.

5.7 Horn-Transition-OMT Simulations with HFSS

As a part of this work, it is also very important to check how both OMT polarization output performances will be deteriorated, when including the square-to-circular waveguide transition and the horn, all connected as a one piece of equipment. This was simulated in HFSS and the results are presented in Figure 94, where the reflection losses and output ports isolation of the OMT were used to characterize this behavior. The simulations showed a maximum reflection loss of about -17 dB for the horizontal polarization and maximum of about -18 dB for the vertical one, which is a deterioration of -2 to -3 dB with respect to the stand alone OMT simulation obtained in Section 5.4, and about -1 dB of deterioration, for both polarization cases, if compared with the measurements summarized in the previous Section. The worst isolation level for our simulated OMT-transition-horn system was of about -48 dB, a deterioration of about -16 dB and -11 dB if compared with the OMT stand alone simulations and with its measured results respectively. This comparison suggests that the OMT probably needs to be re-optimized so that, for example, the simulated and measured reflection losses are less than -23 dB for the entire working frequency band. Finally, Figure 95 shows how the different standard modes, simulated at 38 GHz, propagated from the horn input (TE_{11} , HE_{11} , and TE_{11}) through the transition and then into the OMT vertical (TE_{10}) polarization output port. On the other hand, Figure 96 shows the same simulation but instead it is highlighting the horizontal (TE_{01}) polarization mode propagation through the OMT output port.

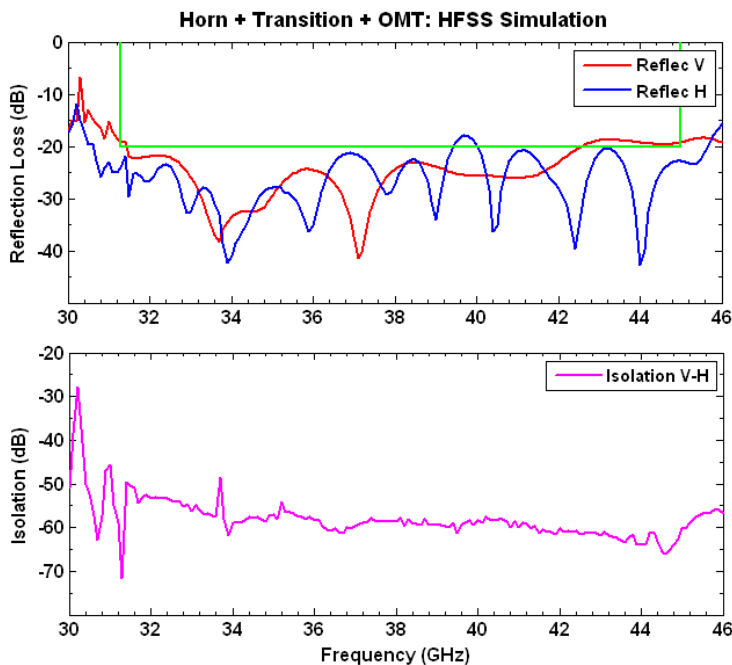


Figure 94. Horn-transition-OMT reflection-loss and isolation HFSS simulations performed between 30 and 46 GHz. Note how at some frequencies, the reflection losses for both polarization states cross above the specifications when coupling together all the elements.

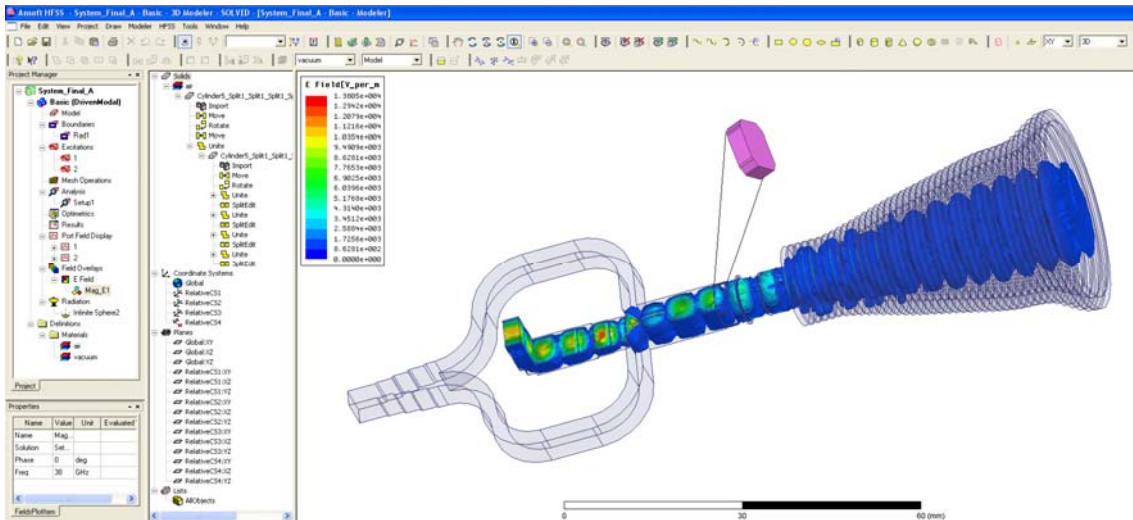


Figure 95. A HFSS simulation of the horn-transition-OMT showing how the vertical polarization “V” different modes propagate through this system at 38 GHz. In the figure the circular-to-rectangular transition is been highlighted in magenta color.

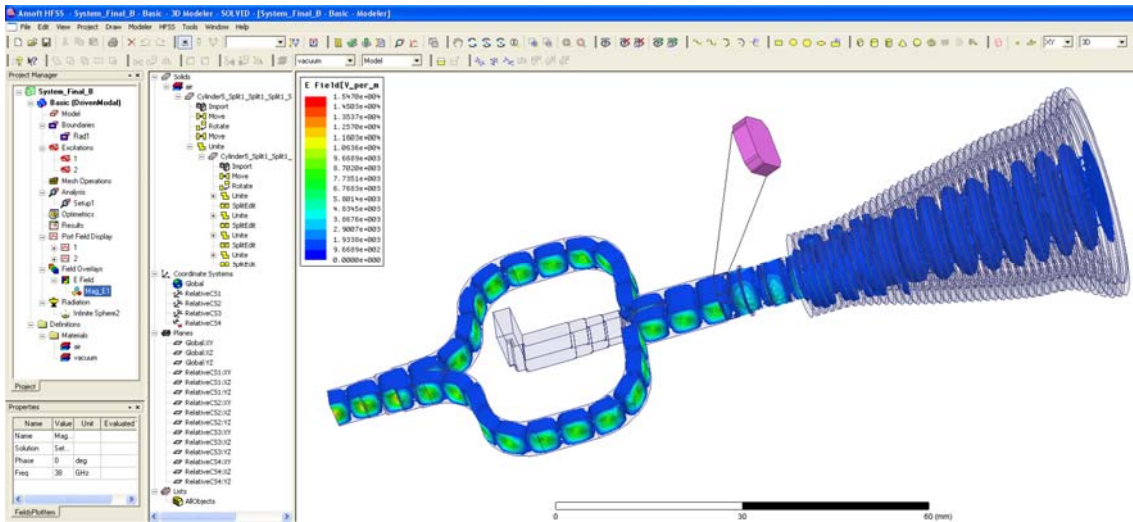


Figure 96. A HFSS simulation of the horn-transition-OMT showing how the horizontal polarization “H” different modes propagate through this system at 38 GHz. In the figure the circular-to-rectangular transition is been highlighted in magenta color.

5.8 Conclusions

The measurements results of the designed OMT, on both polarizations, exhibits return losses better than -20 dB for almost the entire 30-to-45 GHz working range, with the only exception at the band edges, where the obtained measured results shows a return performances less than -18 dB. The measured insertion losses of the constructed device, are better than -0.5 dB. The measured cross-polarization and insertion loss where less than -35 dB and -58 db respectively. In general, the constructed OMT performance showed agreement between the experimental measurements and the expected simulation results.

The small deviation between the simulation and measurements are probably due to the limited calibration quality and the insertion losses generated when connecting the rectangular-to-square waveguide transition that was specially constructed to excite one of the input ports of the OMT at a time, while performing the measurements. This constructed OMT showed to be the right chosen design that comply with almost all the ALMA specifications that, as in the case of the reflection losses, with a further more careful optimization, it can reach the desired performance. One important test that it was not done due to at the time of writing this report was to test the overall beam pattern performance of the whole optical system that includes the OMT, the square-to-circular transition, the horn, and the lens. Instead, a simulation of the first three microwave component predicts the overall return and isolation losses. This simulation showed that the return loss was lower than -18 dB and the isolation was better than -45 dB, indicating a good performance that although does not complains to a 100% with the specifications, it is very close to them.

Chapter 6

Discussion and Further Work

The aim of this thesis was to design, construct, and measure a complete low-noise optical system for a 31–45-GHz radio astronomical receiver that complies with the ALMA Band-1 specifications and that will serve as a prototype for such important project. Through this document, the most important parts of the designing theory, simulation procedures, construction techniques, and the final measured performances of the lens, horn, and OMT, have been analyzed and summarized. Most of the measured results are presented together with the expected result from the simulations that we performed for each one of the developed devices. We have also compared the results with the expected requirements and discussed about the improvements needed in every design. The most important goals that were followed when designing the different stages of the optical system were: (1) Minimize the noise contribution of each one of the optical microwave devices by using proper materials and optimizing the truncation losses and the final antenna efficiency with a suitable horn-lens design. (2) Optimize the transmission, reflections, isolation, and cross-polar level of each one of the designed and constructed passive microwave components. (3) Since the Band-1 microwave devices are physically larger than the other bands, a lot of effort was put into minimize the size of each component, especially for those that will be located on top of the 20 K stage plate.

We started our work by simulating 4 different optical system designs using quasioptical beam calculations between the horn, lens/lenses, and the antenna subreflector. Those simulations were optimized in terms of the lens dielectric materials, its total thickness, focal length, and its focal distance from the horn aperture. It was found that the single bi-hyperbolic lens system, made of HDPD, gave the best compromise between construction price and noise performance. The estimated theoretical noise contribution of such optical system was of about 10 K for the worst case, a value which is of about 4 K higher than when using the a optical system with a quartz lens and 1 K higher than the ALMA imposed specification at any frequency inside the working bandwidth of the receiver. However, the single HDPE lens system is cheaper and easy to be constructed (including the machining of the antireflection grooves on its surface) making it the best design choice, especially if 66 of them are to be constructed for the ALMA telescope.

From the estimated horn beam parameters, such as the beam-waist size and the beam-waist position, which were obtained from the designed HDPE designed optical system, different horn shapes were designed. The best obtained design have been the spline-line corrugated horn, which, besides complying with all the imposed ALMA specifications, also has the mayor advantage of being short an compact, making it very suitable to accommodate with the other receiver components, such as the OMT and both HEMT amplifier blocks, inside the 15-K cryocooled stage. The measurements obtained when testing the constructed spline-line horn using split-block technique were excellent. Low side-lobes, low cross-polar levels, and symmetrical beam shapes

were obtained which agree with the simulations and fulfill the specifications. Moreover, when integrating the lens into the horn measuring setup, the beam shape was quite Gaussian and the estimated farfield antenna beam efficiencies were quite satisfactory, but with a approximately $-2,5\%$ lower than the 80% required for this band. This difference can be explained due to the lack of accuracy when aligning the horn and lens during the measurements, which results in lateral and axial defocus losses. The last component to be designed and constructed was the dual-ridge orthomodal transducer. Our OMT model has two mayor advantages if we compare with other existing designs at similar frequency range: it supports a large bandwidth (first of its kind) and contains a square-to-circular waveguide transition that could be easily integrated in the OMT block, making it a very compact device. Its measured performance showed a return better than -18 dB, isolation less than -45 dB, and a cross-polarization better than -35 dB. Both the isolation and measured cross-polar levels did comply with the specifications, while the return loss is still a $+2$ dB higher than expected. We believe that our constructed 31-to-45 GHz OMT can further be optimized so, then, all the requirements can be reached. Since this device is simple to fabricate and assemble, it will be a very suitable polarization splitting device that can be mass produced for all the ALMA Band-1 receivers.

Summarizing all the results of each one of the designed components for our optical system setup, we see that most of the ALMA specifications were complied, or were very close to them. Therefore, our optical system makes a good candidate to be used in the Band-1 receiver, but there are still a few improvements that need to be addressed. First, the spline-line horn needs to be re-optimized so its diffracted energy, especially at low frequencies, does not increase the total optical system noise contribution of the receiver. Secondly, it will be important to confirm our quasioptical beam ray propagation model, used to design the optical horn-lens-subreflector arrangement, with a more proper ray-tracing program (such as Zemax for example) that can estimate with higher the accuracy the lens final focal length and tits distance to the horn. Furthermore, once the lens shape is determined, the total lens thickness must be increased according to the antireflection concentrical-grooves that must be machined on the lens surface to minimize reflection losses, and it could also be necessary to measure experimentally the refraction index and loss-tangent of the HDPE lens material to ensure accuracy when calculating the quasioptical beam propagation of the optical setup. The final improvement that it is recommended to be done is that, probably, the circular-to-rectangular waveguide transition needs to be machined in the same aluminum block part of the OMT, which will probably make the measured cross-polar levels come closer to the predicted values made in HFSS.

References

- [1] D. Miller, et al, "A Measurement of the Angular Power Spectrum of the CMB from l-100 to 400", ApJ, 524:L1-4, 1999 (astro-ph/9906421).
- [2] S. T. Myers, et. al, "Measurements of the Sunyaev-Zeldovich Effect in the Nearby Clusters A478, A2142 and A2256" Astrophysical Journal v.485, p.1.
- [3] Myers S. T., "Scaling the universe: Gravitational lenses and the Hubble constant". Proc. Natl. Acad. Sci. 96, 4236-4239 (1999).
- [4] Walsh, D.; Carswell, R. F.; Weymann, R. J., "0957 + 561 A, B - Twin quasi stellar objects or gravitational lens". Nature, vol. 279, May 31, 1979, p. 381-384.
- [5] Padeli Papadopoulos, Rob Ivison, Chris Carilli, Geraint Lewis, "A massive reservoir of low-excitation molecular gas at high redshift" Nature 409, 58-60 (4 January 2001).
- [6] Jackson, J. M., Paglione, T. A. D., Carlstrom, J. E. & Rieu, N. "Submillimeter HCN and HCO+ emission from galaxies". Astrophys. J. 438, 695±701 (1995).
- [7] K. Rohlfs and T.L. Wilson, "Tools of Radio Astronomy". Fourth edition, Springer Astronomy and Astrophysics Library, 2004
- [8] Pennock S, Shepherd P "Microwave engineering with wireless applications", 1998, Macmillan Press.
- [9] V. Vassilev, et al, Performance of a Sideband Separating SIS Mixer for 85-115 GHz. Chalmers GARD internal report.
- [10] Maral G., and Bousquet M., Satellite Communications Systems, 4th edition, John Wiley & Sons, 2002.
- [11] *McClaning, K., and Tom V. Radio Receiver Design. Atlanta, GA: Noble Publishing Corporation, 2000.*
- [12] Atmospheric transmission calculator at Chajnantor:
<http://www.apex-telescope.org/sites/chajnantor/atmosphere/>
- [13] H. Rudolf, M. Carter, and A. Baryshev, "The ALMA Front End Optics—System Aspects and European Measurement Results". IEEE TRANSACTIONS ON ANTENNAS AND PROPAGATION, VOL. 55, NO. 11, NOVEMBER 2007

- [14] C. Granet, “Designing Axially Symmetric Cassegrain or Gregorian Dual-Reflector Antennas from Combinations of Prescribed Geometric Parameters” IEEE Antennas and Propagation Magazine, Vol. 40, No. 2, April 1998
- [15] ALMA Project Book, “Antennas”. Chapter 4:
<http://www.alma.nrao.edu/projectbk/construction/>
- [16] ALMA Project Book, “Cryogenics”. Chapter 6:
<http://www.alma.nrao.edu/projectbk/construction/>
- [17] M. Sugimoto, et al, “Thermal link for cartridge-type cryostat”. Copyright © 2003 Published by Elsevier Science Ltd. Cryogenics Volume 43, Issue 8, August 2003, Pages 435-439
- [18] ALMA MEMO #455, “Cartridge Test Cryostats for ALMA Front End”:
<http://www.alma.nrao.edu/memos/>
- [19] ALMA Project Book, “Requirements & Specifications”. Chapter 2:
<http://www.alma.nrao.edu/projectbk/construction/>
- [20] ALMA Project Book, “Front Ends”. Chapter 5:
<http://www.alma.nrao.edu/projectbk/construction/>
- [21] J. M.Casalta, A. Molins, M. Bassas, M. Canchado, E. Creus, A. Tomàs. “ALMA Front End Amplitude Calibration Device Design and Measured Performances”. Advanced Optical and Mechanical Technologies in Telescopes and Instrumentation, Proc. of SPIE Vol. 7018- 701838, 2008.
- [22] T. Mimura, “The Early History of the High Electron Mobility Transistor (HEMT)”. IEEE TRANSACTIONS ON MICROWAVE THEORY AND TECHNIQUES, VOL. 50, NO. 3, MARCH 2002
- [23] C. A. Mead, “Schottky barrier gate field effect transistor,” Proc. IEEE, vol. 54, pp. 307-308, Feb. 1966.
- [24] B. F. Burke, and F. Graham-Smith, “An Introduction to Radio Astronomy. Cambridge University Press; 2 edition (January 15, 2002).
- [25] Pospieszalski M.W., “Extremely low-noise amplification with cryogenic FETs and HFETs: 1970-2004”. Microwave Magazine, IEEE. Volume: 6, Issue: 3 pp. 62- 75, Sept. 2005.
- [26] G. Moorey, et. al., “CRYOGENICALLY COOLED 30 – 50 GHZ RECEIVER SYSTEMS FOR THE AUSTRALIA TELESCOPE”. Seventh Workshop on Applications of Radio Science Conference – WARS 2008, Queensland, Australia.
- [27] S. Padin, et. al., “The Cosmic Background Imager” Astronomical Society of the Pacific, Vol. 114:83–97, 2002.
- [28] The Effelsberg Radio Telescope Webpage:

<http://www.mpifr-bonn.mpg.de/div/effelsberg/receivers/receiver.html>

- [29] EVLA Project Book, Chapter 5, “RECEIVERS”:
<http://www.aoc.nrao.edu/evla/pbook.shtml>
- [30] QUIET , the Q/U Imaging Experiment array webpage:
<http://quiet.uchicago.edu/instrumentation/index.html#Introduction>
- [31] J. Lamb et al., “ALMA receiver optics design”. ALMA Memo #362, 2001.
- [32] “ALMA Front-end Optics Design Report “ALMA internal Report nr: FEND-40.02.00.00-035-B-REP (2007).
- [33] Bahaa E. A. Saleh, Malvin Carl Teich, Fundamentals of Photonics, Wiley-Interscience; 1st edition (August 15, 1991).
- [34] P. F. Goldsmith, Quasioptical Systems: Gaussian Beam Quasioptical Propagation and Applications. New York: IEEE Press, 1998.
- [35] J. W. Lamb, “Miscellaneous data on materials for millimeter and submillimeter optics,” Int. J. Infrared Millim. Waves, vol. 17, no. 12, pp. 1997–2034, Dec. 1996.
- [36] N. Roddis and J. Kitching, “A REMOTE CONTROLLED HORN/LENS FEED FOR A 25 METRE RADIO TELESCOPE” Jodrell Bank Observatory Internal Report. University of Manchester, Macclesfield, UK.
- [37] F. T. Martínez, et. al., “Óptica con lente correctora de fase a 22 GHz, 30 GHz y 45 GHz”. Informe técnico del Centro Astronómico de Yebes, CAY, nr. 2002-4
- [38] J.W. Lamb, “Cross-polarization and astigmatism in matching grooves,” Int. J. Infrared Millim.Waves, vol. 17, no. 12, pp. 2159–2165, Dec. 1996.
- [39] J. E. Garret and J. C. Wiltse, “Fresnel zone plate antennas at millimeter wavelengths”. Int. J. Infrared Millimeter Waves, vol. 12, pp 195-220, march 1991.
- [40] D. Koller, et al. “INFRARED MEASUREMENTS OF POSSIBLE IR FILTER MATERIALS”. International Journal of Infrared and Millimeter Waves, Vol. 27, No. 6, June 2006.
- [41] Mohammed N. Afsar and Igor Tkachov, “MEASUREMENT OF TRANSMITTANCE AND SCATTERING OF RADOME MEMBRANES FROM 30 TO 1000 GHz”. IEEE MTT-S Digest, 1997.
- [42] M. Carter, et al., “ALMA Front-end Optics Design Report”. FEND-40.02.00.00-035-B-REP, versión B, 2007.
- [43] P.-S. Kildal, Foundations of antennas: A unified approach, Studentlitteratur, 2000.

- [44] P.J.B. Clarricoats, A. D. Olver “Corrugated Horns for Microwave Antennas”. IEE Electromagnetic Waves Series 18. 1984.
- [45] B. M. Thomas, et. al., “Design of Wide-Band Corrugated Conical Horns for Cassegrain Antennas”, IEEE TRANSACTIONS ON ANTENNAS AND PROPAGATION, VOL. AP-34, NO. 6, JUNE 1986.
- [46] C. Granet and G. L. James. Design of Corrugated Horns: A Primer. IEEE Antennas and Propagation Magazine, Vol. 47, No. 2, April 2005.
- [47] P.-S. Kildal, “Gaussian beam model for aperture-controlled and flare-angle-controlled corrugated horn antennas”. IEE PROCEEDINGS, Vol. 135, Pt. H, No. 4, AUGUST 1988
- [48] GRAEME L. JAMES Teil-to-HE, “Mode Converters for Small Angle Corrugated Horns”. IEEE TRANSACTIONS ON ANTENNAS AND PROPAGATION, VOL. AP-30, NO. 6, NOVEMBER 1982
- [49] Granet C., “Profile options for feed horn design”, Proceedings of the Asia Pacific Microwave Conference, Vol. 1, pp. 1448-1452, 2000.
- [50] X. Zhang, “Design of conical corrugated feed horns for wide-band high frequency applications,” IEEE Trans. Microwave Theory Tech., vol. 41, pp. 1263–1274, Aug. 1993.
- [51] Granet C., James G.L., Bolton R. and Moorey G., (2004) “A smooth-walled spline-profile horn as an alternative to the corrugated horn for wide band millimeter-wave applications,” IEEE Trans. Antenna Propagat., 52(3), pp. 848-85.
- [52] D. Rabanus, et. al., “Measurement of properties of a smooth-walled spline-profile feed horn around 840 GHz”. Infrared Physics & Technology, ed.: G. Neil, H.N. Rutt, vol.: 48, no.: 3, pp.: 181-186, 2006
- [53] Potter P., “A new horn antenna with suppressed sidelobes and equal beamwidth” Microwave J., vol. 6, pp. 71-78, June 1963.
- [54] G. Yassin, P. Kittara et al., “A High Performance Horn for Large Format Focal plane Arrays”. Eighteenth International Symposium on Space Terahertz Technology, California Institute of Technology, California USA. March 2007.
- [55] Jens Bornemann and Marjan Mokhtaari Initial Design and Optimization of Broad-Band and Dual-Band Square-to-Circular Waveguide Transitions”. Microwave Conference Proceedings, 2005. APMC 2005. Asia-Pacific Conference Proceedings
- [56] B. F. Burke and F. Graham-Smith, “An Introduction to Radio Astronomy”, Cambridge University Press, 2002.
- [57] M. Boifot, E. Lier, and T. Scahung-Petterssen, “Simple and broadband Orthomode Transducer”. IEE Proceedings, Vol. 137, Pt. H. N.6, 1990.

- [58] Wollack, E., “A Full Waveguide Band Orthomode Junction”, 1996, NRAO, EDIR Memo Series, #303.
- [59] ALMA memo #425: “THE BØIFOT ORTHOMODE JUNCTION”:
<http://www.alma.nrao.edu/memos/>.
- [60] Wollack E. J., “TCHEB_x: Homogenous Stepped Waveguide Transformer”, 1995, NRAO internal press release.
- [61] Wollack, E., “Notes on Right-Angle-Miter Bends for Standard Rectangular Waveguide,” 1995, NRAO, EDTN Memo Series, #172.
- [62] Wollack, E., “Simple Split-Block 90-Degree E-Plane Bends for Low Power Applications,” 2001, NRAO, EDTN Memo Series, #187
- [63] Wollack, E., “On the Compensation of E-Plane Bifurcations in Rectangular Waveguides,” 1997, NRAO, EDTN Memo Series, #181.
- [64] S. Asayama, “Double-ridged Orthomode Transducer for ALMA Band 4 receiver”. NAOJ internal MEMO, 2007.
- [65] Dunning “Double Ridged Orthogonal Mode Transducer for the 16-26GHz Microwave Band” CSIRO Australia Telescope National Facility Memo.
- [66] R. Kerr, “Elements for E-Plane Split block Wave guide Circuits”. ALMA Memo #381, 2001.
- [67] Alessandro Navarrini and Richard L. Plambeck. “A Turnstile Junction Waveguide Orthomode Transducer. IEEE TRANSACTIONS ON MICROWAVE THEORY AND TECHNIQUES, VOL. 54, NO. 1, JANUARY 2006.
- [68] KERN, high precision CNC machines:
<http://www.kern-microtechnic.com/oldpage/2-Machines-Micro-TD.html>.
- [69] “ALMA Front-end Optics Design Report “ALMA internal Report nr: FEND-40.02.00.00-035-B-REP (2007).
- [70] P. F. Goldsmith, Quasioptical Systems: Gaussian Beam Quasioptical Propagation and Applications. New York: IEEE Press, 1998.
- [71] ALMA Project Book, “Antennas”. Chapter 5:
<http://www.alma.nrao.edu/projectbk/construction/>
- [72] Chung Wa Wong. “Introduction to Mathematical Physics: Methods and Concepts”. 1st edition, Oxford University Press, 1991.
- [73] R. Wylde , “Optics and Corrugated Feedhorns”. IEE Proc., Vol. 131. Pt. H, No. 4, pp. 258-262. 1984.

- [74] MatLab software, ver. 7.0. The MathWorks Corporation, Natick, MA, USA.
- [75] F.J. Pedrotti, L. S. Pedrotti, “Introduction to Optics”. 2nd Edition, Prentice Hall Press. 1992.
- [76] J. W. M. Baars, “The Paraboloidal Reflector Antenna in Radio Astronomy and Communication: Theory and Practice”. 1st edition, Springer Press. 2007.
- [77] R. Padman, J. A. Murphy, and R. E. Hills, “Gaussian mode analysis of Cassegrain antenna efficiency,” IEEE Trans. Antenna Propagat., vol. AP-35, pp. 1093–1103, Oct. 1987.
- [78] C. A. Balanis, “Antenna Theory: Analysis and Design. 3rd Edition, Willey Press. 2005.
- [79] Ruze, “Antenna Tolerance Theory – A Review” Proc. IEEE, Vol. 54 p.633-640, April 1966.
- [80] ALMA Memo #175. B. Shillue, “Gain Degradation in a Symmetrical Cassegrain Antenna Due to Laterally Offset Feeds”. <http://www.alma.nrao.edu/memos/>
- [81] E. Hecht, “Optics”. 4th edition, Addison-Wesley Press. 2001.
- [82] H. Rudolf, M. Carter, and A. Baryshev, “The ALMA Front End Optics—System Aspects and European Measurement Results”. IEEE TRANSACTIONS ON ANTENNAS AND PROPAGATION, VOL. 55, NO. 11, NOVEMBER 2007.
- [83] ALMA Receiver Optics Design Electromagnetic Analysis ALMA internal Report nr: FEND-40.01.00.00-006-A-REP, 2001.
- [84] J.W. Lamb, “Cross-polarization and astigmatism in matching grooves,” Int. J. Infrared Millim. Waves, vol. 17, no. 12, pp. 2159–2165, Dec. 1996.
- [85] High Frequency Structure Simulator (HFSS), version 11, Ansoft Corporation, Pittsburgh, PA, USA.
- [86] ALMA MEMO NO. 377 D. Koller, A. R. Kerr, G. A. Ediss, and D. Boyd, “Design and Fabrication of Quartz Vacuum Windows with Matching Layers for Millimeter-Wave Receivers “. <http://www.alma.nrao.edu/memos/>
- [87] M. Carter and R. Nesti. “ALMA band 1 horn design” Internal Technical note. INAF - Arcetri Astrophysical Observatory. 2002
- [88] M. Carter, et al., “ALMA Front-end Optics Design Report: Appendix 1”. FEND-40.02.00.00-035-B-REP, version B, 2007.
- [89] G. L. James, “Design of Wide-Band Compact Corrugated Horns,” IEEE Transactions on Antennas and Propagation, AP-32, 10, October 1984, pp. 1134-1 138.

- [90] C. Granet and G.L. James, "Design of Corrugated Horns: A Primer," IEEE Antennas and Propagation Magazine, Vol. 47, No. 2, April 2005, pp. 76–84.
- [91] C. A. Balanis (Editor), "Modern Antenna Handbook". 1th edition. Wiley-Interscience press. 2008.
- [92] P.-S. Kildal, "Gaussian beam model for aperture-controlled and flareangle-controlled corrugated horn antennas". IEE PROCEEDINGS, Vol. 135, Pt. H, No. 4, AUGUST 1988.
- [93] G. L. James, "Analysis and Design of TE₁₁-to-HE₁₁ Corrugated Cylindrical Waveguide Mode Converters," IEEE Transactions on Microwave Theory and Techniques, MTT-29, 1981, pp. 1059- 1066.
- [94] C. Granet, "Profile options for feed horn design", Proceedings of the Asia Pacific Microwave Conference, Vol. 1, pp. 1448-1452, 2000.
- [95] Olver A.D., Clarricoats P.J.B., Kishk A.A., Shafai L., "Microwave horns and feeds", IEE Electromagnetic waves series, ISBN 0 85296 809 4, 1994.
- [96] C. Granet, G.L. James, R. Bolton, G. Moorey, "A smooth-walled spline-profile horn as an alternative to the corrugated horn for wide band millimeter-wave applications," IEEE Transactions on Antennas and Propagation, Vol. 52, No. 3, March 2004, pp. 848–854.
- [97] "Horn antenna synthesis CAD Tool". MICROWAVE JOURNAL®, March 2008 issue.
- [98] C. Granet, T.S. Bird, "Optimization of corrugated horn radiation patterns via a spline-profile," ANTEM 2002, 9th International Symposium on Antenna Technology and Applied Electromagnetics, Montreal, Canada, 2002, pp 307–310.
- [99] C. Granet, P. Mena, P. Zorzi, I.M. Davis, J.S. Kot, G. Pope, "Corrugated and Smooth-Walled Spline-Profile 31.3–45 GHz Horns for ALMA." Proceedings of the 4th European Conference on Antennas and Propagation, Barcelona, Spain, 12–16 April 2010.
- [100] S. Gregson, J. McCormick and C. Parini, "Principles of Planar Near-Field Antenna Measurements." Institution of Engineering and Technology Press, 2007.
- [101] T. Brockett and Y. Rahmat-Samii, "A Novel Portable Bipolar Near-field Measurement System for Millimeter-wave Antennas: Construction, Development, and Verification," IEEE Antennas and propagation Magazine, Vol. 50, No. 5. October 2008.
- [102] F. Colleoni, "Diseño e implementación de un sistema de medición de patrones de radiación de antenas en el campo cercano". Millimeter-wave Laboratory internal Report, 2012. http://www.das.uchile.cl/lab_mwl/publications.html
- [103] D. Janse van Rensbur, "Millimeter Wave Near-Field Antenna Testing." Nearfield Systems Inc. Microwave Product Digest Article, Aug 2010.

- [104] P.N. Betjes, "An algorithm for automated phase center determination and its implementation," AMTA Conference, 2007.
- [105] Emerson & Cuning Microwave Products. <http://www.eccosorb.com/>
- [106] K. Pontoppidan and C. Haupt, "Electromagnetic properties and optical analysis of the ALMA antennas and Front Ends". TICRA Report S-1430-02, 2007.
- [107] R. Hills, et. al. "Beam efficiency Calculator User manual ". ALMA internal Report nr: FEND-40.09.00.00-014-A-MAN (2010).
- [108] S. Asayama. "Development of Double-Ridged Waveguide Orthomode Transducer for the 2 MM Band". Journal of Infrared Millimeter and Terahertz Waves, vol. 30, no. 6, pp. 573-579, 2009.
- [109] D. M. Pozar, "Microwave Engineering". Wiley; 3 edition, 2004.
- [110] D. Cheng. "Field and wave electromagnetic". Addison-Wesley; 2 edition, 1989.
- [111] G. Matthaei , E. Jones, L. Young. "Microwave Filters, Impedance-Matching Networks, and Coupling Structures". Artech Microwave Library Press, 1980.
- [112] Wollack E. J., "TCHEBx: Homogenous Stepped Waveguide Transformer". NRAO internal press release, 1995.
- [113] R. E. Collin. "Foundations for Microwave Engineering". Wiley-IEEE Press; 2 edition, 2000.
- [114] Chang K. "Handbook of microwave and optical components". John Wiley & Sons Press, 1989.
- [115] P. Kildal. "Artificial soft and hard surfaces in electromagnetic". IEEE Transaction on Antennas and Propagation. Vol. 38, pp. 1537-1544, 1990.
- [116] A. Dunning "Double Ridged Orthogonal Mode Transducer for the 16-26GHz Microwave Band" CSIRO Australia Telescope National Facility Memo.
- [117] Wollack, E., "Notes on Right-Angle-Miter Bends for Standard Rectangular Waveguide," 1995, NRAO, EDTN Memo Series, #172.
- [118] Wollack, E., "Simple Split-Block 90-Degree E-Plane Bends for Low Power Applications," 2001, NRAO, EDTN Memo Series, #187
- [119] Wollack, E., "On the Compensation of E-Plane Bifurcations in Rectangular Wave guides," 1997, NRAO, EDTN Memo Series, #181.
- [120] R. Kerr, "Elements for E-Plane Split block Wave guide Circuits". ALMA Memo #381, 2001.

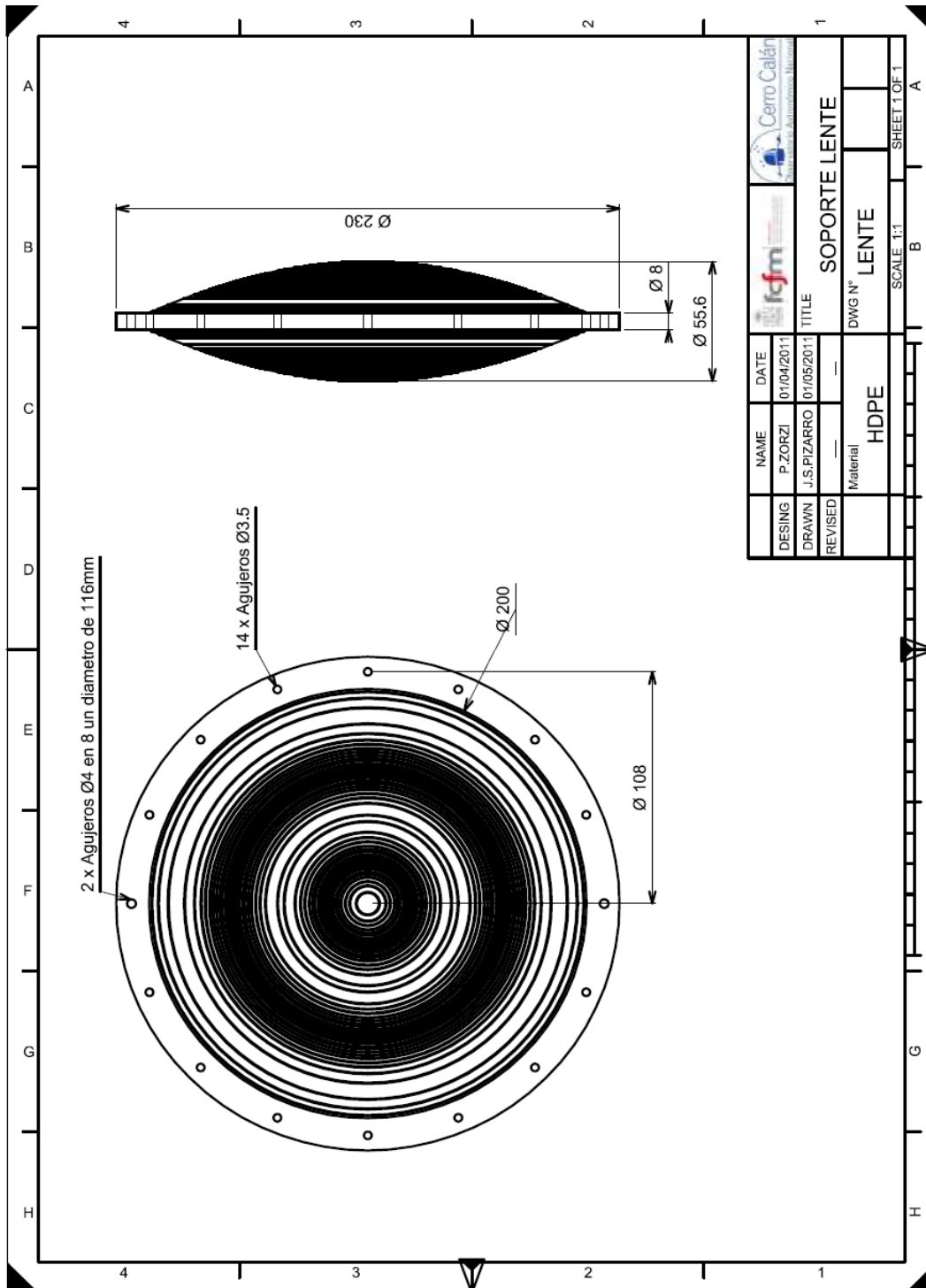
[121] “ALMA Band-5 Cold Cartridge Assembly Design Report“. ALMA internal Report nr: FEND-40.02.05.00-010-B-REP (2009).

[122] “Applying Error Correction to Network Analyzer Measurements“. Agilent Technologies © Application Note: AN 1287-3.

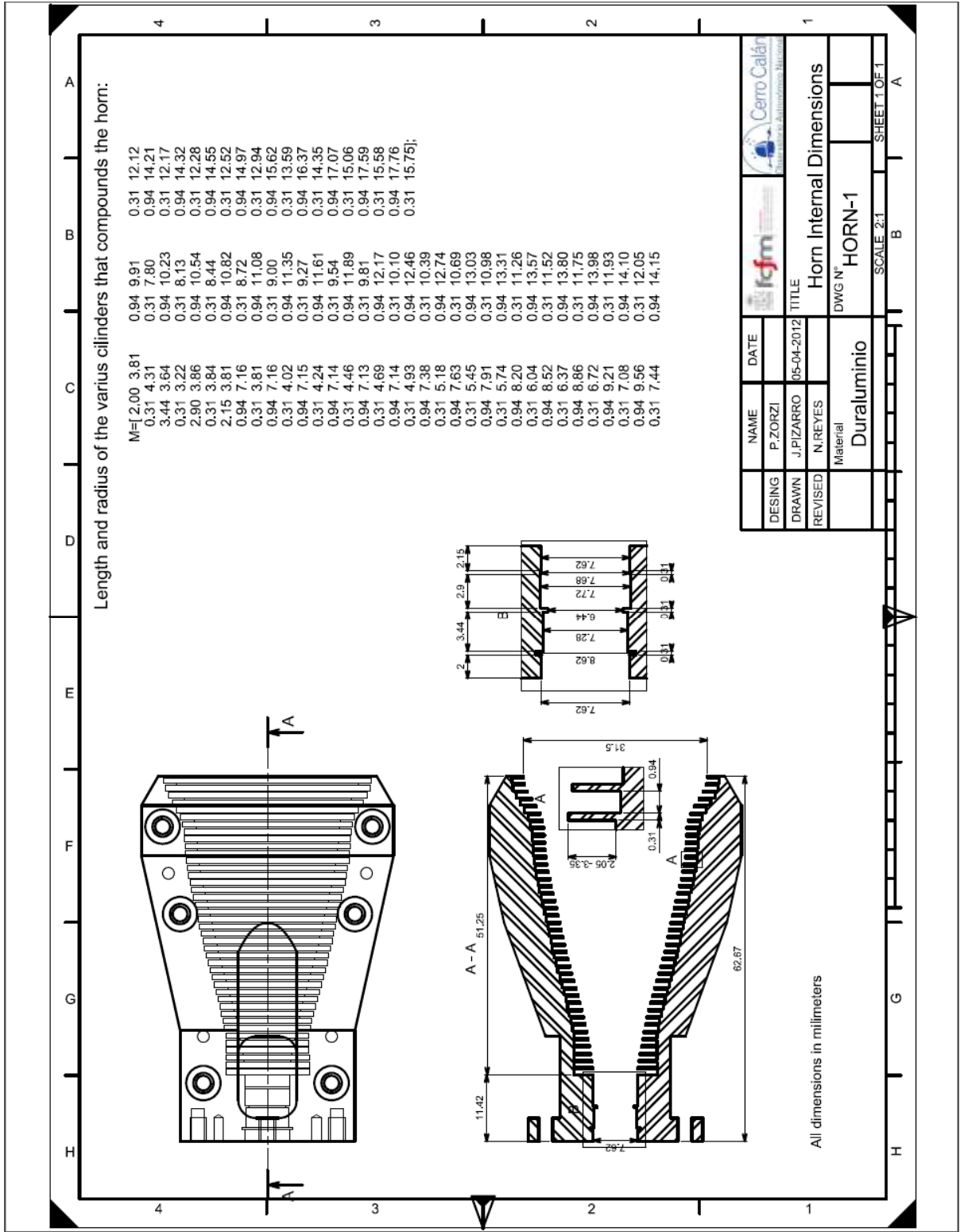
Appendix A

Technical Drawing

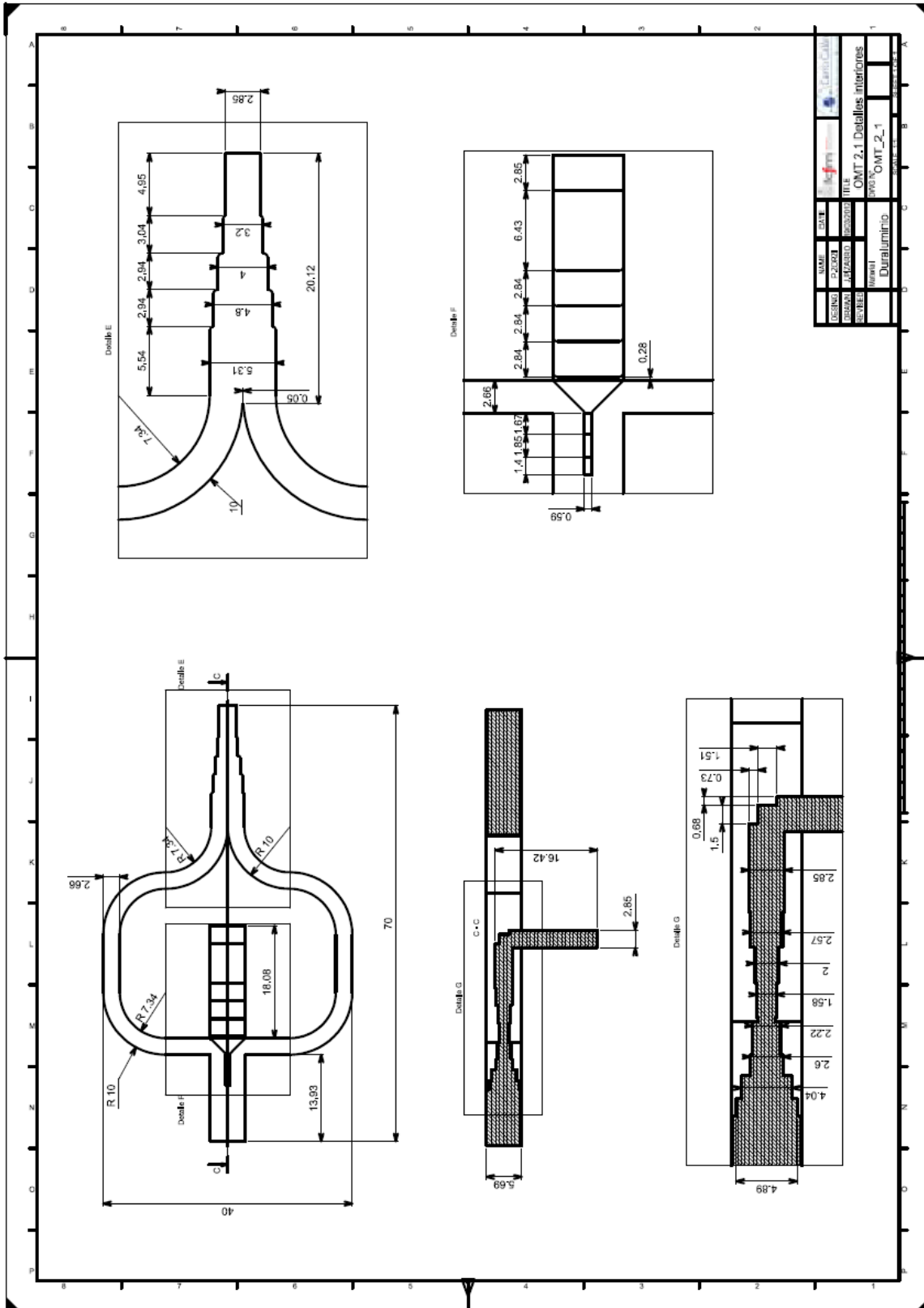
Lens:



Horn:



OMT:



Appendix B:

Author List of Publications

Articles

- 1) P. Zorzi, C. Granet, F. Colleoni, N. Reyes, J. Pizarro, P. Mena, L. Bronfman, "Construction and measurement of a 31.3-45 GHz Optimized Spline-profile horn with corrugations". Journal of Infrared Millimeter and Terahertz Waves, October 2011.
- 2) Nicolas Reyes, Pablo Zorzi, Jose Pizarro, Ricardo Finger, F. Patricio Mena and Leonardo Bronfman, "A Dual Ridge Broadband Orthomode Transducer for the 7-mm Band". Journal of Infrared Millimeter and Terahertz Waves, 2012.

Conferences

- 1) N. Reyes, P. Zorzi, C. Jarufe, F. Navarrete, F. Colleoni, J. Pizarro, F.P. Mena and L. Bronfman, "ALMA band 1 development at Universidad de Chile". Millimeter and Submillimeter Detectors and Instrumentation for Astronomy V, edited by Wayne S. Holland; Jonas Zmuidzinas, Amsterdam, July 2012.
- 2) P. Zorzi, D. Henke, S. Claude, P. Mena, L. Bronfman, and J. May, "Revisiting the ALMA Band 1 Optics Design ". Proceedings of the 21th International Symposium on Space Terahertz Technology, Oxford, March 23-25, 2010.
- 3) N. Reyes, P. Zorzi, C. Jarufe, P. Altamirano, F. P. Mena, J. Pizarro, L. Bronfman, J. May, C. Granet, and E. Michael. "Construction of a Heterodyne Receiver for Band1 of ALMA". Proceedings of the 21th International Symposium on Space Terahertz Technology, Oxford, March 23-25, 2010.
- 4) N. Reyes, P. Zorzi, F. P. Mena, C. Granet, E. Michael, L. Bronfman, and J. May, "Design of a Heterodyne Receiver for Band 1 of ALMA". Proceedings of the 20th International Symposium on Space Terahertz Technology, Charlottesville, USA, April 20-22, 2009.
- 5) Javier Ruiz-del-Solar, Patricio Loncomilla, and Pablo Zorzi, "Applying SIFT Descriptors to Stellar Image Matching". Progress in Pattern Recognition, Image Analysis and Applications Lecture Notes in Computer Science Volume 5197, Springer press, 2008. pp 618-625.